Status and perspectives of hierarchical porous carbon materials in terms of high-performance lithium–sulfur batteries

Xiang, Yinyu; Lu, Ewan; Kottapalli, Ajay Giri Prakash; Pei, Yutao T.

Published in:
Carbon Energy

DOI:
10.1002/cey2.185

Publication date:
2022

Received: 18 December 2021 | Revised: 25 January 2022 | Accepted: 30 January 2022

DOI: 10.1002/cey2.185

REVIEW

CARBON ENERGY WILEY

Status and perspectives of hierarchical porous carbon materials in terms of high-performance lithium–sulfur batteries

Yinyu Xiang | **Liqiang Lu** | **Ajay Giri Prakash Kottapalli** | **Yutao Pei**

Advanced Production Engineering (APE), Engineering and Technology Institute Groningen (ENTEG), Faculty of Science and Engineering, University of Groningen, 9747 AG, Groningen, The Netherlands

Correspondence
Liqiang Lu and Yutao Pei, Advanced Production Engineering (APE), Engineering and Technology Institute Groningen (ENTEG), Faculty of Science and Engineering, University of Groningen, Nijenborgh 4, 9747 AG Groningen, The Netherlands.
Email: ewan.lu@rug.nl and y.pei@rug.nl

Funding information
China Scholarship Council, Grant/Award Number: 201806950083

Abstract

Lithium–sulfur (Li–S) batteries, although a promising candidate of next-generation energy storage devices, are hindered by some bottlenecks in their roadmap toward commercialization. The key challenges include solving the issues such as low utilization of active materials, poor cyclic stability, poor rate performance, and unsatisfactory Coulombic efficiency due to the inherent poor electrical and ionic conductivity of sulfur and its discharged products (e.g., Li_2S_2 and Li_2S), dissolution and migration of polysulfide ions in the electrolyte, unstable solid electrolyte interphase and dendritic growth on anodes, and volume change in both cathodes and anodes. Owing to the high specific surface area, pore volume, low density, good chemical stability, and particularly multimodal pore sizes, hierarchical porous carbon (HPC) materials have received considerable attention for circumventing the above problems in Li–S batteries. Herein, recent progress made in the synthetic methods and deployment of HPC materials for various components including sulfur cathodes, separators and interlayers, and lithium anodes in Li–S batteries is presented and summarized. More importantly, the correlation between the structures (pore volume, specific surface area, degree of pores, and heteroatom-doping) of HPC and the electrochemical performances of Li–S batteries is elaborated. Finally, a discussion on the challenges and future perspectives associated with HPCs for Li–S batteries is provided.

KEYWORDS

carbon/sulfur cathodes, hierarchical porous carbon, lithium–sulfur batteries, lithium metal anodes, separators/interlayers, synthetic methods

1 | INTRODUCTION

The demand for sustainable energy has witnessed a drastic increase mainly due to the vast emissions of greenhouse gases associated with excessive combustion of fossil fuels. Extensive research efforts have been dedicated toward the technology development for renewable energy sources (e.g., solar, wind, tide, and geothermal energy) and methods to harvest and convert them for societal use.[1,2] However, these clean energy

sources are intermittent, unevenly distributed, and unstable for utilization. Pursuing reliable, economical, and efficient energy storage systems with high energy density is of great significance in addressing these issues and for taking advantage of renewable energies.[3] Rechargeable batteries, such as lead-acid, nickel–cadmium, nickel metal hydride, and lithium-ion batteries (LIBs), have been widely used in numerous applications during the past century. Among them, LIBs, based on ion-insert lithium metal oxides or lithium phosphates as the cathodes and graphite as the anodes, ever since their naissance in the late 1980s, have been dominating the electronic market for more than 30 years owing to their relatively high energy density and operating voltage, low self-discharge rate, no memory, and long lifespan.[4–6] Nevertheless, current commercial configurations of LIBs are approaching the theoretical limitation of energy density/capacity and have rather high costs and safety issues, and therefore cannot meet the demands for widely storing the renewable energies and the endurance of electrical transportation and devices. Alternative substitutes of LIBs with desirable energy density, good safety, and low cost have been intensively researched in both academia and industry.

Rechargeable lithium–sulfur (Li–S) batteries have great potential as promising candidates of the next-generation batteries due to their high theoretical capacity (1675 mAh g^{-1} calculated based on sulfur) and energy density (2600 W h kg^{-1}), abundance in resources, and the low cost of sulfur.[7,8] Despite the aforementioned merits, the practical commercialization of Li–S batteries is impeded by the following issues.[9–11] First, both S and its discharged products (lithium sulfide or disulfide) are intrinsic electrical and ionic insulators, resulting in low utilization of active materials, sluggish kinetics, and poor rate performances.[12,13] In addition, the dissolution and migration of intermediate polysulfide (PS) ions (Li_2S_x, $x = 4$–8) during the charging and discharging processes cause serious loss of active materials in the electrolyte and parasitic reactions with the lithium anode, which are associated with severe decay and deterioration of batteries.[14] The large volumetric expansion (80 vol%) during the conversion from S into Li_2S also leads to fracture or delamination of electrodes. Moreover, the formations of Li dendrites and an unstable solid electrolyte interphase (SEI) on Li metal anodes cause low Coulombic efficiency (CE), continuous consumption of electrolytes, and safety concerns.[15–17]

Extensive research has been conducted to tackle the aforementioned problems with the aim of improving the performance of Li–S batteries. The main methods for solving the issues caused by sulfur cathodes and PSs are to improve the conductivity of the battery system and physically constrain PS ions by introducing carbonaceous materials as conductive hosts for cathodes[18] and as coating layers for separators.[19,20] These carbonaceous materials include graphene,[21,22] carbon nanotubes,[23] carbon spheres,[24] porous carbons,[25–27] and many other carbon forms and structures. After a major breakthrough made by Li et al.[28] through confining sulfur in CMK-3 (a kind of mesoporous carbon, Figure 1A), porous carbons with high specific surface areas (SSA), tunable pore structures, and controllable morphologies and chemical components have been extensively investigated and utilized as both sulfur hosts and functional coating layers to enhance the Li–S battery performances. According to the classification of the International Pure Union and Applied Chemistry (IPUAC) in 1985, porous carbon materials can be divided into three categories based on pore width: macroporous carbon with pore widths larger than 50 nm, mesoporous carbon with pore widths between 2 and 50 nm, and microporous carbon with pore widths smaller than 2 nm.[39] In previous reviews, it was reported that the micropores and small mesopores with high SSA confer better cyclic stability due to solvent-restricted lithiation/delithiation of sulfur, while the large mesopores and macropores with high pore volume enable high sulfur loadings and facilitate ion transport.[18,40] In many cases, carbon materials with unimodal pore size hardly provide desirable electrochemical performances of Li–S batteries as well as other energy storage devices.[41,42]

Contrary to microporous carbon, mesoporous carbon, and macroporous carbon, all of which only have unimodal pore sizes, hierarchical porous carbon (HPC) materials have multiple levels of porosity and show a porous structure with multimodal pore sizes from micropores, mesopores to macropores.[43,44] The multiple levels of pore sizes of HPC usually comprise bimodalities such as micro/meso, meso/macro, and micro/macro, or even trimodalities such as micro/meso/macro.[45] Thus, in addition to their excellent electrical conductivity, tailorability, and low costs, HPCs also have the advantages of large pore volume, high SSA, and unique multimodal porous structures.[46,47] Due to the combination of the advantages of micropores and large pores, HPCs are potentially able to augment the electrochemical performance of Li–S batteries in industry.[48] Extensive progress has been made in the field of HPC-based Li–S cells during the past decade, and some typical milestones (experiments and theoretical calculations) are presented in Figure 1, from S@HPC cathodes, HPC interlayer/HPC-coated separators, and the Li@HPC anode to finally integrate these configurations for further improving the performance toward practical applications.

In comparison with carbon materials of unimodal pore sizes, HPCs have the following merits when used in

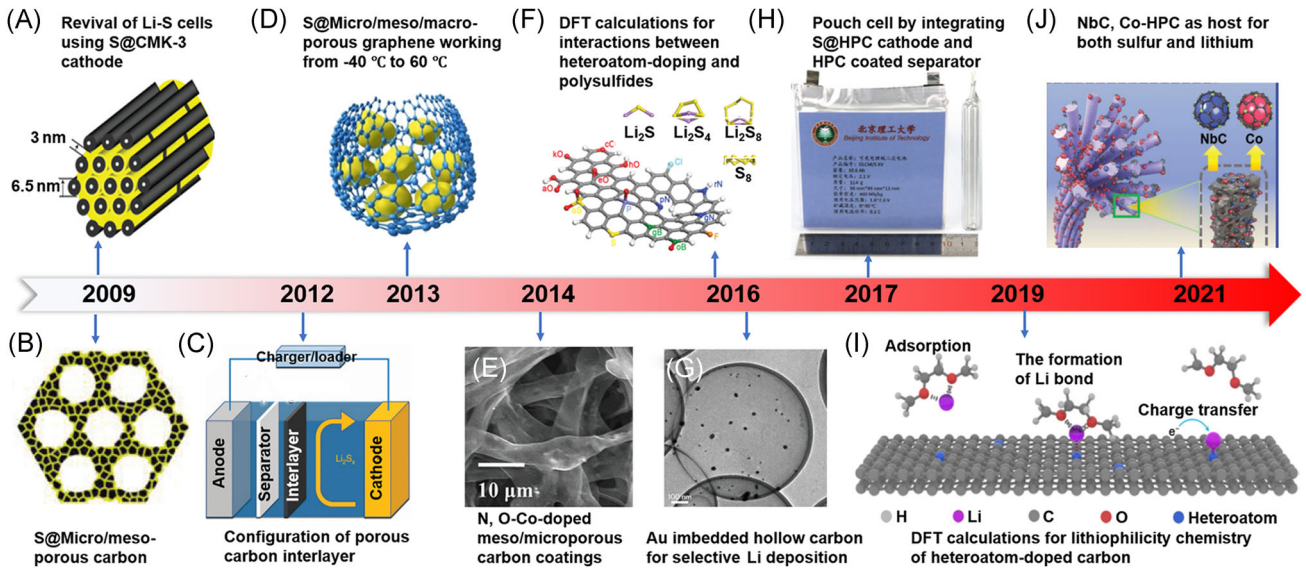

FIGURE 1 A brief timeline and representative strategies of hierarchical porous carbons (HPCs) (including experiments and theoretical simulations) for improving the performance of lithium–sulfur (Li–S) cells, covering HPC-based composite cathode design, separator modification/interlayer configuration, and lithium metal protection: (A) S@CMK-3 cathode, with the work leading to the revival of Li–S batteries; (B) S@micro/mesoporous carbon; (C) conception of a porous carbon interlayer between the separator and the cathode; (D) S@micro/meso/macroporous graphene working from −40°C to 60°C; (E) N,O–Co-doped meso/microporous carbon coating on the separator; (F) density functional theory (DFT) calculations for interaction between heteroatom doping and polysulfides; (G) Au-imbedded hollow carbon for selective Li deposition, introducing seed-guided lithium growth; (H) pouch cell integrating the S@HPC cathode and the HPC-coated separator achieving a high-energy-density Li–S battery at an extremely low E/S ratio (electrolyte amount/sulfur mass); (I) DFT calculations for lithiophilicity chemistry of heteroatom-doped carbon; and (J) NbC, Co–HPC as the host for both sulfur and lithium. (A) Reproduced with permission: Copyright 2009, Nature Publishing Group.[28] (B) Reproduced with permission: Copyright 2009, American Chemical Society.[29] (C) Reproduced with permission: Copyright 2012, Nature Publishing Group.[30] (D) Reproduced with permission: Copyright 2013, Elsevier.[31] (E) Reproduced with permission: Copyright 2014, Royal Society of Chemistry.[32] (F) Reproduced with permission: Copyright 2016, Wiley.[33] (G) Reproduced with permission: Copyright 2016, Nature Publishing Group.[34] (H) Reproduced with permission: Copyright 2017, Wiley.[35] (I) Reproduced with permission: Copyright 2019, American Association for the Advancement of Science.[36] (J) Reproduced with permission: Copyright 2021, Wiley[37]

Li–S batteries. As a sulfur host, the conductive carbon skeleton can greatly improve the conductivity of cathodes. Moreover, the micropores and small mesopores of HPCs endow sulfur cathodes with high SSA and provide more active sites for sulfur redox, while the large pore volume originating from large mesopores and macropores is favorable for storing a high content of sulfur and buffering the volume expansion.

Similarly, HPCs can be used as coating layers/interlayers for modifying separators to improve cell performances on the basis of multiple functions. First, the HPC layers can serve as a second current collector to enhance the electrical conductivity of sulfur cathodes. Second, the redox reactions of the as-dissolved and migrated PSs occur on the conductive HPCs, therefore reutilizing the active materials and retaining capacity retention. Furthermore, the three-dimensional porous channels and particularly the micropores can serve as barriers to suppress the migration of PSs without blocking or reducing the transport of lithium ions, leading to a mitigated "shuttle effect". As a result, the concentration of PSs on the lithium anode side can be significantly reduced, preventing the corrosion of lithium anodes and the formation of thick sulfide films on anodes. Due to these functions, the capacity, cyclic stability, and fast discharge/charge performances of the Li–S cells can be considerably enhanced. However, the addition of thick coating layers or interlayers would inevitably increase the mass and volume of the battery, requires more electrolyte, and thus decreases the energy density. More research needs to be conducted to balance the cyclic stability, rate performances, and energy density of Li–S cells by tuning the thicknesses, microstructures, and mass of HPC interlayers.

Aside from confining PSs and improving conductivity, HPCs can also potentially be applied in anodes and enhance the performances of Li metal batteries (including Li–S batteries). On the basis of Sand's time model, which indicates the onset of lithium dendrites, the growth of dendrites is correlated to several factors:

the ambipolar diffusion coefficient, electrolyte concentration, anionic and cationic mobilities, and practical current density.[49] To function as current collectors and host materials of the anode, three-dimensional (3D) porous skeletons have a larger electrode/electrolyte interface than that of two-dimensional (2D) current collectors, thus decreasing the current density and prolonging Sand's time, consequently delaying the formation of dendrites.[50,51] The porous structure could further confine the deposition of lithium to suppress dendrite growth and accommodate volume changes. The creation of small pores such as nanopores considerably increases the electrode/electrolyte interface. However, nanopores have a relatively small pore volume that limits the accommodation of lithium and electrode capacity. Large pores such as macropores yield large pore volume but have the limitation of low surface area. To this end, the hierarchical porous structure that comprises of both small pores and large pores can synergistically boost the electrode/electrolyte interface and electrode capacity. Compared to metallic current collectors, carbon materials, in particular, have low density and good electrochemical stability. These advantages increase the potential to use hierarchical carbon materials in future research on Li metal anodes. However, there are few reviews on the applications of HPCs for Li metal anodes.[52–54]

This article focuses on the progress of HPCs for use in rechargeable Li–S batteries, including the novel synthetic strategies of HPCs, design, and applications of advanced sulfur cathodes, separators/interlayer, and rationally constructed lithium anodes to enhance the electrochemical performance of Li–S batteries (Figure 2). The structure–activity relationships between the structures (pore volume, specific surface area, ordering degree of pores, and heteroatom doping) of HPCs and the electrochemical performances of Li–S batteries will be systematically elaborated. The progress made with the use of HCPs for designing Li metal anodes is also discussed. Finally, we highlight the key challenges and perspectives associated with future research on HPCs for Li–S batteries.

2 | SYNTHETIC STRATEGIES OF HPCS

A variety of approaches have been developed for the preparation of HPCs, which can be generally classified into a hard-templating method, a soft-templating method, a templating/activation combination method, and a templating-free method according to the template agents utilized during the synthesis process. In this section, a recapitulative description of preparation methods for HPCs is elaborated in detail.

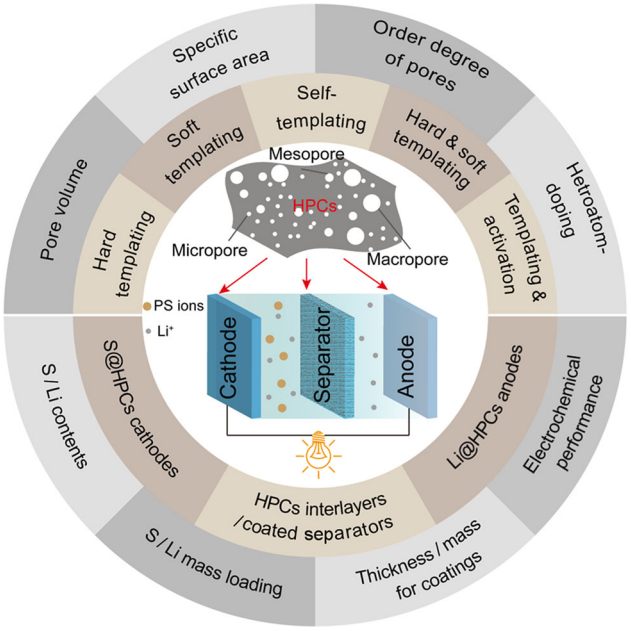

FIGURE 2 An overview of the synthetic methods of hierarchical porous carbons (HPCs) covering hard templating methods, soft templating methods, self-templating methods, hard and soft templating methods, and templating and activation methods, and the applications of HPCs in lithium–sulfur (Li–S) cells, including S@HPC cathodes, HPC-functionalized separators/interlayers, and Li@HPC anodes

2.1 | Hard templates

The hard templating method is an efficient way to produce HPCs due to its ability to precisely control the morphologies, particle sizes, and pore structures of HPCs by adjusting the structures and concentration of predesigned templates. The synthesis of HPCs using the hard templating method consists of the following steps: at least two hard templates with different particle sizes or pore structures, or one hard template with a hierarchical structure are impregnated with carbon precursors, followed by a heat treatment of the mixture in an inert or hydrocarbon atmosphere. HPC replicas can be obtained after the removal of hard templates by chemical etching or dissolution. Considering the cost and manipulability, silica, metal/metal oxide/metal hydroxide templates, and inorganic salt templates are the widespread hard templates, while phenolic formaldehyde (PF) resin, saccharides (sucrose, glucose, and chitosan), melamine, polymers, and carbon-rich gases (CH and C_2H_2) are common carbon feedstocks for producing porous carbon materials.

2.1.1 | Silica templates

Various types of silica structures, including nanoparticles/nanospheres,[55–60] silica gel/colloidal silica,[61–65] silica monolith,[66–68] hierarchical microarchitectures,[69,70] and hierarchical porous silica,[71,72] are popular hard templates for producing HPCs due to their low costs and accessibility, as well as the development of Stober methods. As shown in Figure 3A, a series of 3D flower-like carbon nanospheres of size around 200 nm were prepared using urchin-like hierarchical silica spheres (UHSSs) as the template and tuning the calcination temperature.[69] To begin with, UHSS was modified by 3-aminopropyltrimethoxysilane in a dry toluene solution. Thereafter, due to the surface electrostatic self-assembly, glucose was uniformly coated on the surface and filled into the pores of UHSS, after a hydrothermal reaction. Finally, after carbonization at a high temperature, followed by the removal of silica templates using hydrofluoric acid, flower-like hierarchical carbon nanospheres with microporous and small mesoporous channels were obtained.

Ionic liquids with high thermal stability and different heteroatoms have been broadly used as carbon sources for the preparation of heteroatom-doped carbonaceous materials. For example, Schneider et al.[71] developed a nitrogen-doped carbon with an interconnected hierarchical porous microstructure (N-HPC) using 1-ethyl-3-methylimidazolium dicyanamide (EMIM DCA) feedstock providing both carbon and nitrogen, while hierarchical porous silica monoliths were used as hard templates. To achieve maximum filling of EMIM DCA into the pores of silica monoliths, the impregnation process should be operated at reduced pressure and can be quickly completed, which is less tedious than using other precursors. The pore size distribution of N-HPC revealed two distinct maxima at 6–7 and 750 nm from the nitrogen adsorption and mercury intrusion porosimetry analyses, demonstrating the meso/macroporous structures.

Beyond directly using the presynthesized silica templates, the silica templates can also be formed in the mixture containing both silica and carbon precursors. Following reaction and carbonization, highly ordered porous carbon materials can be fabricated. For instance, a root-like carbon nanofiber with an ordered hierarchical porous structure (OHPCNF) was synthesized using a facile electrospinning technology, with polyvinylpyrrolidone (PVP) as the carbon source and tetraethyl orthosilicate (TEOS) as the silica template precursor.[59] As a result of the hydrolysis of TEOS, the silica template was generated during the course of the reaction. In addition, because TEOS could enhance the phase separation of the solution and then influence the diameter of nanofibers, the nanofiber diameter can also be controlled by altering the ratios of TEOS to PVP solution.[59] Another advantage is that the freestanding carbon nanofiber networks can be conveniently fabricated by peeling the electrospun nanofibers off the substrates and used for lightweight electrodes with enhanced energy density.

2.1.2 | Metal/metal oxide/metal hydroxide templates

The removal of silica templates usually requires poisonous hydrofluoric acid or hot concentrated alkali, which is time-consuming and harmful to both humans and the environment. In contrast, insoluble metal, metal oxide, and metal hydroxide templates, such as nickel,[76–80] magnesium oxide,[73,81,82] calcium oxide,[83] zinc oxide,[84] anodic aluminum oxide,[85] manganese dioxide,[86] ferroferric oxide,[87] and nickel hydroxide,[88–90] magnesium hydroxide,[91–93] and layered double hydroxide,[94,95] can be readily etched or removed using diluted acids. In addition, these metals, metal oxides, and metal hydroxide templates can usually catalyze the growth of graphitic carbon, thus improving the graphitization and electrical conductivity of HPCs. For example, Wang et al.[90] reported a strategy to fabricate 3D periodic hierarchical porous graphitic carbon (PHGC) under alkaline synthesis conditions. In their work, ethanol solution of phenolic resin was added to the alkaline $Ni(OH)_2$ solution to obtain a homogeneous hydroxide/resin mixture. After drying, a hybrid of inorganic and resin materials was obtained. The PHGC was then synthesized after further calcination, followed by etching templates. To further optimize the structure of HPC with an HPC–carbon nanotube (CNT) hybrid structure using metal hydroxide, a one-step approach, which is by incorporating $Ni(OH)_2$ into a phenolic resin carbon precursor under alkaline conditions, was developed by Luo et al.[78] During carbonization, Ni nanoparticles that were reduced from $Ni(OH)_2$ served as pore agents for the hierarchical pores and catalyzed the epitaxial growth of CNTs, improving the conductivity of hybrids and leading to better performance than pure HPCs for energy storage.

In recent years, chemical vapor deposition (CVD) growth of high-quality graphene/few-layer graphitic carbon with a hierarchical structure on the porous metal/metal oxide substrates has been proven to be an efficient approach. In particular, MgO-based templates have been shown to be one of the most favorable catalysts for CVD growth of porous graphene/few-layer graphitic carbon both experimentally[96–98] and theoretically.[99] As shown in Figure 3B, Lyu et al.[73] reported a kind of hierarchical carbon nanocage with only a few-layer carbon shell and coexisting micro-, meso-, and macropores using a MgO template. MgO templates derived from a magnesium carbonate precursor of $4MgCO_3{\cdot}Mg(OH)_2{\cdot}5H_2O$ by thermal

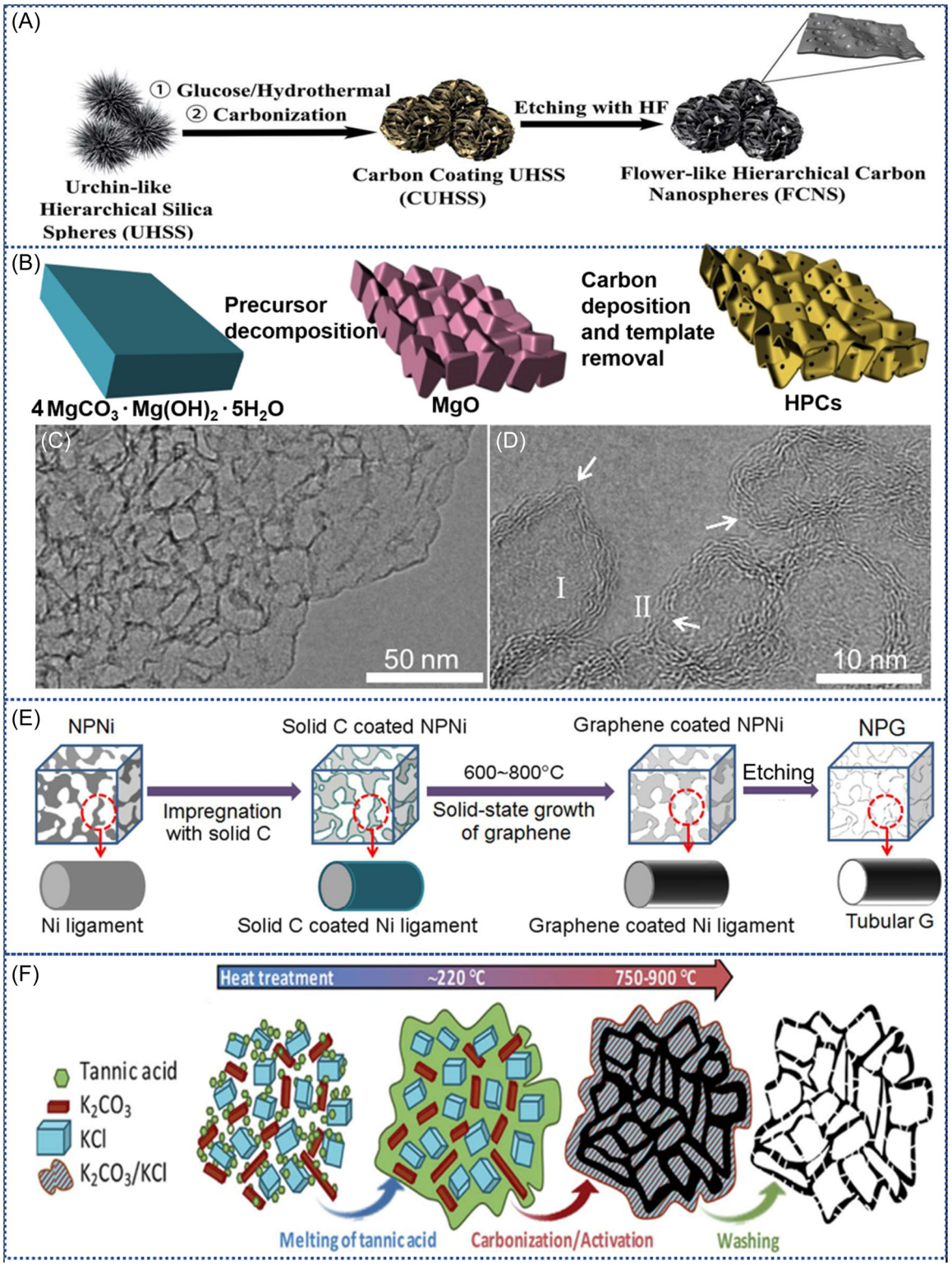

FIGURE 3 Synthesis of hierarchical porous carbon (HPCs) through hard templates. (A) Preparation of flower-like carbon nanospheres (FCNSs) using hierarchical silica spheres. (B) Synthesis of HPC nanocages using MgO templates through chemical vapor deposition growth. (C,D) Transmission electron microscopy (TEM) image and high-resolution TEM image of HPC nanocages, respectively. (E) Production of hierarchical porous graphene using a porous nickel template. (F) Utilization of salt templates for the production of HPCs. (A) Reproduced with permission: Copyright 2017, Royal Society of Chemistry.[69] (B–D) Reproduced with permission: Copyright 2015, Elsevier.[73] (E) Reproduced with permission: Copyright 2018, Royal Society of Chemistry.[74] (F) Reproduced with permission: Copyright 2015, Royal Society of Chemistry. HF, hydrofluoric acid; NPG, nanoporous graphene; NPNi, nanoporous nickel

decomposition retained the hierarchical nature of the precursor.[73] CVD carbon layers were deposited on the surface of the hierarchical MgO by introducing benzene vapor. Hierarchical carbon nanocages with four to seven well-graphitized carbon layers (Figure 3C,D) were then collected after the removal of the template. Benefiting from a large SSA of 1276 $m^2 g^{-1}$ and a high micro–mesopore volume of 4.18 $cm^3 g^{-1}$, the unique hollow structures could contribute to high sulfur loading and energy density for Li–S batteries.

As graphene or graphitic carbon has higher crystallization than amorphous carbon, hierarchical porous graphene or graphitic materials show higher electrical conductivity and better mechanical properties. Usually, the synthesis of porous graphitic carbon or graphene through CVD is realized at high temperatures (above 1000°C). Most of the metallic frameworks are subjected to severe coarsening of pores and ligaments at such high temperatures, resulting in undesirable pore sizes of porous graphene or carbon materials. To regulate the pore sizes of porous graphene and avoid coarsening of metal templates, our group has developed a low-temperature approach (≤800°C) for synthesizing interconnected meso/macroporous graphene through solid-state growth of graphene on the surface of nanoporous nickel that functions both as a template and as a graphene-growth catalyst (Figure 3E).[74,100] The as-generated 3D graphene foam possessed two different types of pores, namely, nontubular open pores inherited from Ni macrofoams and closed tubular pores produced from the etching of Ni ligaments. Both the nontubular and tubular pores yielded a 3D bicontinuous network, which is favorable for mass transfer during discharging and charging. Thanks to the method, the tubular pore sizes were tunable from a few microns down to below 50 nm by selecting templates with a corresponding ligament size. Notably, a high-performance cathode with enhanced cyclic stability was constructed by accommodating sulfur nanoparticles inside the tubular pores of as-synthesized nanoporous graphene (NPG). As the walls of tubular pores contain defect-induced micropores, the dissolution of the long-chain PSs with length above 0.5 nm is assumed to be effectively prohibited due to the physical and chemical trapping by the holey graphene walls, which was confirmed by the enhanced cyclic stability. It was also found that smaller pore sizes lead to higher utilization of sulfur. Further investigations revealed that reduced particle sizes of the NPG hosts favored mass transfer and, therefore, enhanced the rate performances.[100]

Benefiting from the facile synthesis of nanoporous Ni through hydrogen reduction of metallic salts in a more efficient and recyclable approach, the synthesis of porous Ni templates and the growth of graphene were combined in a one-route process, through which a lightweight and 3D porous graphene foam was obtained and used for a free-standing sulfur cathode with high electrode capacity.[101]

2.1.3 | Salt templates

Apart from metal/metal oxide/metal hydroxide, inorganic, and organic salts are another group of hard templates that can be conveniently removed using water or dilute acid for the production of hierarchical porosity. For instance, inorganic NaX salts (X: Cl^-, CO_3^{2-}, SiO_3^{2-}) were chosen as templates for the preparation of 3D HPCs, which is schematically shown in Figure 3F.[75] At first, glucose and three kinds of NaX were dissolved into distilled water, and then the water was removed via freeze-drying. During the freezing process, multiscale (from nanometers to micrometers) salt particles formed because of crystallization of the salts. Simultaneously, salt particles evenly coated with glucose were self-assembled into a 3D architecture. Finally, pure 3D HPCs were obtained after carbonization and removal of salts by washing.[75] However, the aggregation of salt nanoparticles owing to the high surface energy, especially during high-temperature calcination, is the main problem, which inevitably leads to the generation of disordered pores with undesirable pore shapes. To overcome this obstacle, an in situ template formation strategy was adopted. For example, water-soluble lithium citrate could be used as the template agent. Under high-temperature heating, lithium citrate was decomposed to generate Li_2CO_3 templates, while sucrose and the decomposed carbon-containing products of citrate were transformed into carbon. After thermal treatment and the removal of Li_2CO_3, ordered micro-, meso-, and macropores remained in the carbon structures, presenting a facile way to avoid the agglomeration of salt templates.[102]

2.1.4 | Organic polymer templates

Besides the inorganic materials, some organic materials that are soluble in nonpolar organic solvents or thermally decomposable such as polyurethane[103] and tetramethylammonium oxalate[104] have been studied as hard porogenic agents for synthesizing HPC materials. Due to the good solubility in hot acetone and decomposition under an air atmosphere, interconnected polystyrene is the widely used organic hard template.

2.2 | Soft templates

Despite the precise tailoring of the morphology and the pore structure of HPCs using hard templates, the

hard-templating technique obviously has some intrinsic disadvantages associated with large-scale production as it usually requires sophisticated procedures and harmful chemicals for the removal of the templates. In contrast, the soft templating method, which is based on self-assembly between organic molecules/amphiphilic block copolymers and polymerizable carbon precursors, is more flexible and less harmful for synthesizing HPCs. Generally, the production of HPCs with soft templates consists of the following two steps: self-assembly of soft templates and precursors, and then annealing of precursor–template composites. In the first step, dissolved soft template moleculars combine with each other into micelles, and then their charged, hydrophilic terminations covalently bond with carbon precursors, and form rigid organic micelles with carbon precursor warping. In the calcination step, precursors can be pyrolyzed and converted into carbon while pores are formed due to the thermal decomposition or evaporation of templates at high temperatures and in an inert atmosphere. Originating from the ordered assembly for the formation of micelles, HPCs obtained by these soft templates usually contain ordered mesopores. In addition, the shapes of micelles influence the pattern of the ordered pores: cylindrical micelles are likely to yield hexagonal structures, while spherical micelles are likely to form cubic patterns. To date, surfactant templates are the main soft templates used for preparing HPCs.

On the basis of the polarity of the functional groups, surfactant templates can be divided into the following three types: cationic surfactants, anionic surfactants, and nonionic surfactants. Owing to its positive charge, hexadecyl trimethylammonium bromide (CTAB), being a kind of cationic surfactant, was chosen as a soft template to interact with negatively charged $H_2BO_3^-$ and HSO_4^-. Driven by the electrostatic interaction between the CTAB chains, $H_2BO_3^-$, HSO_4^-, and threonine, self-assembled micelles formed at the interface. After the pyrolysis of micelles, HPC spheres were achieved.[105] In addition to cationic surfactants, triblock polymers are nonionic structure-directing agents that produce HPCs with ordered mesoporous walls, the most popular one of which is poly(ethylene glycol)–poly(propylene glycol)–poly (ethylene glycol), for example, F127,[106–110] and poly (ethylene oxide)–poly(propylene oxide)–poly(ethylene oxide) (PEO–PPO–PEO), for example, P123.[111–113]

F127 and P123 have different molecular weights, but similar structures, which are composed of a central hydrophobic block of polypropylene (PP) glycol/oxide and hydrophilic blocks of polyethylene glycol/oxide at two chain ends. All oxygen atoms of the polymer chains are capable of interacting with hydrogen atoms of carbon feedstocks via hydrogen bonds or covalent bonds. The triblock polymer micelles filled with carbon precursors are spherical or hexagonal and are finally transformed into HPCs with ordered mesoporous walls. An example is shown in Figure 4A; pyrrole was first modified and grafted with hydrophilic carboxyl groups, and then P123 was utilized as the soft template to promote the uniform assembly and polymerization of hydrophilic PEO and functionalized pyrrole.[112] During the above synthesis, macroporous structures were formed due to tuning the electrostatic interaction through pH and microphase separation during the formation of porous polymer networks. Mesoporous structures were generated by the structural directing triblock copolymer micelles, which were subsequently removed by calcination to give rise to mesopores with high-degree periodicity (Figure 4B,C). The micropores were created by the removal of interpenetrating block copolymer tails into the polymer matrix and partly from the cleavage of the butanoic acid group. Another example is the combined use of a nonionic surfactant (F127) and an anionic surfactant (sodium dodecyl sulfate) developed by Sun et al.[114] As shown in Figure 4D, chitosan-protic salt [Chit][HSO_4] was used as a source of carbon, nitrogen, and sulfur, while F127 and sodium dodecyl sulfate (SDS) served as the mesoporous and macroporous soft templates, respectively. During the curing process, the surfactant templates and precursors melt at elevated temperatures, which leads to a homogeneous, mobile reaction and excellent compatibility of various components. Due to the existence of abundant hydroxyl groups and protonated amino groups in the molecular structure of [Chit][HSO_4], aggregation occurs easily between [Chit][HSO_4], F127, and SDS by the driving force of hydrogen bonding, charge attraction, van der Waals forces, and so forth, contributing to the formation of micelles. During pyrolysis, F127 and SDS are gradually removed to form a 3D interconnected honeycomb-like structure, while the micropores are derived from the release of SO_2 and NH_3 by the decomposition of [Chit][HSO_4] during pyrolysis.

Although soft template agents can be removed easily during the pyrolysis and lead to the formation of ordered mesoporous walls of HPCs, usually, the electrostatic self-assembly requires organic solvents for the reactions between carbon precursors and surfactants and takes a long time. Thus, more attention needs to be paid to the use of aqueous or solvent-free synthesis systems for the large-scale production of HPCs.

2.3 | Hard/soft combined templates

Another method for the fabrication of HPCs is the use of a combination of hard and soft templates. As is known, hard

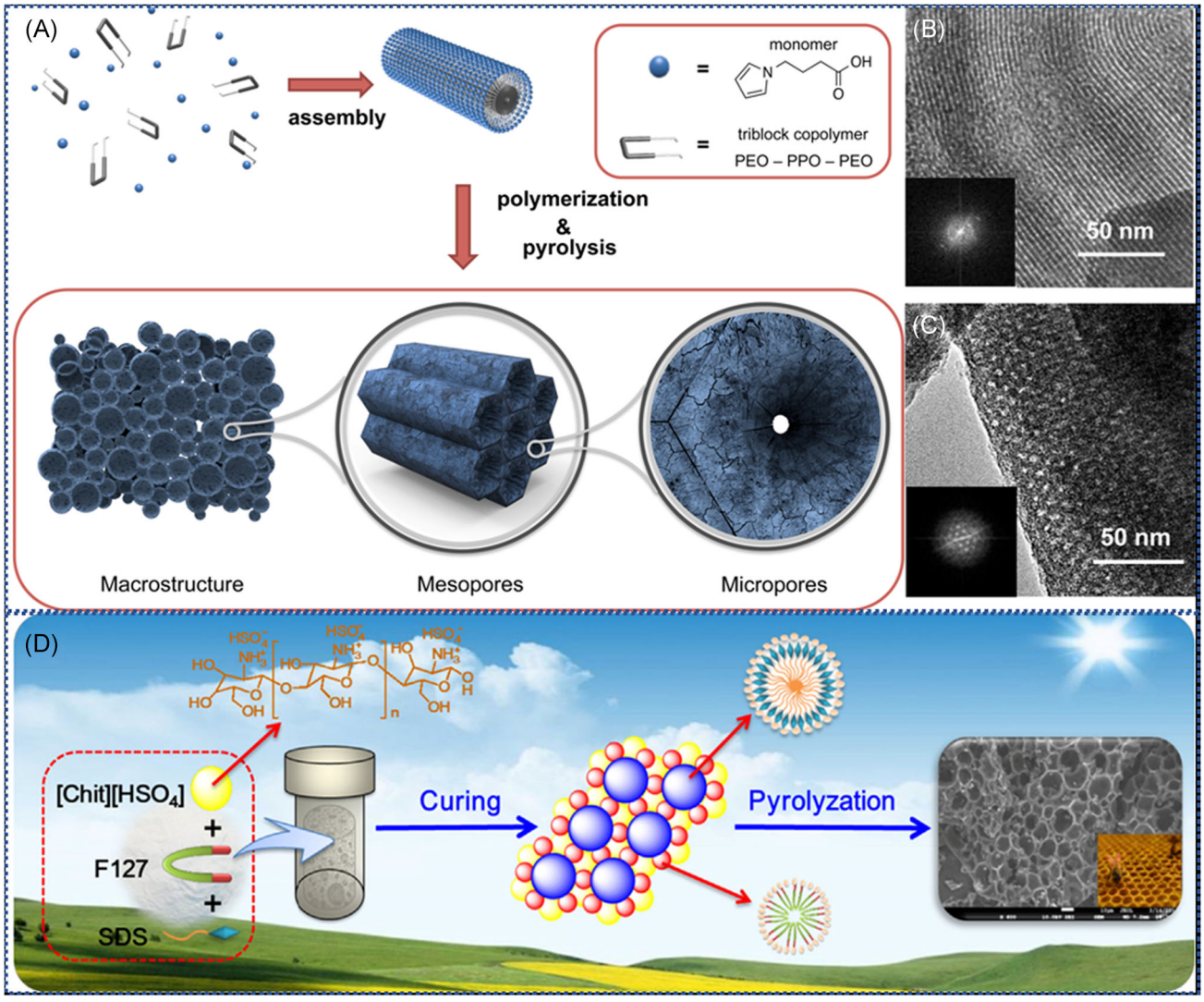

FIGURE 4 Synthesis of hierarchical porous carbons (HPCs) through soft templates. (A) Schematic of the synthesis of HPCs using P123 as a soft template and modified polypyrrole as a carbon source. (B,C) Transmission electron microscopy images of HPCs demonstrating the [110] and [001] directions of the hexagonal array, respectively; the insets show fast Fourier transfer diffractograms. (D) Procedure for the preparation of nitrogen, sulfur co-doped HPCs (N/S-HPCs) with the combination of F127 and sodium dodecyl sulfate (SDS) as soft templates. (A–C) Reproduced with permission: Copyright 2015, American Chemical Society.[112] (D) Reproduced with permission: Copyright 2019, Elsevier[114]

templates have rigid structures and mostly can withstand a high-temperature treatment to prevent the shrinkage of carbon precursors during carbonization, while soft templates help to form the periodic nanoporous structures of HPCs. Thus, the combination of hard and soft templates is believed to be an effective approach for the construction of 2D and 3D ordered HPCs. In particular, the pore size of HPCs can be tuned in a wide range using these methods, which is difficult to achieve when only using soft or hard templates. Liu et al.[115] prepared a novel type of N-HPC with unique ordered 2D hexagonal mesostructures and interconnected micropores, the process of which is schematically shown in Figure 5A. At first, the amino groups in octa (aminophenyl) silsesquioxane (OAPS) could strongly interact with the PEO blocks of PEO–PPO–PEO via intermolecular hydrogen bonds, ensuring the microphase separation through the universal solvent evaporation-induced self-assembly process and resulting in highly ordered mesostructured hybrids. During thermal curing and subsequent pyrolysis in a nitrogen atmosphere, the aggregates (i.e., micelles) of the block copolymer surfactants can be eliminated and produce ordered open mesopores, while the cross-linked OAPS is transformed into a carbon skeleton containing amorphous silica nanoparticles. After the removal of silica nanoparticles, the resulting HPC has abundant silica-imprinted uniform micropores (~1 nm)

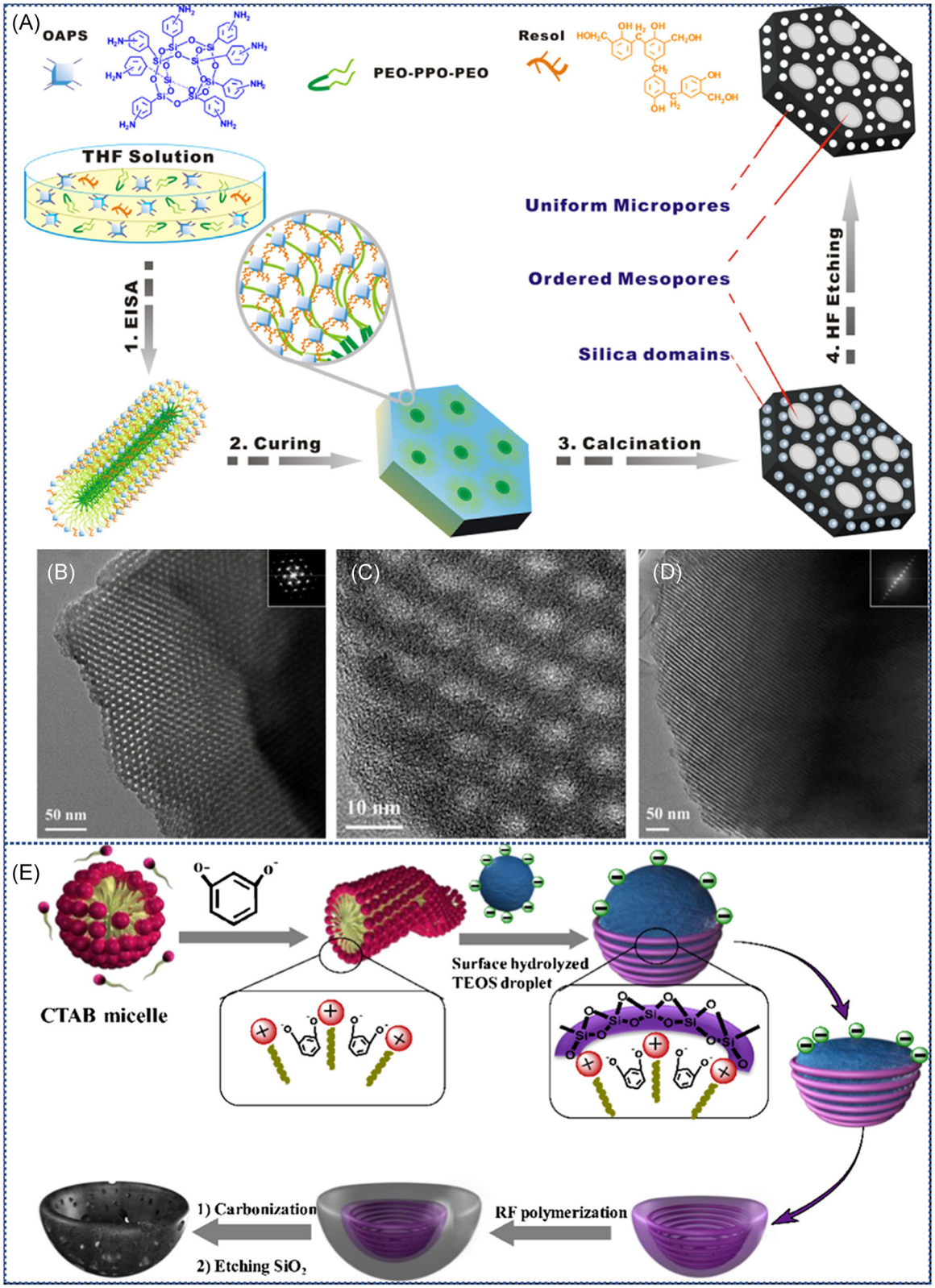

FIGURE 5 Preparation of hierarchical porous carbons (HPCs) by hard/soft combined templates. (A) Schematic diagram of the synthesis of HPC with the combination of a silica hard template and a P123 soft template. (B) Transmission electron microscopy (TEM) and (C) high-resolution TEM (HRTEM) images of HPC viewed along the [001] direction. (D) TEM image of HPC viewed along the [110] direction. The insets in (B) and (D) show the corresponding fast Fourier transform diffractograms. (E) Illustration of synthesis of HPCs with the combination of a CTAB soft template and SiO_2 hard templates. (A–D) Reproduced with permission: Copyright 2016, Elsevier.[115] (E) Reproduced with permission: Copyright 2016, Elsevier.[116] CTAB, hexadecyl trimethylammonium bromide; EISA, evaporation-induced self-assembly; HF, hydrofluoric; OAPS, octa(aminophenyl) silsesquioxane; PEO, poly(ethylene oxide); PPO, poly(propylene oxide); RF, radiofrequency; TEOS, tetraethyl orthosilicate

(Figure 5C), interconnecting the highly ordered mesopores (~4 nm) (Figures 5B and 4E). As expected, the unusual pore structure endows the obtained HPCs with a high Brunauer–Emmett–Teller (BET) surface area of 2144 $m^2 g^{-1}$ and a total pore volume of 1.47 $cm^3 g^{-1}$, showing good capability for sulfur loading and enhancement of Li–S cells. Furthermore, when using Pluronic F108 with a higher PEO/PPO ratio as a mesoporous template to substitute PEO–PPO–PEO, HPCs with 3D cubic mesostructures and well-defined micropores were also synthesized. Similarly, a facile strategy for producing bowl-like HPCs was developed by Zhang et al.[116] involving the self-assembly of worm-like CTAB micelles with polymerization of silica/RF at the interface of TEOS droplets (Figure 5E). After calcination and SiO_2 etching, the bowl-like HPCs obtained showed a high BET surface area of 1255 $m^2 g^{-1}$ and a high pore volume of 1.87 $cm^3 g^{-1}$. More interestingly, by controlling the shape of micelles of a CTAB-coated resorcinol aggregate with varied ethanol–water ratios, porous silica/carbon nanomaterials with various morphologies including nanorods and nanospheres can also be prepared.[117,118] All of these results demonstrate the versatility and adjustability of the combined hard/soft templating method to produce HPCs with controlled structures and morphologies.

2.4 | Self-templates

Despite the fact that templating methods are general and versatile to control the nanoporous structures of HPCs, there are still some challenges including the requirement of sophisticated preparation technology, and high-cost templates, which might restrict the large-scale production of HPCs for Li–S batteries. Therefore, self-templating methods have been proposed and have gained popularity in recent years due to their facile nature. Self-templating methods can also be considered template-free methods, which means synthesizing HPCs through the direct calcination of carbon precursors without the addition of structure-directing agents. On the basis of original precursors used in the synthesis systems, self-templated HPCs can be categorized into biomass-derived carbon and synthetic material-derived carbon.

Biomass-derived HPCs: Biomass, the main ingredient in the formation of fossil fuels, has attracted considerable attention, serving as both self-templates and carbon feedstocks for the generation of HPCs due to tailorable physical/chemical properties, natural abundance, and low costs.[119] Various types of biomasses have been studied for the preparation of HPCs, including plant-derived materials (bark of tree,[120] leaves,[121,122] cassava,[123] coffee ground,[124] green algae,[125] waterweed,[126] banana peels,[127] cotton,[128] tobacco,[129] etc.), animal-derived materials (eggshell membrane,[130] pig bone,[131] crab shell,[132] silk cocoon,[133] etc.), and microorganisms (filamentous fungi,[32] *Aspergillus Oryzae*,[134] and bacterial cellulose[135]). Usually, biomass inherently contains organic polymers and elements of N, S, and P. During the pyrolysis and decomposition of biomass, abundant pores are generated and the carbon skeleton can be doped with heteroatoms (e.g., N, S, and P). As a result, the heteroatom-doped HPCs obtained from biomass could effectively adsorb PS and show excellent electrochemical performances. Tree leaves containing hierarchically arranged epidermis and parenchyma cells were explored to produce HPCs by Arumugam et al.[121] via one-step carbonization under an argon atmosphere without using time-consuming templates or multistep treatments. Benefiting from the perfectly retained anatomically layered structure of the leaves, the as-produced HPCs film showed a layered hierarchical structure with abundant stomata. As is known, the pores and stomata of the lower epidermis serve as water reservoirs and exchange openings in vascular plants. Similarly, the inherited pores can serve as pathways for ion transport, promoting the chemical reactions in energy storage devices.

Recently, N and P dual-doped spore-derived carbon with a porous maze structure consisting of crosslinked nanofolds was developed by Zhong et al.[134] In their work, rice was used as the culture medium for the growth of *Aspergillus oryzae* spores. After inoculation with *Aspergillus oryzae*, the inoculated rice was transferred to an incubator and kept for 1 week. Subsequently, the *Aspergillus oryzae* spores could be easily harvested by a filter screen, and then the proteins and polysaccharides of spores could be converted into carbon after heat treatment at 900°C under argon protection. As can be seen in Figure 6, the spore-derived carbon shows a special concaved porous morphology with a rugged texture and a wrinkled maze-like secondary architecture. The structure consists of interconnected nanofolds with diameters of 2–3 μm (Figure 6B–D), and the nanofold structure is made up of interconnected carbon wrinkles. Simultaneously, the carbon skeleton can provide a continuous conductive network for fast electron transport. The hierarchical hollow porous structure observed from the TEM images (Figure 6E and inset) is amorphous carbon confirmed by the selected area electron diffraction pattern and the disordered lattice fringe in the high-resolution TEM image. Furthermore, the corresponding energy-dispersive X-ray spectroscopy (EDX) elemental mapping images demonstrated intrinsic doping with N and S atoms, which are beneficial for fast charge transfer and capacity retention.

Synthetic self-templated HPCs: Despite the aforementioned merits, there is also an intrinsic challenge

associated with biomass-derived HPCs; namely, obstacles in accurately tailoring the pore size and pore distribution as the porous structure is inherited from the natural precursor. To circumvent this difficulty, synthetic materials with pre-designed porous precursors or tunable structures were selected as carbon sources, such as metal–organic frameworks (MOFs),[136–144] graphene/graphene oxide,[31,145–147] graphitic C_3N_4 (g-C_3N_4),[64] and decomposable salts.[148]

MOFs, composed of organic ligands and metal cores, have been receiving attention for fabrication of HPCs due to their inherent ordered porous structures.[149,150] Klose et al.[136] selected commercial iron-containing MOF, Basolite F300, as a proof of concept to prepare HPCs using a thermal decomposition approach. Basolite F300 is a coordinated complex with an iron ion core and 1,3,5-benzenetricarboxylate ligands. During the pyrolysis process, 1,3,5-benzenetricarboxylate acted as a sacrificial carbon precursor, while iron acted as a catalyst for the growth of graphitic carbon to enhance the graphitization and electrical conductivity of MOF-derived carbon. Apart from MOFs, prefabricated g-C_3N_4 was also used as a template for the synthesis of hierarchical porous graphene using a two-step calcination method,[64] during which graphene was simultaneously doped with N and S atoms using dithiooxamide as a doping reagent. Confirmed by N_2 adsorption–desorption isotherms, an intense adsorption curve appeared at low

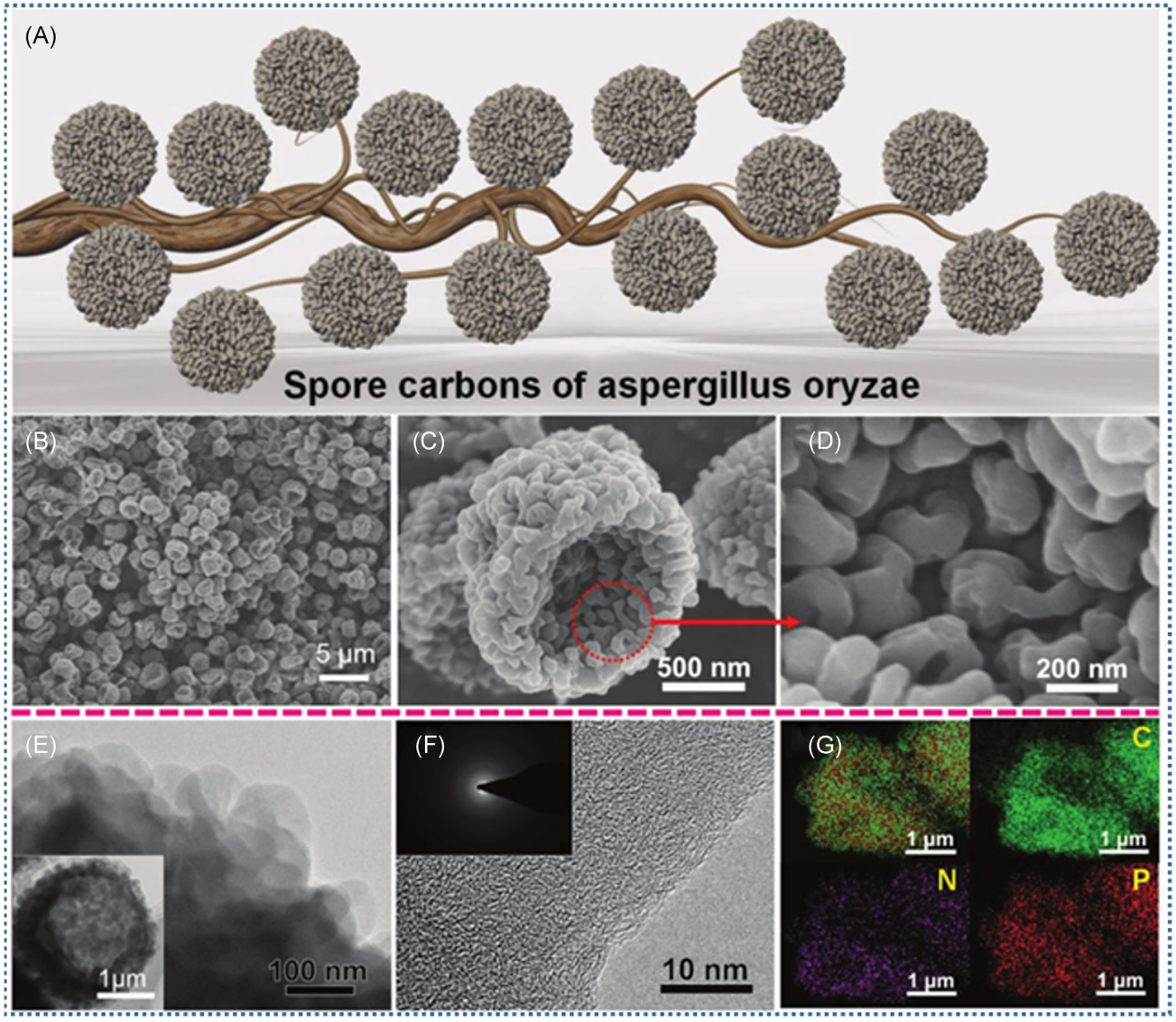

FIGURE 6 Synthesis of hierarchical porous carbons through self-templates. (A) Schematic illustration of the spore carbon synthesized from *Aspergillus oryzae*. (B–D) Scanning electron microscopy images and (E,F) transmission electron microscopy images of spore carbon. (G) Energy-dispersive X-ray spectroscopy elemental mapping images of spore carbon. (A–G) Reproduced with permission: Copyright 2018, Wiley[134]

relative pressure, demonstrating the typical presence of micropores. The H3-type hysteresis was accompanied by capillary condensation in mesoporous structures, implying the presence of hierarchical pores. The corresponding pore-size distribution also confirmed the hierarchical porous structure containing the pores in different ranges such as 0.5–1.7 nm (micropores) and 3.5–35 nm (mesopores).

2.5 | Combination of templating and activation methods

Activation methods are widely adopted to further tune the pore sizes, SSA, and pore volume of carbon materials. Depending on the activating agents used, the activation methods can be divided into physical and chemical activation.[151] The physical activation method is performed by inert-atmosphere calcination, followed by high-temperature (600–1200°C) activation with the introduction of suitable gasifying agents (CO_2,[135,152–157] NH_3,[158,159] Cl_2,[160–163] and steam[164]). In contrast, chemical activation includes mixing of carbonaceous materials and activating agents (e.g., KOH,[29,84,165–199] NaOH,[200] K_2CO_3,[201,202] H_3PO_4,[203–205] etc.), followed by calcination at a lower temperature (400–900°C). Nearly two-thirds of our reviewed publications on activated HPCs for Li–S cells adopted KOH as the activating agent because it can promote the creation of micropores, high micropore volume, and a very high SSA of up to 3000 $m^2 g^{-1}$. The activating process is associated with many variables such as the experimental parameters (temperature, KOH/carbon ratio, etc.) and the reactivity of KOH with different precursors. Generally, the reaction between carbon and KOH starts with solid–solid reactions, followed by solid–liquid reactions, including the reduction of potassium compounds to metallic potassium, the oxidation of carbon to CO_2 and carbonate, and the formation of various active intermediates (CO_2, H_2O, H_2).[206,207] Thus, three main activation mechanisms for KOH activation of carbon have been widely accepted[206–210]: (1) the redox reactions between various potassium compounds with carbon are responsible for generating the pore network; (2) the formation of intermediates (e.g., H_2O and CO_2) in the activation process could positively contribute to further production of porosity through the gasification of carbon; (3) the intermediate of metallic potassium is able to efficiently intercalate into the carbon lattices, which gives rise to the expansion of the carbon lattices. After removing the intercalated metallic potassium and other potassium compounds by washing/etching, HPCs with enhanced porosity and SSA were created due to the expanded carbon lattices. An example of a KOH-activated silk cocoon-derived porous HPC is shown in Figure 7A,[194] which could be simply obtained by precarbonization of silk cocoon, followed by KOH activation. With an increase in the weight ratio of KOH/carbon from 0.5 to 1.5, carbon could react more with KOH, leading to a much higher SSA of HPC-1.5 (HPC-X, X represents the weight ratios) than that of HPC-0.5. The N_2 adsorption–desorption isotherms of HPCs (Figure 7B) were identified as type IV with a typical H1 hysteresis loop according to the IUPAC classification.[211] The pore-size distribution of HPCs (Figure 7C) demonstrated the main micro–mesoporous structures, which originated from the etching of carbon skeleton and gas (i.e., H_2 and CO_2) generation during activation.[208]

By combining an MXene hard template, an F127 soft template, and chlorine activation, a series of 2D–2D heterostructures consisting of MXene-derived carbon (MDC) and ordered mesoporous carbon (OMC) were prepared (Figure 7D). In the synthesis, layered MXene can provide interspaces between F127 and resol, while F127 serves as a mesopore agent, and chlorine activation can finally remove the titanium and etch the carbon skeleton to generate abundant micropores. Due to a combination of these merits, HPCs with layer-by-layer motif architectures and ordered pores (Figure 7E,F) were obtained, which prevented the restacking and blocking of layered structures. In addition, the SSA (1021 $m^2 g^{-1}$) and pore volume (1.62 $cm^3 g^{-1}$) of MDC–OMC were greatly enhanced after chlorination compared with Mxene–OMC (84 $m^2 g^{-1}$ for SSA, 0.19 $cm^3 g^{-1}$ for pore volume).

In conclusion, herein, we briefly summarize the features of five strategies for the synthesis of HPCs, including the hard-templating method, the soft-templating method, the hard and soft-templating method, the self-templating method, and the templating/activation combined method. (1) The hard templating method is efficient in tuning the morphologies, particle sizes, and pore structures of HPCs by adjusting the structures and concentration of predesigned templates. (2) The soft templating method can lead to the formation of HPCs with ordered mesoporous walls, and in particular, the templates can be removed easily by calcination. (3) The hard and soft templating method is very effective for the construction of 2D and 3D ordered HPCs. Hard templates are stable even at high temperatures, which can offer rigid and stable scaffolds to avoid framework shrinkage of carbon precursors during carbonization, while soft templates can help to form periodic nanopores. (4) Template-free methods for synthesizing HPCs are beneficial in terms

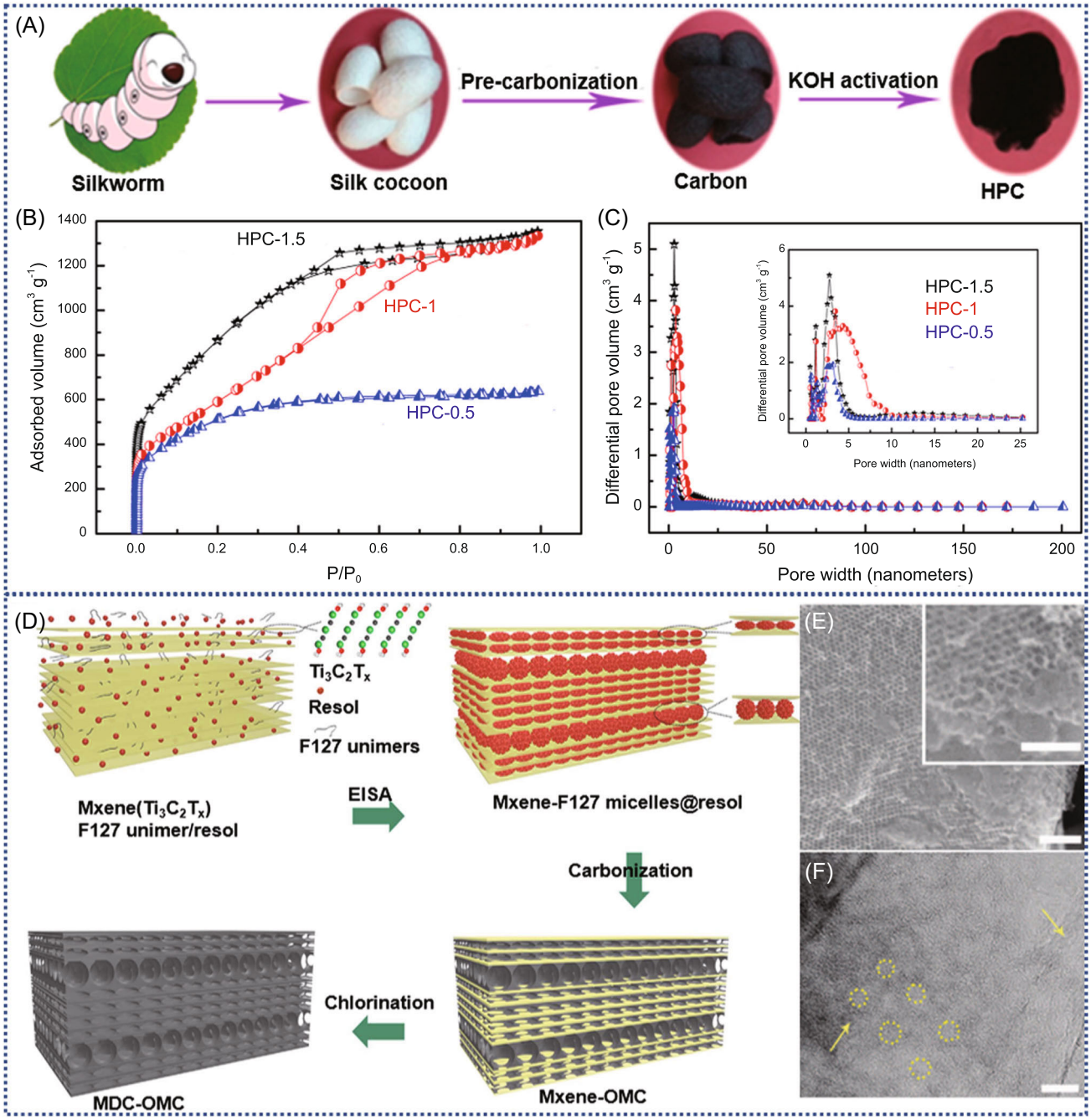

FIGURE 7 Synthesis of hierarchical porous carbons (HPCs) through templating and activation methods. (A) Schematic diagram of synthesis of HPCs by pyrolysis of silk cocoon, followed by KOH activation. (B) N_2 adsorption−desorption isotherms and (C) pore size distributions of HPCs. (D) Schematic illustration of the synthetic route for producing MDC–OMC. (E) Top-view SEM and (F) TEM images of the MDC–OMC. Scale bars are 100 nm for (E), inset in (E), and 20 nm for (F). (A–C) Reproduced with permission: Copyright 2014, American Chemistry Society.[133] (D–F) Reproduced with permission: Copyright 2017, Nature Publishing Group.[163] MDC, MXene-derived carbon; OMC, ordered mesoporous carbon; SEM, scanning electron microscope; TEM, transmission electron microscope

of the direct calcination of carbon feedstocks without using templates, which is time-saving and economical. (5) The templating/activation combined method can integrate the strengths of templates and activation: templates can promote the formation of ordered mesopores or macropores, and the activation step can endow HPCs with abundant micropores, further improving the specific surface area and pore volume. It is often not possible to classify a certain method as the ideal method for producing HPCs, but we can select the suitable method according to the microstructures required for the specific application in focus (e.g.,

sulfur cathode, interlayers, and lithium anode), which will be elaborated in the following sections.

3 | NOVEL SULFUR/HPC CATHODES AND PARAMETERS AFFECTING BATTERY PERFORMANCE

As mentioned in the introduction, the main challenges such as volume change, insulating nature, and the "shuttle effect" originating from the use of a sulfur cathode hinder the commercialization of Li–S batteries. Since the work carried out by Liang et al.,[29] HPCs containing bimodal/trimodal pores have shown singificantly enhanced electrochemical performances for Li–S cells. Basically, conductive carbon materials can facilitate electron transport and improve sulfur utilization and reaction kinetics. In addition, the micro- and mesopores in HPCs can provide a high surface area to improve the contact between sulfur and carbon, and provide abundant active sites for adsorption of PSs. The meso- and macropores can accommodate sulfur, mitigate the volume change, and provide pathways for ions margination.

The performance of a Li–S battery is highly correlated to the pore structure of carbon hosts. In this section, we discuss the correlation between the characteristics of HPCs and the performances of S/HPCs cathodes of Li–S batteries. As summarized in Table 1, HPCs can be categorized into three classes according to the pore-size distributions for Li–S cells, namely, micro/mesoporous carbon, micro/meso/macroporous carbon, and meso/macroporous carbon. On the basis of the analyses, micro/mesoporous carbon is the most used one in the published work, accounting for 63.5%, while the percentages of micro/meso/microporous carbon and meso/microporous carbon are 28.6% and 7.9%, respectively. As is known, some key parameters (pore volume, SSA, pore size and order degree of pores, heteroatom doping) of HPC hosts strongly affect sulfur/carbon cathodes (sulfur content and mass loading) and further influence the electrochemical performances (initial capacity, cycle, and rate performance). However, to date, the correlation between the structure of HPCs, the sulfur content and loading of the carbon–sulfur cathodes, and the electrochemical performance of the Li–S cells has not been comprehensively and systematically summarized and discussed. Therefore, in this part of the review, we focus our attention on the effects of pore structures (pore volume, SSA, degree of order, heteroatom doping) of HPCs on the performance of carbon–sulfur cathodes.

3.1 | The correlation between pore volume of HPCs and performances of S/HPCs cathodes

As one of the most significant parameters, the pore volume of HPCs, which is largely dependent on the size and ratio of large mesopores and macropores, strongly influences the sulfur content of S/C composites and battery performances. In fact, the theoretical maximum sulfur content loaded in the pores of HPCs can be calculated based on the following equation when the volume expansion is not taken into account:

$$\varphi = \frac{V_p \times \rho_S}{V_p \times \rho_S + 1}, \quad (1)$$

where φ is the sulfur content (wt%) of sulfur/HPCs, V_p ($cm^3\,g^{-1}$) is the pore volume of HPCs, and ρ_S is the density of sulfur ($2.07\,g\,cm^{-3}$). In consideration of the volume expansion due to the different densities of sulfur and lithium disulfide, the sulfur content when storing maximum Li_2S is expressed by the following formula:

$$\varphi = \frac{V_p \times \rho_{Li_2S} \times M_s}{V_p \times \rho_{Li_2S} \times M_s + M_{Li_2S}}, \quad (2)$$

where M_S is the molecular weight of sulfur ($32\,g\,mol^{-1}$), ρ_{Li_2S} is the density of Li_2S ($1.66\,g\,cm^{-3}$), and M_{Li_2S} is the molecular weight of Li_2S ($46\,mol^{-1}$). For example, if the volume expansion is not considered and sulfur is fully filled in the pores, the minimum pore volume of HPCs should be 1.13 and $1.93\,cm^3\,g^{-1}$ for the sulfur contents of 70 and 80 wt% of S/HPC composites, respectively. While the volume expansion of sulfur is taken into account, the expected pore volume of HPCs for filling with the same contents of sulfur should be larger than 2.02 and $3.46\,cm^3\,g^{-1}$, respectively.

An example of the pore volume affecting the performances of S@HPCs cathodes was given by Kang et al.[188] Three coal-derived porous carbons (CDPC-1, CDPC-2, and CDPC-3) with different SSAs (968, 3036, and $3343\,m^2\,g^{-1}$ for CDPC-1, CDPC-2, and CDPC-3, respectively) and pore volumes (0.46, 1.65, and $2.10\,cm^3\,g^{-1}$ for CDPC-1, CDPC-2, and CDPC-3, respectively) corresponded to the theoretical sulfur loadings of 48.7, 77.4, and 81.4 wt%, respectively, without considering the volume expansion. However, according to thermogravimetric (TG) analyses (Figure 8A), the sulfur contents of the synthesized CDPC/S-1, CDPC/S-2, and CDPC/S-3 were 65, 76, and 75 wt%, respectively. Thus, there were distinct characteristics of sulfur for CDPC/S-1 in both the X-ray diffraction (XRD) patterns (Figure 8B) and Raman spectra (Figure 8C), indicating the existence of excessive

TABLE 1 A summary of the characteristics and performance of typical HPC/sulfur composite cathodes for Li–S batteries

Materials	Preparation methods	Pore structures	SSA ($m^2\ g^{-1}$)	Pore volume ($cm^3\ g^{-1}$)	S content (%)	S content (electrode,%)	S loading (mg cm^{-2})	Initial discharge capacity (mAh g^{-1})[a]	Cyclingperformance (mAh g^{-1}) [a]	Rate performance (mAh g^{-1}) [a]	Reference
S@HPC	Soft template + KOH activation	Micro/ mesopores	1566	-	11.7	-	0.25	1585@1.5 C	805@1.5 C (30 cycles)	-	[29]
S@HPC-graphene	Silica + graphene oxide + KOH	Micro/ mesopores	1558	1.1	74	59.2	0.56–0.75	1370@0.5 C	860@1 C (100 cycles)	860@5 C, 510@10 C	[212]
S@HPC	Urchin-like silica template	Micro/ mesopores	541	0.47	60	48	1.2	1390@0.2 C	~530@1 C (600 cycles)	610@5 C	[70]
S@Co, N-HPC	NaCl + $Co(NO_3)_2$ salt template	Micro/ mesopores	588	-	60	48	~1.0	1150.4@0.2 C	708@0.2 C (100 cycles)	572@1 C	[213]
S@HPC	Siliceous + Cl_2 activation	Micro/ mesopores	2449	4.97	80	68	3.46	1165@0.1 C	860@0.1 C (100 cycles)	766@0.5 C	[160]
S@HP graphene	Salt template(Nickel acetate)	Micro/ mesopores	2700	2.5	72.3	~57.8	-	1150@0.5 C	854@0.5 C (200 cycles)	720@3 C	[214]
S@HPC	Silica foam + Cl_2 activation	Micro/ mesopores	2800	2.6	73	58.1	2.89	1070@0.1 C	790@0.1 C (100 cycles)	Over 600@0.5 C	[161]
S@CNTs/ graphene-HPC	Layered metal hydroxide + KOH	Micro/ mesopores	513	0.853	50	45		1070@1 C	877@1 C (150 cycles)	810@10 C	[169]
S@HPC	Polymer–silica–surfactant template	Micro/ mesopores	957	1.46	65.3		~1.0	1398@0.2 C	831@0.2 C (200 cycles)	753.2@4 C	[91]
S@HP CNTs	Layered metal hydroxide template	Micro/ mesopores	649	1.55	60	54	1.0–1.5	844@1 C	530@1 C (450 cycles)	570@4 C	[94]
S@HPC	PANi + KOH activation	Micro/ mesopores	4073	2.26	-	-	3.2	1270@0.2 C	980@0.2 C (200 cycles)	~600@2 C	[215]
S@HP CNFs	Ni $(Ac)_2$ template	Micro/ mesopores	252	0.48	57.7	46.2	0.3-0.4	845@0.25 C	657@0.25 C (100 cycles)	438@2 C	[77]
S@N-HPC	Magnesium citrate + NH_3 activation	Micro/ mesopores	1290	3.04	76.2	~61	1.14	934@1 C	(600@1 C) (300 cycles)	671@4 C	[73]
S@N-HPC nanosheets	Magnesium/potassium citrate + NH_3 activation	Micro/ mesopores	1735	1.71	75	56.2	1.13	1209@0.2 C	486@1 C (500 cycles)	493@4 C	[216]

TABLE 1 (Continued)

Materials	Preparation methods	Pore structures	SSA ($m^2\ g^{-1}$)	Pore volume ($cm^3\ g^{-1}$)	S content (%)	S content (electrode,%)	S loading (mg cm^{-2})	Initial discharge capacity (mAh g^{-1})[a]	Cyclingperformance (mAh g^{-1}) [a]	Rate performance (mAh g^{-1}) [a]	Reference
S@HP CNFs	Silica + KOH activation	Micro/ mesopores	2480	1.84	66	52.8	~2.0	1071@0.5 C	965@0.5 C (100 cycles)	626.2@2 C	[217]
S@HPC-CNTs	$Ni(OH)_2$ template	Micro/ mesopores	605	-	65	52	1.0	714@1 C	465@1 C (250 cycles)	~500@2 C	[78]
S@HPCs	ZnO template + CO_2 activation	Micro/ mesopores	1365	3.13	66	52.8	1.5	~1000@0.6 C	~700@0.6 C (50 cycles)	-	[155]
S@HPCs	Soybean + KOH activation	Micro/ mesopores	1500	0.7	80	56	~2.0	868@0.5 C	460@0.5 C (800 cycles)	710@1 C	[176]
S@HPCs	Rice husk-derived	Micro/ mesopores	525	0.488	56	44.8	1.0	834@0.5 C	~600@0.5 C (500 cycles)	500@5 C	[218]
S@HPCs	Zinc citrate templates	Micro/ mesopores	2600	2.46	66.7	56.7	2.5	1225@0.1 C	950@0.1 C (100 cycles)	600@2 C	[219]
S@HP graphene	CaO template	Micro/ mesopores	572	0.93	68	54.4	~2.0	798@0.2 C	666.2@0.5c (150 cycles)	656@5 C	[83]
S@HPCs	Layered $Ti_2AlC + Cl_2$ activation	Micro/ mesopores	1264	1.89	50	40	1.2	1229@0.5 C	724@0.5 C (200 cycles)	621@5 C	[162]
S@N,P-HPCs	Mushroom + H_2PO_4 activation	Micro/ mesopores	788	0.768	50	40	1.2–1.3	1358@0.1 C	729@0.1 C (100 cycles)	213@2 C	[203]
S@HPCs	$Mg(OH)_2$ templates	Micro/ mesopores	2226	4.9	80	64	1.5	970@1 C	700@1 C (300 cycles)	646@5 C	[92]
S@N,S HPCs	Pyrolysis of lotus plumule + KOH	Micro/ mesopores	2488	0.99	85	59.5	2.38	1285@0.5 C	952@0.5 C (300 cycles)	1201@1 C	[178]
S@HP CNFs	Nickel–sulfate templates	Micro/ mesopores	500	0.65	60	42	~1.0	977@0.5 C	636@0.5 C (200 cycles)	433@5 C	[88]
S@HPC	Pyrolysis of polypyrrole + KOH	Micro/ mesopores	3271	2.8	80	56	2.4	1411@0.5 C	592@0.5 C (80 cycles)	678@0.6 C	[180]
S@N-HPC	Enteromorpha + KOH activation	Micro/ mesopores	1425	0.59	75	52.5	1.0	1001@0.1 C	~800@0.1 C (100 cycles)	500@1 C	[181]
S@N-HPC	F127 + P123 + NH_3 activation	Micro/ mesopores	1565	0.88	68	54.4	2.5	1095@0.2 C	708@0.2 C (100 cycles)	~400@1 C	[159]

(Continues)

TABLE 1 (Continued)

Materials	Preparation methods	Pore structures	SSA ($m^2\ g^{-1}$)	Pore volume ($cm^3\ g^{-1}$)	S content (%)	S content (electrode,%)	S loading (mg cm^{-2})	Initial discharge capacity (mAh g^{-1})[a]	Cyclingperformance (mAh g^{-1}) [a]	Rate performance (mAh g^{-1}) [a]	Reference
S@HPC	SDS/CTAB templates + KOH	Micro/ mesopores	642	0.51	77.2	~54	2.4	921@0.12 C	762@0.12 C (150 cycles)	~720@1 C	[200]
S@HPC	Rice husk-derived + $ZnCl_2$	Micro/ mesopores	1199	0.752	33	19.8	0.31–0.79	1050@0.2 C	~600@0.2 C (100 cycles)	426@2 C	[220]
S@N-HPC nanocages	Silica colloid template	Micro/ mesopores	1187	3.98	72.7	54.5	-	1202@0.2 C	780@0.22 (60 cycles)	-	[63]
S@HPC	Mangosteen peels + KOH activation	Micro/ mesopores	3244	1.58	65	52	1.0	870@0.5 C	600@0.5 C (100 cycles)	569.2@2 C	[184]
S@HPC	Pyrolysis of polypyrrole + KOH	Micro/ mesopores	3422	1.979	70	49	2.4	1189@0.12 C	725@0.12 C (100 cycles)	520.4@0.6 C	[221]
S@N-HPC	MOF-derived	Micro/ mesopores	730	0.81	74	51.8	-	1341@0.5 C	695@0.5 C (100 cycles)	354@5 C	[142]
S@HPC	Oil palm shells + KOH/ K_2CO_3	Micro/ mesopores	1449	0.80	60	48	0.57	1105@0.12 C	819@0.12 C (100 cycles)	660@1 C	[222]
S@O,N-HPC	Pyrolysis of coffee grounds	Micro/ mesopores	1018	0.48	47.6	38.1	2–2.5	1150@0.2 C	613@0.2 C (100 cycles)	331@1 C	[124]
S@N-HPC	Pyrolysis of green algae	Micro/ mesopores	101	0.54	63	50.4	3.5	1327@0.1 C	757@0.1 C (100 cycles)	642@1 C	[125]
S@HPC	Soybean hulls + KOH	Micro/ mesopores	1232	~0.54	63.7	44.6	1.5	1231@0.5 C	~450@0.5 C (200 cycles)	340@1 C	[185]
S@O,S-HPC	Pyrolysis of alginate + KOH	Micro/ mesopores	1454	1.059	60	42	~1.0	1119@1 C	713@1 C (200 cycles)	-	[186]
S@O-HPC	Pyrolysis of balsa + KOH	Micro/ mesopores	3068	1.37	80	64	~1.5	1385@0.1 C	925@0.1 C (100 cycles)	462@2 C	[223]
S@N-HPC	Pyrolysis of MOF	Micro/ mesopores	1832	1.26	70	49	1.6	1343@0.5 C	1002@0.5 C (300 cycles)	758@2 C	[143]
S@HPC	Silica + PS templates	Micro/ mesopores	1389	1.16	66.7	54.7	3-4	~1200@0.1 C	660@0.1 C (200 cycles)	~520@1 C	[57]
S@N,P-HPC	Jellyfish-derived + KOH activation	Micro/ mesopores	2307	1.889	59	42	~1.0	748@1 C	517@1 C (300 cycles)	574.2@2 C	[187]

TABLE 1 (Continued)

Materials	Preparation methods	Pore structures	SSA ($m^2\ g^{-1}$)	Pore volume ($cm^3\ g^{-1}$)	S content (%)	S content (electrode,%)	S loading (mg cm^{-2})	Initial discharge capacity (mAh g^{-1})[a]	Cyclingperformance (mAh g^{-1}) [a]	Rate performance (mAh g^{-1}) [a]	Reference
S@HPC	Pyrolysis of coal + KOH activation	Micro/ mesopores	3343	2.1	75.9	60.7	~2.0	678@0.5 C	570@0.5 C (100 cycles)	520@2 C	[188]
S@HPC	MOF-derived	Micro/ mesopores	666	1.45	75.2	75.2	~1.5	1287@0.2 C	1060@0.2 C (50 cycles)	622.6@10 C	[144]
S@N,S-HP graphene	g-C_3N_4 templates	Micro/ mesopores	461	1.31	65	45.5	~1.0	1149@0.5 C	602@0.5 C (300 cycles)	653.1@1 C	[64]
S@N,I-HPC	Urea + KI templates + KOH activation	Micro/ mesopores	2089	1.106	73.3	58.6	1.4–1.7	1284@0.1 C	917@0.1 C (100 cycles)	539@1 C	[224]
S@HPC	Silica hard template	Micro/ mesopores	641	1.42	72	57.6	~2.1	924@0.6 C	~470@0.6 C (200 cycles)	376.5@3 C	[64]
S@HPC-N-graphene	Silkworm feces + KOH activation	Micro/ mesopores	1406	1.05	60.8	48.6	1.7–1.8	1372@0.1 C	741@0.1 C (100 cycles)	451@3 C	[190]
S@HPC	Walnut shell + KOH activation	Micro/ mesopores	2164	1.29	~50	33	~1.0	1237@0.5 C	943@0.5 C (200 cycles)	758.7@2 C	[191]
S@N-HPC	$ZnCl_2$ + Silica templates	Micro/ mesopores	1188	2.73	69	56	1.0	834@0.2 C	520@0.2 C (300 cycles)	623@2 C	[225]
S@core–shell HPC	Metal oxide as templates	Micro/ mesopores	1517	2.78	83.1	66.5	3.6	942@0.2 C	741@0.2 C (200 cycles)	589@2 C	[226]
S@HPC	Mangosteen peels + KOH activation	Micro/ mesopores	3244	1.56	65	52	~1.0	860@0.5 C	591@0.5 C (100 cycles)	-	[227]
S@HPC	Pyrolysis of bamboo + KOH	Micro/ mesopores	1824	1.15	58.5	40.1	-	1481@0.1 C	711@0.1 C (50 cycles)	561@1 C	[192]
S@HPC	Na_2CO_3 template +KOH activation	Micro/ mesopores	1837	2.28	60	42	~1.5	1260@0.1 C	573@0.1 C (50 cycles)	505@3 C	[193]
S@HPC	Banana peels + KOH activation	Micro/ mesopores	2045	2.4	60	42	~1.2	1481@0.1 C	753@0.1 C (50 cycles)	~50@5 C	[194]
S@N,S-HPC	CTAB template	Micro/ mesopores	249	0.18	70	70	10.6	691@0.2 C	525@0.2 C (100 cycles)	338@1 C	[228]
S@HPC	Cyclosorus interruptus + $KHCO_3$	Micro/ mesopores	1550	0.88	66.4	39.8	-	1377@0.2 C	753@0.2 C (100 cycles)	~500@1 C	[229]

(Continues)

TABLE 1 (Continued)

Materials	Preparation methods	Pore structures	SSA ($m^2\ g^{-1}$)	Pore volume ($cm^3\ g^{-1}$)	S content (%)	S content (electrode,%)	S loading (mg cm^{-2})	Initial discharge capacity (mAh g^{-1})[a]	Cyclingperformance (mAh g^{-1}) [a]	Rate performance (mAh g^{-1}) [a]	Reference
S@N,O-HPC-rGO	GO + ice template	Micro/mesopores	481	2.14	75	60	~1.2	1065@1 C	848@1 C (300 cycles)	685@5 C	[147]
S@HPC	Silica template	Micro/mesopores	884	1.03	75	60	~1.4	1375@0.1 C	630@1 C (300 cycles)	592@5 C	[60]
S@N-HP graphene	Urea + GO	Micro/mesopores	432	1.24	72.5	58	~1.8	840@2 C	554@2 C (800 cycles)	580@3 C	[230]
S@N-HPC	NaCl + $Fe(NO_3)_3$ templates	Micro/mesopores	342	-	60	48	-	1313@0.2 C	722@0.2 C (200 cycles)	538@2 C	[231]
S@HPC	Goat hair + H_3PO_4 activation	Micro/mesopores	535	0.388	54	43.2	1.4	1185@0.05 C	489@0.2 C (300 cycles))	355@2 C	[204]
S@N,O-HPC	Rapeseed meal + KOH activation	Micro/mesopores	2431	1.49	~70	~56	2–4	1259@0.1 C	512@0.1 C (200 cycles)	426.9@2 C	[232]
S@HPC	Carbonization of glucose + KOH	Micro/mesopores	587	0.33	50	40	0.6–0.75	1420@0.1 C	750@0.1 C (100 cycles)	350@0.6 C	[168]
S@HPC	Coconut shells + KOH activation	Micro/mesopores	2259	1.23	62	49.6	-	1233@0.1 C	929@0.12 C (100 cycles)	436@1.9 C	[174]
S@HPC	Fish scale + KOH activation	Micro/mesopores	2441	1.69	58.8	~40	0.8–1.0	1039@1 C	1023@1 C (70 cycles)	686@3 C	[166]
S@HPC	Monolithic SiO_2 template	Micro/mesopores	1426	3.1	75	67.5	-	1305@0.1 C	469@0.1 C (25 cycles)	-	[66]
S@HPC	Silk cocoon + KOH activation	Micro/mesopores	3243	2.1	48.4	33.9	~0.2	1443@0.5 C	804@0.5 C (50 cycles)	500@1 C	[130]
S@N,O-HPC	Carbonization of eggshell membrane	Micro/mesopores	429	0.36	-	-	3.2	1327@0.1 C	1000@0.1 C (100 cycles)	-	[121]
S@N,O-HPC	Biomass + urea + melamine + K_2CO_3	Micro/mesopores	2988	1.94	67	60.3	2.72	1302@0.1 C	977@0.1 C (50 cycles)	-	[202]
S@HPC	Pyrolysis of MOF-5	Micro/mesopores	1645	1.18	54	37.8	-	1177@0.1 C	730@0.5 C (50 cycles)	-	[138]
S@HPC	Pyrolysis of MOF	Micro/mesopores	1124	1.0	57	45.6	~1.0	1206@0.1 C	856@0.1 C (100 cycles)	763@2 C	[139]

TABLE 1 (Continued)

Materials	Preparation methods	Pore structures	SSA ($m^2\ g^{-1}$)	Pore volume ($cm^3\ g^{-1}$)	S content (%)	S content (electrode,%)	S loading (mg cm^{-2})	Initial discharge capacity (mAh g^{-1})[a]	Cyclingperformance (mAh g^{-1}) [a]	Rate performance (mAh g^{-1}) [a]	Reference
S@N-HPC	Pyrolysis of MOF	Micro/ mesopores	620	0.54	70	49	~1.0	737@0.2 C	-	433.4@2 C	[233]
S@HPC	Pyrolysis of MOF-5	Micro/ mesopores	1798	1.56	60	48	0.5–0.7	1398@0.1 C	760@0.1 C (100 cycles)	360@1 C	[234]
S@HPC	Phenolic resin + KOH activation	Micro/ mesopores	1800	2.33	63	50.4	-	798@2 C	610@2 C (100 cycles)	615@6 C	[89]
S@HPC	Pyrolysis of Peanut hull + KOH	Micro/ mesopores	480	-	84	69.2	0.8–1.0	1198@0.3 C	610@0.3 C (100 cycles)	324@3 C	[198]
S@N, O, S-HPC	NaCl template + $ZnCl_2$ activation	Micro/ mesopores	213	0.18	70	49	1.0–1.1	1556@0.1 C	401@1 C (450 cycles)	638@3 C	[196]
S@HPC	Carbonization of pomelo peel + KOH	Micro/ mesopores	1533	0.84	75	63.8	5.1	1528@0.2 C	750@0.2 C (100 cycles)	700@2 C	[235]
S@HPC	Magnesium gluconate template	Micro/ mesopores	1560	2.6	58.6	46.9	1–1.2	939@0.3 C	731@0.3 C (150 cycles)	626@2 C	[82]
S@N-HPC nanoflower	Hierarchical silica template + NH_3	Micro/ mesopores	1151	1.94	81	64.8	1–1.3	1413@0.2 C	923@1 C (200 cycles)	829@5 C	[69]
S@HPC	Pig bond + KOH activation	Micro/meso/ macropores	2157	2.26	63	63	-	1265@0.4 A g^{-1}	643@0.4 A g^{-1} (50 cycles)	-	[131]
S@Ni, N-HPC	Ni + urea	Micro/meso/ macropores	814	-	75	75	-	~1200@0.2 C	~800@0.2 C (500 cycles)	760@2 C	[236]
S@HPC	Self-template (MOFs)	Micro/meso/ macropores,	4793	3.99	55	38.5	0.96–1.15	1472@0.24 C	662@0.24 C (40 cycles)	-	[137]
S@HPC	Na_2CO_3 templates	Micro/meso/ macropores	807	0.93	46	32.2	~1.0	999@0.3 C	899@0.3 C (100 cycles)	-	[237]
S@HPC	Self-template (MOFs)	Micro/meso/ macropores	514	~1.0	~34	~28.9	-	~1115@0.2 C	~630@0.2 C (40 cycles)	-	[136]
S@HPC	Silica spheres templates	Micro/meso/ macropores	614	1.34	66.3	53	0.7–0.84	923@2 C	564@2 C (100 cycles)	564@3 C	[55]
S@HPC graphene	Nickle foam templates	Micro/meso/ macropores	160	-	52	52	~2.0	~820@0.24 C	518@0.24 C (50 cycles)	~300@2 C	[76]

(Continues)

TABLE 1 (Continued)

Materials	Preparation methods	Pore structures	SSA ($m^2\ g^{-1}$)	Pore volume ($cm^3\ g^{-1}$)	S content (%)	S content (electrode,%)	S loading (mg cm^{-2})	Initial discharge capacity (mAh g^{-1})[a]	Cyclingperformance (mAh g^{-1}) [a]	Rate performance (mAh g^{-1}) [a]	Reference
S@HPC	$Mg(OH)_2$ templates	Micro/meso/ macropores	903	2.6	84	58.8	-	1249@1 C	562@1 C (100 cycles)	419@2 C	[91]
S@HP CNFs	Self-template + KOH activation	Micro/meso/ macropores	1354	1.27	50.6	40.5	-	1477@0.1 C	1041@0.1 C (100 cycles)	544@1 C	[172]
S@HPC-GO	Silicate template	Micro/meso/ macropores	639	0.911	60	48	~0.6	987@1 C	500@1 C (400 cycles)	505.6@5 C	[56]
S@HP nanocages	MgO template	Micro/meso/ macropores	1276	4.72	79.8	63.8	0.8–1.2	1095@0.6 C	670@0.6 C (100 cycles)	487.3@1.8 C	[73]
S@HPC	Silica templates	Micro/meso/ macropores	2088	3.17	80	68	2.3–2.9	1268@0.1 C	813@0.1 C (24 cycles)	365@1 C	[135]
S@N-HP CNTs	Xylene + KOH activation	Micro/meso/ macropores	292	0.37	66.7	53.4	0.68	1287@0.2 C	979@0.2 C (200 cycles)	817@5 C	[175]
S@HPC	F127 soft + Silica hard templates	Micro/meso/ macropores	915	4.15	78	62.4	0.8	1228@3 C	914@3 C (200 cycles)	1134@3 C	[61]
S@HPC	Tree bark-derived	Micro/meso/ macropores	528	0.72	48	48	3.2–4.2	1159@0.12 C	608@0.12 C (60 cycles)	-	[120]
S@HP-nanofibers	MOF-derived	Micro/meso/ macropores	1906	1.35	60	48	0.5	1336@1 C	904@1 C (100 cycles)	650@5 C	[140]
S@HPC	CNTs + MOF-derived	Micro/meso/ macropores	1147	3.15	70	70	2.0	1291@0.2 C	960@0.2 C (50 cycles)	650@10 C	[238]
S@N,P-HPC	Pyrolysis of polyaniline +KOH	Micro/meso/ macropores	1514	1.13	66.7	46.7	1.3	1116@0.1 C	456@1 C (500 cycles)	550@2 C	[177]
S@N-HPC	Bamboo leaves-derived	Micro/meso/ macropores	329	0.5	~70	56	1.8	728@1 C	707@1 C (200 cycles)	527@4 C	[122]
S@HPC	Na_2SO_4 template	Micro/meso/ macropores	693	1.08	85	68	1.0–1.2	772@1 C	513@1 C (500 cycles)	553@4 C	[239]
S@O-HPC	$CaCO_3$ template	Micro/meso/ macropores	1217	0.54	78	54.6	0.4	1327@0.2 C	630@0.2 C (100 cycles)	~600@1 C	[240]

TABLE 1 (Continued)

Materials	Preparation methods	Pore structures	SSA ($m^2\ g^{-1}$)	Pore volume ($cm^3\ g^{-1}$)	S content (%)	S content (electrode,%)	S loading (mg cm^{-2})	Initial discharge capacity (mAh g^{-1})[a]	Cyclingperformance (mAh g^{-1}) [a]	Rate performance (mAh g^{-1}) [a]	Reference
S@HPC yolk-shell nano-sphere	F127/CTAB soft template + Silica hard template	Micro/meso/ macropores	-	-	76	60.8	-	~700@0.5 C	~350@0.5 C (1000 cycles)	~400@2 C	[241]
S@HPC nanobelts	Polymer-derived +CO_2 activation	Micro/meso/ macropores	3445	3.18	60	48	~1.0	1577@0.1 C	752@0.1 C (100 cycles)	~800@5 C	[156]
S@HPC	NaK alloy + silica template	Micro/meso/ macropores	2032	2.77	60	45	2.0–2.5	1592@0.1 C	988@0.1 C (100 cycles)	691@1 C	[242]
S@HPC	Al_2O_3 + silica templates	Micro/meso/ macropores	287	0.61	72.1	57.7	2.52	1168@0.2 C	864@0.2 C (200 cycles)	814@2 C	[243]
S@HPC	Li_2CO_3 templates	Micro/meso/ macropores	991	1.50	61	54.9	~2.0	1059@0.2 C	797@0.2 C (200 cycles)	829@2 C	[102]
S@HP-CNTs	MnO_2 templates	Micro/meso/ macropores	1419	1.44	70	56	1.5	1127@0.2 C	947@0.2C (100 cycles)	391@4 C	[86]
S@N-HPC	Banana peels using microorganism	Micro/meso/ macropores	112.1	2.04	74.3	59.4	~1.3	1174@0.1 C	700@0.1 C (200 cycles)	430.2@2 C	[127]
S@HPC-CNTs	Pyrolysis of sodium citrate + CTNs	Micro/meso/ macropores	572	-	66	52.8	1.2–1.5	1138@2 C	522@2 C (400 cycles)	749@4 C	[148]
S@HP-CNFs	Silica template	Micro/meso/ macropores	1626	-	~56	~56	~2.2	1460@0.05 C	700@0.5 C (300 cycles)	-	[59]
S@N,P-HPC	*Aspergillus oryzae*-derived HPC	Micro/meso/ macropores	221	-	70.3	56.2	~2.0	1301@0.1 C	762@0.1 C (500 cycles)	530.5@5 C	[134]
S@HP-micro-sphere	Carbon black (self-template)	Micro/meso/ macropores	756	2.08	60	48	0.3–0.5	1006@1 C	720@1 C (1000 cycles)	691@2 C	[244]
S@N,O,S-HPC	Pyrolysis of tobacco	Micro/meso/ macropores	833	0.65	72	54	2.7	1122@0.5 C	754@0.5 C (400 cycles)	447@3 C	[129]
S@HPC	Carbonization of cotton + KOH	Micro/meso/ macropores	1286	1.15	50	40	-	1024@0.2 C	850@0.2 C (100 cycles)	550@4 C	[171]
S@HPC sphere	Carbonization of glucose + KOH	Micro/meso/ macropores	700	0.47	-	-	-	1253.5@0.1 C	877@0.1 C (50 cycles)	-	[165]

(Continues)

TABLE 1 (Continued)

Materials	Preparation methods	Pore structures	SSA ($m^2\ g^{-1}$)	Pore volume ($cm^3\ g^{-1}$)	S content (%)	S content (electrode,%)	S loading (mg cm^{-2})	Initial discharge capacity (mAh g^{-1})[a]	Cyclingperformance (mAh g^{-1}) [a]	Rate performance (mAh g^{-1}) [a]	Reference
S@N-HPC	Silica + MOF templates	Micro/meso/ macropores	2546	13.4	76	54.6	~2.0	1156@0.5 C	510@0.5 C (1000 cycles)	976@2 C	[245]
S@HPC-graphene	Na_2CO_3 template	Micro/meso/ macropores	667	0.91	59	41.3	~1.2	1501@0.1 C	341@1 C (500 cycles)	-	[246]
S@HPC	$CaCO_3$ template	Micro/meso/ macropores	897	0.68	59	-	-	1475@0.1 C	874@0.1 C (50 cycles)	884@1 C	[247]
S@HPC	Colloidal SiO_2 template	Micro/meso/ macropores	220	0.76	75	67.5	~6.0	~1020@0.2 C	707@0.2 C	162@2 C	[182]
S@HPC	Organic aerogel + KOH	Micro/meso/ macropores	1260	1.54	66	52.8	0.6-1.0	1287@0.2 C	643@0.2 C (200 cycles)	~840@1 C	[248]
S@N, HPC-GO	$CaCO_3$ + GO	Micro/meso/ macropores	-	-	-	-	-	920@0.5 C	644@0.5 C (500 cycles)	634@5 C	[249]
S@HPC	MWCNTs + vertically aligned CNTs	Micro/meso/ macropores	-	-	63	54	6.3	995@0.05 C	700@0.05 C (150 cycles)	-	[250]
S@polymer-CNTs	Anodic aluminum oxide + CVD growth	Micro/meso/ macropores	-	-	63.5	63.5	1.9-2.5	990@0.5 C	647@1 C (450 cycles)	705@2 C	[85]
S@HPCs	Salt template ($CaCO_3$ + $Cu(Ac)_2$)	Meso/ macropores, ~4 nm and ~50 nm	961	0.84	38	26.6	1.52	1397@0.1 C	~838.2@0.1 C (100 cycles)	-	[152]
S@HPCs	Hard/soft templates (silica + polymer)	Meso/ macropores, 9 nm and 300 nm	850	1.4	50	35	-	1193@0.1 C	884@0.1 C (50 cycles)	458@2 C	[251]
S@HP graphene	Self-template (graphene oxide)	Meso/ macropores	434	-	66	-	-	824@1 C	~450@1 C (80 cycles)	543@10 C	[31]
S@N-HPC	Monolithic silica template	Meso/ macropores	350	1.7	~80	57.2	1.0	1450@0.02 C	~600@0.2 C (500 cycles)	~370@2 C	[71]
S@N-HPCs	Silica monolith template	Meso/ macropores	350	1.2	77	55.4	~2.0	1370@0.02 C	670@0.2 C (300 cycles)	-	[201]

TABLE 1 (Continued)

Materials	Preparation methods	Pore structures	SSA ($m^2\ g^{-1}$)	Pore volume ($cm^3\ g^{-1}$)	S content (%)	S content (electrode,%)	S loading (mg cm^{-2})	Initial discharge capacity (mAh g^{-1})[a]	Cyclingperformance (mAh g^{-1}) [a]	Rate performance (mAh g^{-1}) [a]	Reference
S@N-HCP-CNTs	$CaCO_3$ template	Meso/macropores	651	1.19	62.5	50	1.5	~800@0.5 C	~700@0.5 C (200 cycles)	400@2 C	[252]
S@O, N-HPC	Monolithic silica template	Meso/macropores	350–400	1.7-2.0	80–85	~60	3-4	810@0.2 C	~700@0.2 C (100 cycles)	-	[67]
S@3D-HPC	Silica hard template + P123 soft template	Meso/macropores	819	3.67	76.4	61.1	2.0	1042@0.2 C	703@0.2 C (100 cycles)	357@2.5 C	[253]
S@N,S-HPC	Silica template + $ZnCl_2$ activation	Meso/macropores	1420	4.94	78	54.8	~1.2	914@1 C	829@1 C (100 cycles)	581@8 C	[254]
S@N, Zn-HPC	Carbonization + $ZnCl_2$ activation	Meso/macropores	243	-	55.6	38.9	0.8-1.0	963@0.2 C	505@2 C (100 cycles)	528@5 C	[255]
S@N-HPC	SiO_2-monolith template	Meso/macropores	794	1.1	80	64	~6.0	1162@0.2 C	744@0.2 C (150 cycles)	-	[68]
S@ $Fe_{3-x}C$-HPC	Porous Fe_3O_4 hollow microsphere + CVD	Meso/macropores	197	-	75	60	1.2	1265@0.2 C	1089@0.2 C (100 cycles)	609@5 C	[87]

Abbreviations: CNF, carbon nanofibers; CNT, carbon nanotube; CTAB, hexadecyl trimethylammonium bromide; CVD, chemical vapor deposition; GO, graphene oxide; HPC, hierarchical porous carbon.

[a]1 C = 1675 mA g^{-1}.

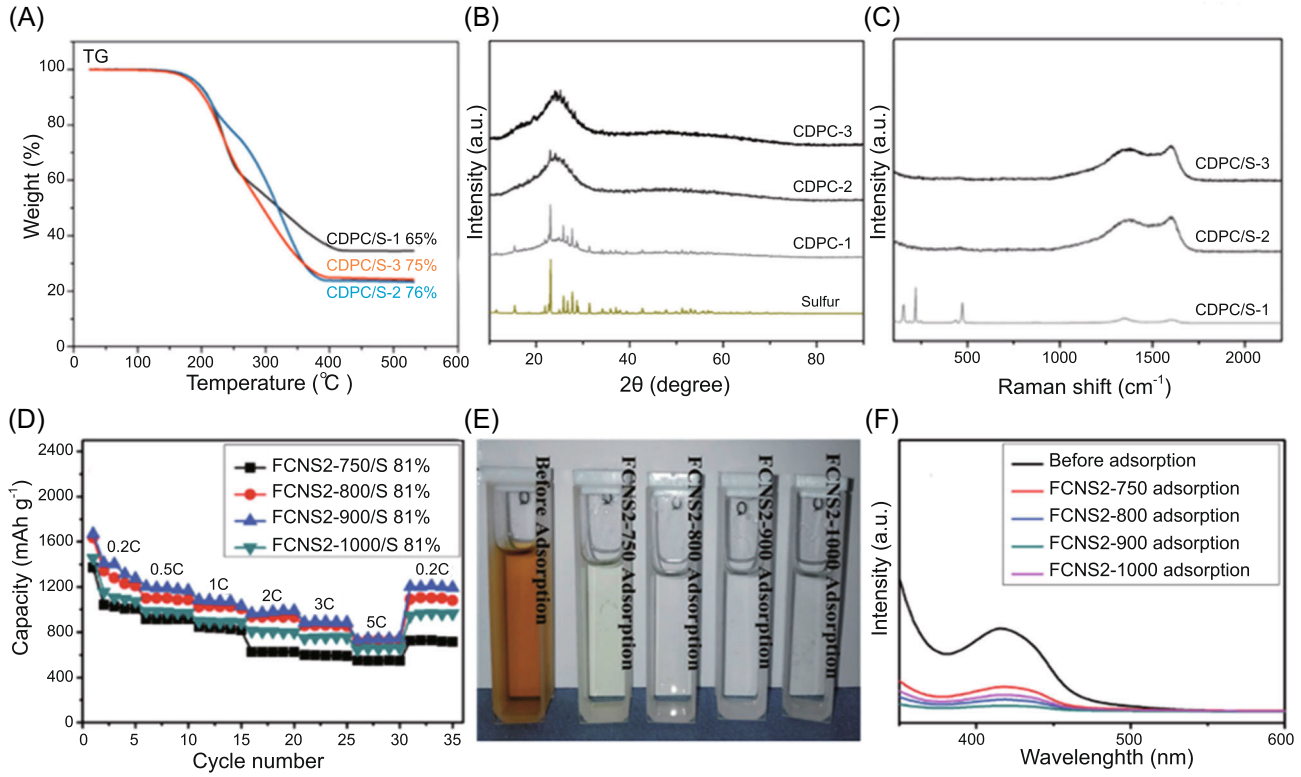

FIGURE 8 Effect of the pore volume of hierarchical porous carbons (HPCs) on the S/HPC cathodes when the sulfur content is higher than the theoretical maximum optimum value. (A-C) Thermogravimetric curves, X-ray diffraction patterns, and Raman spectra of coal-derived porous carbon (CDPC)/S composites, respectively. (D) Cyclic performance of flower-like carbon nanospheres (FCNS2-S81 wt% cathodes at 1 C after activation at 0.2 and 0.5 C. (E) Photograph and (F) UV–visible spectra of the Li_2S_6 solution exposed to as-obtained FCNSs. (A–C) Reproduced with permission: Copyright 2018, Elsevier.[188] (D–F) Reproduced with permission: Copyright 2017, Royal Society of Chemistry[69]

sulfur on the carbon surface. In contrast, there were no obvious characteristic peaks of sulfur for CDPC/S-2 and CDPC/S-3, demonstrating that sulfur was fully filled in the pores of HPCs. As expected, CDPC/S-3 showed the best electrochemical performance, while CDPC/S-1 delivered the lowest specific discharge capacities due to the lowest SSA and pore volume of CDPC-1. On comparison, CDPC-2 and CDPC-3 showed similar SSA ($>3000\,m^2\,g^{-1}$), but CDPC-3 had a much higher pore volume. Therefore, more free space could be retained for CDPC/S-3 to buffer the volume expansion and facilitate the mass transfer during the lithiation/delithiation, leading to the higher specific discharge capacity and better cyclic stability than CDPC/S-2.

Similar to the above work, Guo et al.[69] also pointed out that for HPCs with similar SSA, a higher pore volume would contribute to better battery performance. A series of hierarchical porous flower-like carbon nanospheres (FCNSs) were synthesized using urchin-like hierarchical silica spheres as templates. With an increase in the carbonization temperature from 750°C to 1000°C, the SSAs of FCNS2-750, FCNS2-800, FCNS2-900, and FCNS2-1000 (FCNS2-X, X being the carbonization temperature) were 1103, 1148, 1151, and $1080\,m^2\,g^{-1}$, respectively, and the total pore volumes correspondingly increased from 1.33 to 1.86, 1.94, and $1.74\,cm^3\,g^{-1}$, respectively. The FCNS2-900/S81% with a high sulfur content of 81 wt% delivered the highest discharge capacity and the best cyclic stability. A reversible capacity of $1104\,mAh\,g^{-1}$ was achieved for FCNS2-900/S81% at 1 C after two-cycle activation at 0.2 and 0.5 C. After 200 cycles, a capacity of $923\,mAh\,g^{-1}$ and high-capacity retention of ~85% could be achieved at 1 C. In contrast, other cathodes with smaller pore volume showed worse cyclic performances (Figure 8D). The performances increased in the order of FCNS2-750/S81% < FCNS2-1000/S81% < FCNS2-800/S81% < FCNS2-900/S81%, which was consistent with the increase in their pore volumes. To further explain the differences in the electrochemical reversibility, the adsorption of PSs by the as-synthesized HPCs was detected by exposing the samples to the Li_2S_6 solution and then confirmed by ultraviolet-visible (UV-vis) spectroscopy. The photograph and UV–vis spectra (Figure 8E,F) demonstrated the following order of adsorption capacity with PSs for HPCs: FCNS2-750 < FCNS2-1000 < FCNS2-800 < FCNS2-900, matching well with the cyclic durability.

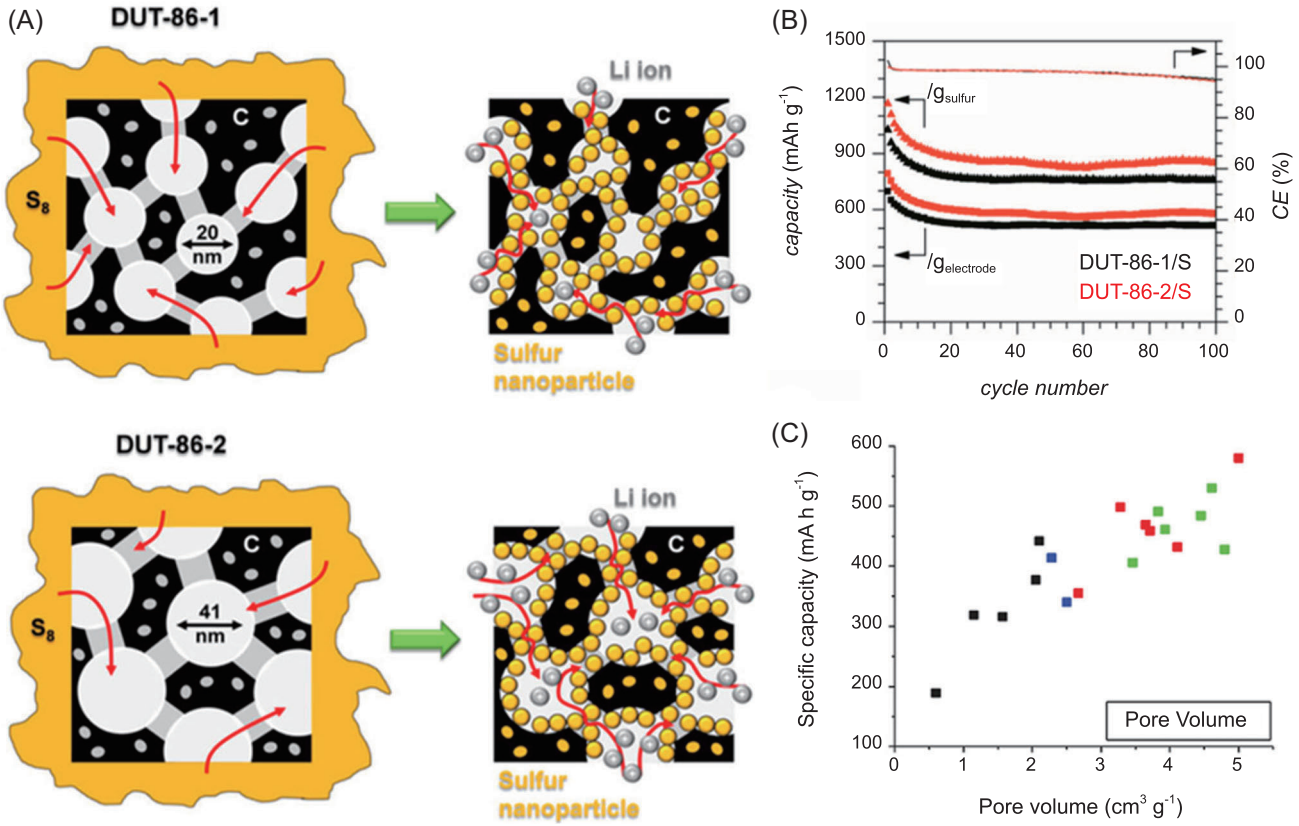

FIGURE 9 Effect of the pore volume of hierarchical porous carbons (HPCs) on the performances of S/HPCs cathodes when sulfur loading is lower than that for the desired optimum content of sulfur fully confined in the pores. (A) Schematic representation of S@HPCs nanocomposites before and after melt infiltration of hydrophobic sulfur. (B) Achievable capacity, cycling stability, and Coulombic efficiency (CE) of the DUT-86/S composites at 0.1 C. (C) Scatter plots correlating the discharge capacity obtained at the 100th cycle with pore volume. (A,B) Reproduced with permission: Copyright 2014, American Chemical Society.[160] (C) Reproduced with permission: Copyright 2016, Wiley[157]

In view of volume expansion (80 vol%) for the sulfur cathode during operation, the sulfur contents in the above two studies exceeded the optimal values of HPCs. To understand the case where the pore volume of the HPCs is higher than its theoretical value required for sulfur loading, Hoffmann et al.[160] demonstrated an example of micro/mesoporous carbon hosts (Figure 9A). In their research, two carbide-derived carbons were synthesized with a nanocasting approach using silica nanospheres as templates, followed by chlorine treatments. The obtained DUT-86-1 and DUT-86-2 had similar microporous structures, with a high SSA of ~2400 $m^2 g^{-1}$ and a specific micropore volume of ~0.53 $cm^3 g^{-1}$, but different mesoporous structures, with mesopores of 22.4 nm for DUT-86-1 and 38 nm for DUT-86-2, and different pore volumes of 3.66 $cm^3 g^{-1}$ for DUT-86-1 and 4.97 $cm^3 g^{-1}$ for DUT-86-2. A DUT-86/S composite with a high sulfur content of 80 wt%, which is still lower than the theoretical maximum values (81% for DUT-86-1% and 85% for DUT-86-2), was synthesized. According to the cyclic stability (Figure 9B), although the DUT-86-2/S cathode showed slightly higher capacity than DUT-86-1/S cathode, both these cathodes delivered good capacity retention of 74% over 100 cycles at a low rate of 0.1 C because both DUT-86-1/S and DUT-86-2/S had extra space for the mass transfer after sulfur filling (Figure 9A). However, very high pore volume and porosity of HPCs could influence the contact between sulfur and carbon skeletons, further resulting in unsatisfactory electrical conductivity. Therefore, when the pore volume of HPCs is lower than that for the desired optimum content of sulfur, the higher the PV, the better the performance of S/HPCs.[69,162,188,191,221] When the pore volume is much higher than an optimal volume for that sulfur content, further increase in pore volume may not have a positive effect on the performance of Li–S cells (Figure 9C).[135,157,160]

3.2 | The effect of SSA for HPCs on the performance of S/HPC cathodes

The SSA of hierarchical porous materials, which is highly related to the ratio of small mesopores and micropores, is

of great significance in many chemical reaction systems as a higher SSA can provide more active sites, and this rule is also applicable to the conversion reaction systems of Li–S batteries. Two types of HPCs, $PSSO_3H$-Spiro40_C, and $PSSO_3H$-Spiro50_C with the same pore volume of 1.16 $cm^3 g^{-1}$, were produced through twin polymerization on sulfonated polystyrene microparticles.[57] However, the micropore volume of $PSSO_3H$-Spiro40_C (29.7%) is higher than that of $PSSO_3H$-Spiro50_C (23.6%), thus leading to a slightly higher SSA for $PSSO_3H$-Spiro40_C (1389 $m^2 g^{-1}$) than that for $PSSO_3H$-Spiro50 (1262 $m^2 g^{-1}$). After infiltration of ~67 wt% sulfur into the pores of $PSSO_3H$-Spiro, although 4% of free pore volume was left for both $PSSO_3H$-Spiro40_C/S and $PSSO_3H$-Spiro50_C/S, the SSA of $PSSO_3H$-Spiro40_C/S would be higher if sulfur is uniformly distributed in the pore. Therefore, more reactive sites of $PSSO_3H$-Spiro40_C/S could be retained for the full chemical conversion between sulfur and lithium sulfide. As can be seen from the cyclic voltammetry (CV) analysis (Figure 10A,B), there were two cathodic peaks at around 2.4 and 2.0 V, corresponding to the reduction of sulfur to high-order Li_2S_n ($n > 4$) and then to low-order Li_2S_n ($1 \leq n < 4$), respectively, while the oxidation peak at ~2.5 V was representative for the oxidization of low-order Li_2S_n to high-order Li_2S_n and finally elemental sulfur. In addition, the relatively narrow peaks for the $PSSO_3H$-Spiro40_C/S electrode indicated fast kinetics of reduction and oxidation reactions. The CV curves of the subsequent cycles matched well with the first one, indicating the better reversibility of $PSSO_3H$-Spiro40_C/S than other cathodes. As a result, the $PSSO_3H$-Spiro40_C/S delivered higher capacity retention and better rate performances than $PSSO_3H$-Spiro50_C/S (Figure 10C).

However, Sahore et al.[157] pointed out that to achieve high sulfur utilization at a high sulfur content, pore volume becomes more important than SSA when the sulfur content is higher than the maximum value for HPCs. On the basis of their results, for HPCs-S composites with a high sulfur content of up to 80 wt%, the HPCs with the

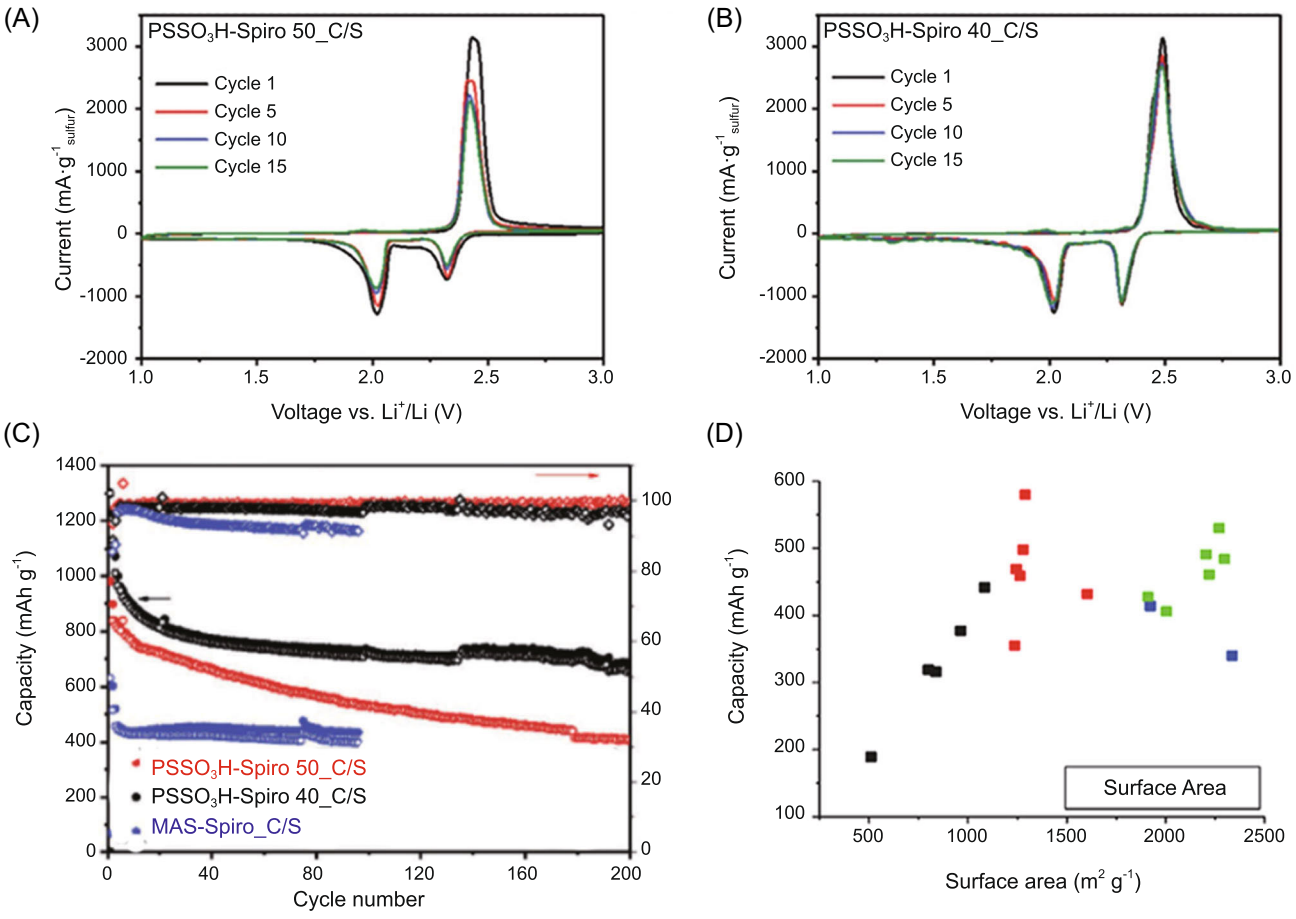

FIGURE 10 Electrochemical analyses of hierarchical porous carbon (HPC)/S cathodes with different specific surface areas (SSAs) but the same pore volume. (A,B) Cyclic voltammetry curves at 0.1 mV s^{-1} for $PSSO_3H$-Spiro50_C/S and $PSSO_3H$-Spiro40_C/S, respectively. (C) Cyclic stability analysis for HPC/S cathodes. (D) Scatter plots correlating discharge capacity obtained at the 100th cycle with SSA. (A–C) Reproduced with permission: Copyright 2018, Wiley.[57] (D) Reproduced with permission: Copyright 2016, Wiley[157]

low SSA and pore volume showed low capacities, while the HPCs with both high SSA and high pore volume resulted in higher capacities, as expected. Interestingly, the HPCs with a moderate SSA but a high pore volume also contributed to the high capacities. In contrast, the HPCs with a moderate pore volume and a high SSA led to moderate capacities. According to their findings (Figure 10D), if the SSA of HPCs was lower than 1500 $m^2 g^{-1}$, the discharge capacity increased with an increase of the SSA; when the SSA exceeded 1500 $m^2 g^{-1}$, however, no obvious correlation was observed between the discharge capacity and SSA.

3.3 | Relationship between the positional order of pores and performance of S/HPC cathodes

Besides the pore volume and SSA, the positional order of pore structures in HPCs also plays a significant role in the physical confinement of PS ions in Li–S cells. As shown in Figure 11A, Choi et al.[237] designed an HPC structure in which the meso/macropores are surrounded by the outer micropores using an ultrasonic spray pyrolysis method for hosting sulfur. The inner meso/macropores can accommodate most sulfur and serve as microsized reactors for active materials, and the outer micropores can function as a protection layer. During charging and discharging, the micropores positioned in the outer shell and in the walls between the core meso-/macropores could effectively inhibit the migration of the soluble high-ordered PSs into electrolytes. The HPC/S showed a high discharge capacity of 1412 at 100 mA g^{-1} and excellent capacity retention of 77% after 500 cycles at ~4 A g^{-1} due to the special hierarchical porous structure. In contrast, the random micropores and mesopores in conventional activated carbon (AC1600) showed undesirable confinement ability with PS (Figure 11B) and led to a lower capacity of 64% for AC1600-S. Consistent with the aforementioned work, Chen et al.[60] compared three kinds of S@hollow carbon nanosphere cluster (S@HCNC) electrodes (Figure 11C–F) and also concluded that the microporous sheath could inhibit the PS shuttle and improve the electrochemical performances (Figure 11G) of Li–S batteries, although the HCNCs with a microporous layer had lower pore volume and SSA compared to monodispersed hollow carbon nanospheres (MHCSs).

In contrast to the above research, a quad-modal nested porous carbon was designed as the sulfur host (Figure 11H) with pore sizes increasing in an orderly manner from the inside to the outside of the pore walls.[61] On the basis of their findings, the first-modal pores (>50 nm) can only facilitate Li^+ transfer, while the second-modal pores (20–50 nm) are beneficial to Li^+ transfer, encapsulation of sulfur, and inhibition of PSs. The third-modal pores (7–20 nm) are favorable for transport of Li^+ and interconnecting mesopores and micropores, and the fourth-modal pores (<3 nm) can accommodate sulfur and PSs. Therefore, the ordered HPCs with a high SSA of 915 $m^2 g^{-1}$, a high pore volume of 4.15 $cm^3 g^{-1}$, and a capillary force endowed the S@HPCs cathode (with a high sulfur content of 78%) with both desirable discharge capacity (Figure 11I) and cyclic stability (914 mAh g^{-1} after 200 cycles at 3 C). According to the summary presented in Table 2, the ordered HPC with high SSA, high pore volume, and strong capillary force is well designed to achieve both excellent rate performance and long lifespan of Li–S cells.

3.4 | Effect of heteroatom doping on the performances of S@HPCs

Due to the inherent nonpolarity of HPCs, they can only provide physical confinement to polar PS species through pore structures. To further reduce the PS migration, researchers have paid attention to heteroatom-doped HPCs, which show stronger chemical interaction with PSs than the undoped ones. Various heteroatom-doped HPCs have shown promise in the use of Li–S cells, such as nitrogen-doped HPCs (N-HPCs), oxygen-doped HPCs (O-HPCs), nitrogen, sulfur-co-doped HPCs (N, S-HPCs), nitrogen, oxygen co-doped HPCs (N, O-HPCs), nitrogen, phosphorus co-doped HPCs (N, P-HPCs), nitrogen, iodine-co-doped HPCs (N, I-HPCs), and nitrogen, sulfur, and oxygen tri-doped HPCs (N, S, O-HPCs).

On the basis of the summary presented in Table 1, nitrogen is the most widely utilized dopant to functionalize HPCs as it is a nonmetal element adjacent to a carbon atom and the nitrogen doping can effectively reduce the structural defects of carbon materials caused by lattice mismatch.[256] At the same time, the lone pair of electrons of the nitrogen atom can change the electronic distribution of the material, resulting in higher chemical polarity and adsorption toward PSs. By utilizing different carbon precursors, hierarchical macro/mesoporous inverse opal (IOP) carbon (using resol-formaldehyde) and nitrogen-doped hierarchical macro/mesoporous inverse opal (N-IOP) carbon (using cyanamide + resol-formaldehyde) were obtained and used as sulfur hosts.[68] Although N-IOP has a much lower SSA (794 $m^2 g^{-1}$) and pore volume (1.1 $cm^3 g^{-1}$) than IOP (1006 $m^2 g^{-1}$ for SSA, 2.2 $cm^3 g^{-1}$ for pore volume), N-IOP showed better adsorption ability toward PSs (Figure 12A) due to the strong interaction between pyrrolic-type nitrogen and

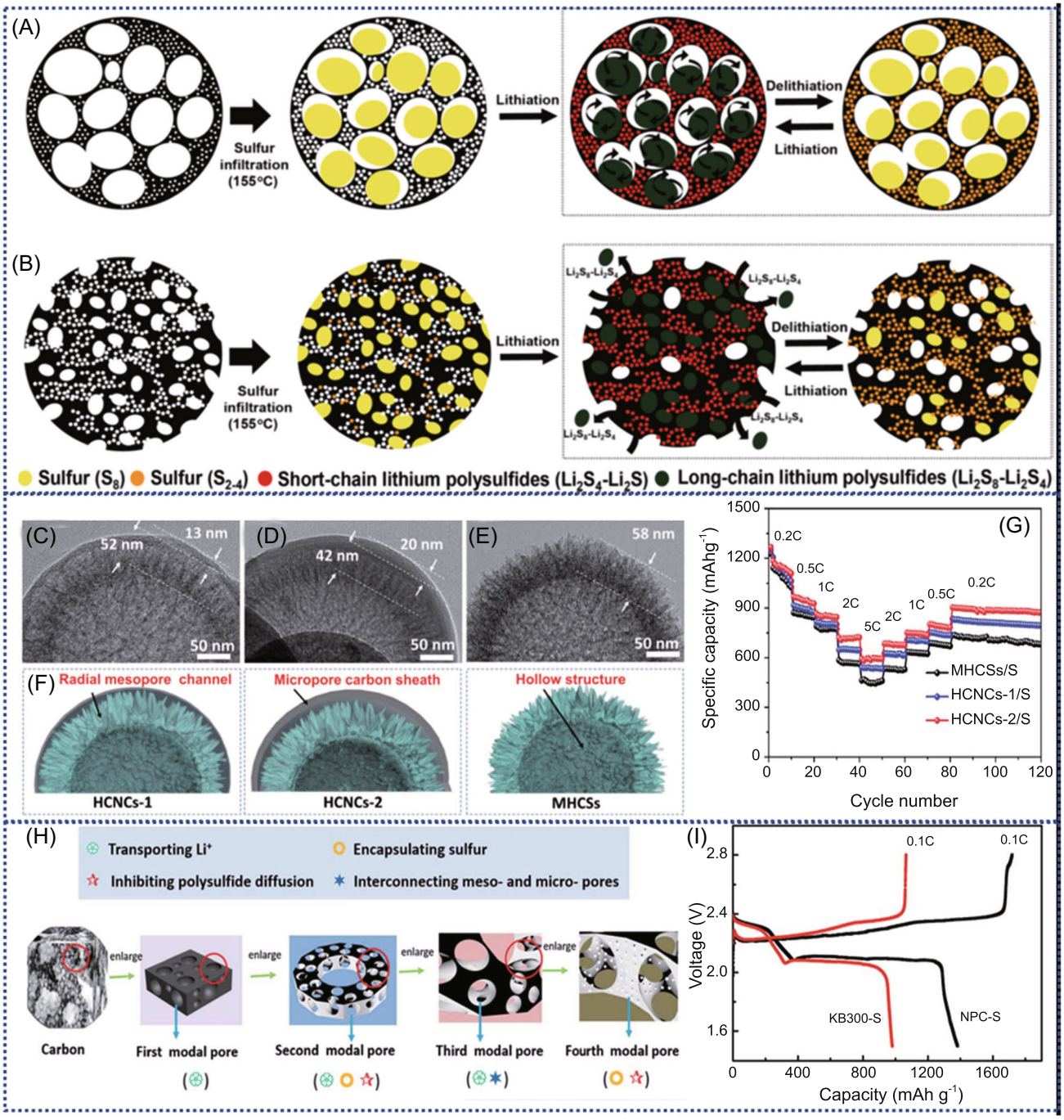

FIGURE 11 Correlation between the order degree of pores for hierarchical porous carbons (HPCs) and performance of S/HPCs cathodes. (A) HPC particles have micropores in the outer shell, surrounding the inner meso/macropores. (B) AC1600 containing micropores and mesopores in a random geometry. (C-E) Transmission electron microscopy images that show the pore characteristics of hollow carbon nanosphere clusters (HCNCs-1 and HCNCs-2) and monodispersed hollow carbon nanospheres (MHCSs), respectively. (F) Sectional pore structure schematic illustration of HCNCs and MHCSs. (G) Rate performance of MHCSs/S, HCNCs-1/S, and HCNCs-2/S. (H) Schematic diagram for the preparation of the nested pore structure carbon and the functions of each modal pore in Li–S cells. (I) Charge and discharge curves of nested porous carbon–sulfur (NPC–S) and carbon black 300–sulfur (KB300–S) composite electrodes at 0.1 C. (A–B) Reproduced with permission: Copyright 2014, American Chemical Society.[237] (C–G) Reproduced with permission: Copyright 2019, Royal Society of Chemistry.[60] (H,I) Reproduced with permission: Copyright 2016, Royal Society of Chemistry[61]

TABLE 2 Correlation between the pore structures of hierarchical porous carbons (HPCs) and their properties for lithium–sulfur (Li–S) cell

	Physical properties			Properties of Li–S cells		
Pore structures of HPCs	**Surface area**	**Pore volume**	**Capillary force**	**Li-ion transfer**	**C-rate capability**	**Cyclic stability**
Micropores	★★★	★☆☆	★★★	★☆☆	★☆☆	★★★
Mesopores	★★☆	★★☆	★★☆	★★☆	★★☆	★★☆
Macropores	★☆☆	★★★	★☆☆	★★★	★★☆	★☆☆
Disordered hierarchical pores	★★☆	★★☆	★★☆	★★☆	★★☆	★★☆
Ordered hierarchical pores	★★★	★★★	★★★	★★★	★★★	★★★

Note: One solid star indicates low contribution to the properties, while three solid stars indicate high contribution. Reproduced with permission: Copyright 2016, Royal Society of Chemistry.[61]

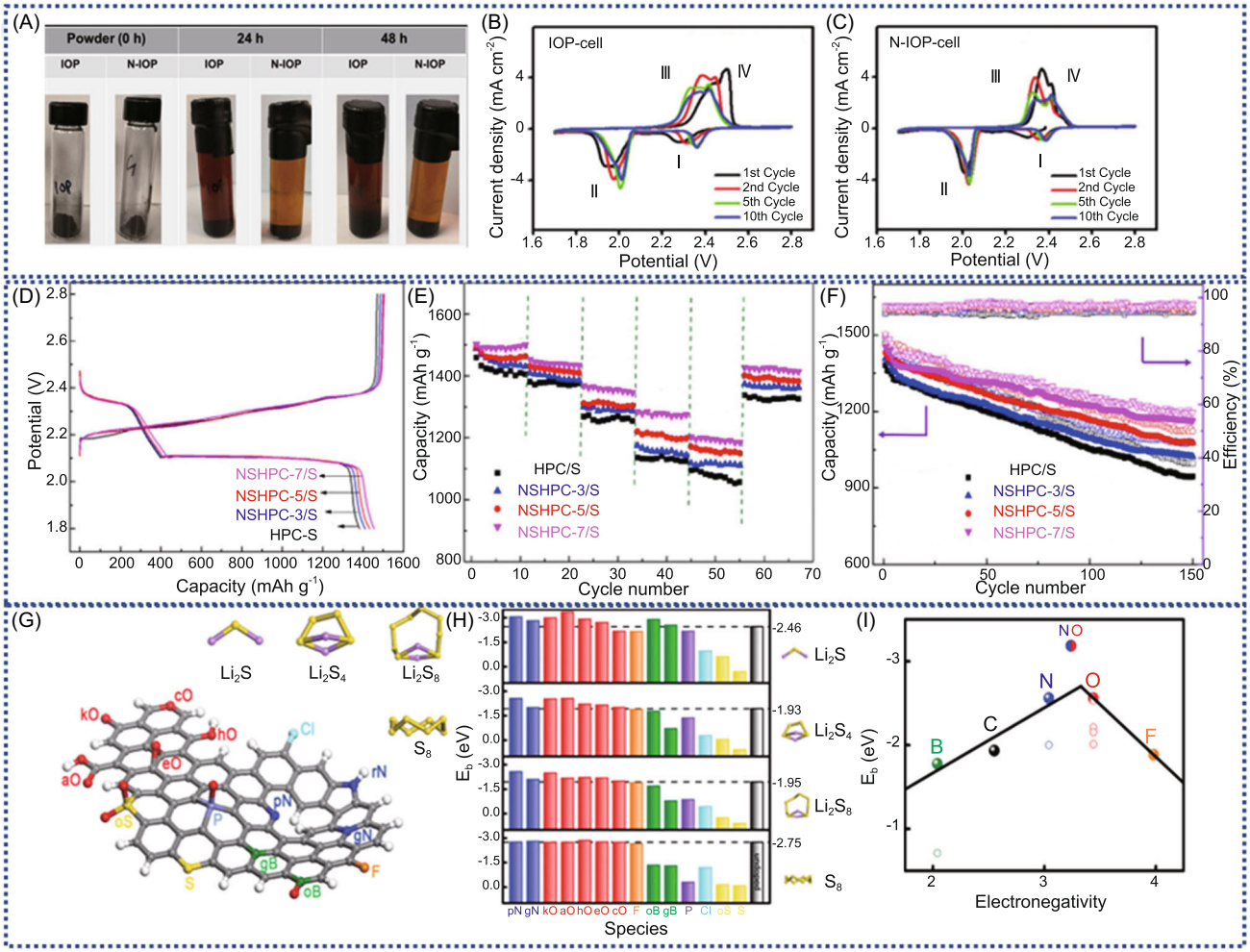

FIGURE 12 Correlation between heteroatom doping of hierarchical porous carbons (HPCs) and the performance of S@HPCs cathodes. (A) Polysulfide trapping test of inverse opal (IOP) carbons compared to N-IOP carbons as a function of time. (B,C) Cyclic voltammetry curves of the IOP cell and the N-IOP cell. (D) Initial charge/discharge profiles at 0.1 C, (E) rate performance, and (F) cycling performances at 0.1 C for HPC/S and N, S-HPC-X/S. (G) Schematic diagram of X-doped nanocarbon materials (X = N, O, F, B, P, S, Cl) and the Perdew–Burke–Ernzerh level optimized structure of Li_2S, Li_2S_4, Li_2S_8, and S_8 molecules. (H) Binding energy E_b (eV) of Li_2S, Li_2S_4, Li_2S_8, and S_8 interacting with X-doped graphene nanoribbons (GNRs) with a zigzag edge, in comparison with the binding energy of Li_2S, Li_2S_4, Li_2S_8, and S_8 interacting with undoped GNR shown as gray bars and dashed lines. (I) E_b with Li_2S_4 versus electronegativity of dopant elements of GNRs. (A–C) Reproduced with permission: Copyright 2019, Wiley.[68] (D–E) Reproduced with permission: Copyright 2017, Wiley.[179] (G–I) Reproduced with permission: Copyright 2016, Wiley[33]

Li_2S_6. Besides, in comparison to the IOP cell, the cyclic voltammetry (CV) profile of the N-IOP cell demonstrated lower polarization with cathodic and anodic peaks, further confirming that nitrogen doping was effective at binding and reactivating the active materials for redox activity (Figure 12B,C). As a result, the N-IOP cell showed good reversibility during the conversion reaction and redistribution of sulfur species. At 0.2 C, the N-IOP cell maintained a capacity retention of 66% after 150 cycles with an ultrahigh sulfur loading of 6.0 mg cm^{-2}, much more stable than the IOP cells (39%).

Aside from nitrogen doping, a series of nitrogen/sulfur-codoped HPCs (NSHPCs-X, X is the ratio of thiourea to the as-prepared HPC during synthesis) with similar pore structures but different sulfur and nitrogen contents were applied in Li–S cells.[179] The nitrogen contents of HPC, NSHPC-3, NSHPC-5, and NSHPC-7 were 0, 3.94, 5.23, and 6.42 at%, respectively, and the sulfur contents in HPC, NSHPC-3, NSHPC-5, and NSHPC-7 were 0, 1.87, 2.23, and 2.52 at%, respectively. With the increase of nitrogen and sulfur contents in the NSHPCs skeleton, NSHPC-7 showed more active sites and stronger chemisorption toward PSs than other samples, leading to higher sulfur utilization and discharge capacity (Figure 12D). Accordingly, both the cyclic stabilities (Figure 12E) and rate capacities (Figure 12F) of the cathodes followed the order: NSHPC-7/S > NSHPC-5/S > NSHPC-3/S > HPC/S.

To guide future screening and rational design of carbonaceous scaffolds with chemical dopants for Li–S batteries, a series of heteroatom-doped (B, N, O, F, P, S, and Cl) graphene nanoribbon structures were simulated (Figure 12G), and their binding energies with sulfur species (Figure 12H) and electronegativity (Figure 12I) were evaluated using density functional theory (DFT) calculation.[33] According to their analyses of configurations, binding energies, bond lengths, and charge transfer of different heteroatom-doped carbons, the rational design principles of heteroatom-doped carbon were concluded to be as follows: (1) the dopants should possess lone pairs of electrons as electron-rich donors, higher binding energy with sulfur species via the dipole–dipole electrostatic interaction, and higher electronegativity and smaller atomic radius that matches Li compared with carbon atoms, and (2) the introduced heteroatoms should form delocalized π bonds with the conjugated system and stable bond structures with the carbon skeleton. To fulfill these conditions, doping of N or O heteroatoms with an extra pair of electrons and high binding energies with sulfur species, or even co-doping is more favorable to facilitate better anchoring ability than that of other heteroatoms (B, F, S, P, and Cl), which are expected to achieve an enhancement in the reversible capacity and CE.

According to the above explanations, all of the parameters for HPCs including pore volume, SSA, heteroatom doping, and order degree influence the performance of the S@HPC cathode. To gain desirable HPCs that simultaneously have large pore volume, high SSA, ordered pores, and suitable dopants, the templating/activation method with heteroatom-rich carbon precursors may be an efficient approach. Additionally, the introduction of some polar compounds (e.g., metals, oxides, sulfides, nitrides, and carbide particles) into HPCs can further promote the chemisorption and conversion of PSs, which could accelerate the commercialization for Li–S cells Figure 13.

4 | HPC-FUNCTIONALIZED SEPARATORS OR INTERLAYERS FOR LI–S CELLS

Separators, which function as an insulator between the anode and the cathode and as a medium for ion transport, are a key component of Li–S cells and play a significant role in battery operation. In addition to the development of sulfur cathodes with HPCs, the engineering of separators or inset of interlayers between the cathodes and separators provides another effective approach to suppress PS migration.[258]

In the case of commercial polyolefin separators, the pores are too large (1–100 nm by the wet method, 100–300 nm by the dry method) to prohibit the migration of PS ions.[259] To design separators that can effectively block PSs, but without influencing the diffusion of Li ions, it is important to understand the dimensions of Li^+ and PS ions. The radius of Li^+ is 0.076 nm, much smaller than the pores of polyolefin membranes, while the dimensions of PS ions are different from those in solvated phases. The understanding behind how the soluble Li_2S_n ($4 \le n \le 8$) intrinsically interacts with the solvent is not clear from the earlier studies and needs to be explored more. For the most widely used solvent of the mixture of 1,3-dioxolane/1,2-dimethoxyethane (DOL/DME, 1:1 by volume) for a Li–S cell electrolyte, only the lateral size and radius of the solvated PS ions in this system were calculated through first-principle simulation. As shown in Figure 12, Li_2S_8 has the largest solvated radius (7.21 Å), followed by Li_2S_6 (6.60 Å) and Li_2S_4 (5.74 Å), while the lateral size increases in an inverse trend from 12.20 Å of Li_2S_8 to 13.40 Å of Li_2S_6 and 13.60 Å of Li_2S_4 due to the lowest solubility of Li_2S_4 in DOL/DME solvent.[257]

Considering the bond lengths of Li–S and S–S, the longest Li_2S_n is smaller than 1.5 nm. Therefore, the introduction of a micro/small mesoporous carbon layer between the polyolefin membrane and the sulfur cathode

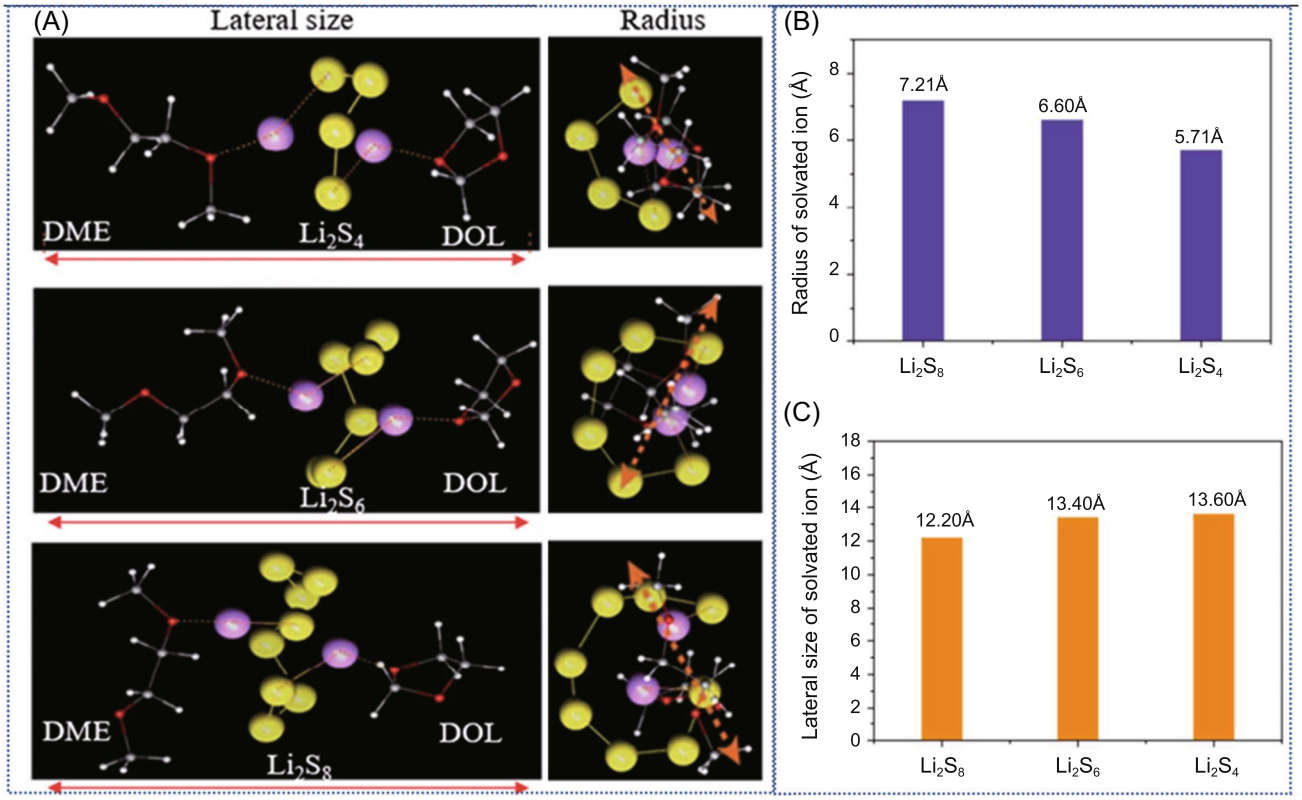

FIGURE 13 First-principle simulation of the interaction between soluble Li_2S_n and the solvent of an electrolyte. (A) Energy-optimized molecular structures of Li_2S_4, Li_2S_6, and Li_2S_8 monomer units in the mixture of DOL and DME based on the first-principle molecular dynamics (MD) simulation. (B) Radius of gyration and (C) lateral size of Li_2S_4, Li_2S_6, and Li_2S_8 in DOL and DME calculated by MD simulations. Reproduced with permission: Copyright 2017, American Chemical Society.[257] DME, 1,2-dimethoxyethane; DOL, 1,3-dioxolane

is expected to effectively confine the PSs. Furthermore, the carbon layer can serve as an additional current collector and an interfacial reactor, enhancing the transport for both Li^+ and electrons and conversion kinetics in the Li–S system. The use of coatings on separators and the addition of the interlayer function also enhance the battery performance. However, Jeong et al.[20] reported that there are still some differences between the coatings on separators and adding interlayers according to the configuration of whether they physically contact the original separators or not. On the basis of the definition given by them, the interlayer is an inserted self-support film in between the existing separator and the electrode, while the coating of the membrane has strong contact with the separators. The recent progress made on HPC-functionalized separators and HPC-derived interlayers for high-performance Li–S batteries is summarized in Table 3.

4.1 | HPC-coated separators for Li–S batteries

Crab shell-derived nitrogen-doped micro–mesoporous carbon was used as a functional layer to a modified PP separator using a simple blade coating method with a polyvinylidene fluoride binder.[132] The functionalized PP showed a macroscopically smooth surface, but a microscopically rough surface (Figure 14A). The coating layer had a thickness of 4 μm (Figure 14B) and a mass loading of 0.2 mg cm^{-2}, much thinner and lighter than that of commercial PP (~25 μm, ~1.1 mg cm^{-2}), which are favorable for maintaining the high energy density of Li–S devices. In addition, the wettability of PP toward the electrolyte was enhanced obviously from the contact angle analysis (Figure 14C) because of the micro/mesoporous structure that can facilitate the penetration of electrolyte. The ion conductivity (σ) of separators can be calculated according to the formula:

$$\sigma = \frac{d}{A \cdot R_b}, \tag{3}$$

where d is the thickness of the separator, A is the active area of the electrode, and R_b is the bulk resistance. Although the ion conductivity is directly proportional to the thickness of the separator, increasing the thickness can also increase the transport paths of ions. Thus,

TABLE 3 A summary of the characteristics and performance of HPC-coated separators and HPC-based interlayers used in Li–S batteries

Separators/ interlayers	Cathode	Methods	Pore size	SSA ($m^2 g^{-1}$)	Pore volume ($cm^3 g^{-1}$)	Mass loading ($mg cm^{-2}$), thickness (μm) of coatings	S content (wt%)	S loading ($mg cm^{-2}$)	Initial discharge capacity ($mAh g^{-1}$) [a]	Cycling performance ($mAh g^{-1}$) [a]	Rate performance ($mAh g^{-1}$) [a]	Reference
HPC-coated PP	Pure sulfur	Zinc nitrite template	Micro/meso-	1538	3.56	0.35, 25	80	1.2	1427@0.2 C	920@0.2 C (100 cycles)	-	[84]
N–HPC-coated PP	S@N-HPC	Citric acid + urea self-template	Micro/meso-	301	1.76	0.6, 10	56	~1.6	1525@0.5 C	1129@0.5 C (100 cycles)	430@10 C	[260]
N–-HPC-coated PP	Pure sulfur	Crab shell + KOH activation	Micro/meso-	1298	2.10	0.2, 4	63	1.5–2.0	1301@0.1 C	971.3@0.1 C	642.2@2 C	[132]
HPC-coated PP	Pure sulfur	Corncob + KOH	Micro/meso-	2645	1.54	1.7, 29	70	1.7–1.9	1067@0.5 C	648@0.5 C (350 cycles)	-	[183]
N–HPC-coated PP	S@N-HPC	MgO template	Micro/meso/ macro-	-	-	0.3, 10	60	0.8	1370@0.6 C	1058@0.6 C (100 cycles)	539@12 C	[81]
N–HP–graphene-coated PP	S@Graphene	Urea template	Meso/macro-	1022.3	0.92	0.71, 32–43	60	~2.7	1150@0.2 C	852@0.2 C (200 cycles)	~150@2 C	[146]
N, Co–HPC-coated PP	S@CNTs	$Co(AC)_2$ + silica template	Meso/macro-	637	2.62	0.3, 50	56	1.2	890@2 C	~500@2 C (300 cycles)	-	[62]
HPC-coated glass fiber	Pure sulfur	Oak Tree fruit shells + KOH	Micro/meso/ macro-	796	0.38	-. -	70	0.8–1.1	1321@0.2 C	990.8@0.2 C (50 cycles)	362@1.5 C	[189]
N,S–HPC-coated PP	Pure sulfur	Lotus plumule + KOH	Micro/meso-	2453.8	2.14	-, 42	80	~1.8	1549@0.1 C	609@0.5 C (300 cycles)	515@1 C	[197]
HPC interlayer	Pure sulfur	Carbonization of PVP + CO_2	Micro/meso-	459	0.32	4.0–4.4, -	60	~1.4	1549@0.2 C	1286@0.2 C (100 cycles)	-	[153]
N–HP graphene interlayer	S@N-HP graphene	Ice template	Micro/meso-	830	1.6	-, -	41.3	0.9–1.2	1548@0.5 C	946@0.5 C (100 cycles)	822@2 C	[261]
HPC interlayer	Pure sulfur	Pyrolysis of cotton cloth	Micro/meso	166.3	-	-, -	60	1.0	1112@0.2 C	743@0.2 C (200 cycles)	718@2 C	[128]
HPC interlayer	Pure sulfur	Carbonization of leaves	Micro/meso-	390	0.34	-, -	70	1.3	1320@0.1 C	1013@0.1 C (100 cycles)	829@0.5 C	[121]

TABLE 3 (Continued)

Separators/ interlayers	Cathode	Methods	Pore size	SSA ($m^2 g^{-1}$)	Pore volume ($cm^3 g^{-1}$)	Mass loading ($mg cm^{-2}$), thickness (μm) of coatings	S content (wt%)	S loading ($mg cm^{-2}$)	Initial discharge capacity ($mAh g^{-1}$) [a]	Cycling performance ($mAh g^{-1}$) [a]	Rate performance ($mAh g^{-1}$) [a]	Reference
HPC interlayer	Pure sulfur	Pyrolysis of PAA + steam activation	Micro/meso-	995	0.51	1.0, -	70	~2.5	1224@0.1 C	897.2@0.1 C (100 cycles)	416@2 C	[164]
HPC interlayer	Pure sulfur	Carbonization of cassava	Micro/meso/ macro-	13.8	6.37	7–10, 200	60	~1.6	1308@0.5 C	811@0.5 C	640@4 C	[123]
HPC interlayer	S@HPC	Carbonization of bacterial cellulose	Micro/meso/ macro-	375	5.29	1.2–1.6, -	81	5.1–6.8	1134@0.16 C	800@0.16 C (150 cycles)	475@1.6 C	[135]
N, P–HPC interlayer	S@N, P-HPC	Pyrolysis of silk cocoons + H_3PO_4	Micro/meso/ macro-	779.2	0.71	-. -	49	-	1412.6@0.1 C	888.5@0.1 C (100 cycles)	758.1@2 C	[205]
HPC-coated PP	Pure sulfur	Carbonization of filamentous fungi	Meso/macro-	20	-	-, -	60	-	~1000@0.5 C	650@0.5 C (100 cycles)	620@2 C	[32]

Abbreviations: CNT, carbon nanotube; HPC, hierarchical porous carbon; PAA, poly(acrylic acid); PP, polypropylene; PVP, polyvinylpyrrolidone.

[a] $1 C = 1675 mA g^{-1}$.

controlling the thickness of coating layers is also significant for Li^+ migration. Due to the enhanced electrical conductivity and compatibility between the electrodes, the separator, and the electrolyte, the Li-S cell assembled with carbon-coated PP showed a much higher rate performance (642 mAh g^{-1}@2 C) than that of the pristine one (~410 mAh g^{-1}@2 C) with the same sulfur content of 63 wt%. Besides, owing to the synergetic physical confinement from hierarchical pores and chemical adsorption from nitrogen doping, the PS shuttle was highly suppressed and the discharge capacity was increased from 508 to 829.7 mAh g^{-1} at 0.5 C after 100 cycles (Figure 14D).[132] Upon further increasing the sulfur content from 63 to 77 wt%, the cells showed a high sulfur utilization rate and reversible capacity of 578 mAh g^{-1} after 500 cycles at 1 C, with capacity retention of ~85% of the initial capacity. To reveal the function of HPC coating layers, the cycled cells were disassembled for microscopy characterization. According to the SEM image (Figure 14E) and energy-dispersive spectroscopy mapping (Figure 14F) of the coating layer, the cathode region showed lots of whitish dots that corresponded to the PSs/disulfides and sulfides, indicating that the migrating active PS species were effectively absorbed and captured during the discharge and charge by the HPC coating.[132]

Besides the polyolefin separators, HPCs can also be used to modify the glass fiber separators using a similar blade coating method to that used by Selvan et al.[189] As the coating layers could serve as second current collectors, the HPC-functionalized glass fiber separators showed lower resistance compared to the pristine one (Figure 14G), leading to accelerated charge transfer and ion diffusion, and enhanced electrochemical performances. More interestingly, they investigated the function of KOH activation of HPCs. It was found that the cells assembled with the activated carbon-coated glass fiber (ACGF) showed better cyclic stability than those used the nonactivated carbon-coated glass fiber (NCGF) because the KOH activation introduced large amounts of micropores and induced high adsorption toward PSs. Nevertheless, these two types of cells showed similar rate performances (Figure 14H), especially at high current densities. At 0.2, 0.25, 1, and 1.5 C, the discharge capacities were 898, 591, 428, and 340 mAh g^{-1} for NCGF cells and 906, 674, 493, and 362 mAh g^{-1} for ACGF cells, respectively. These results are consistent with the findings of Liu et al.;[159] that is, the micropores of HPC can enable better cycle stability on account of solvent-restricted lithiation/delithiation of sulfur, while they do not contribute much to the rate performance due to the lengthening of pathways for lithium-ion transmission.

4.2 | HPC-based interlayers for Li–S batteries

As the porous carbon coating layers may crack and detach from the polyolefin separators during long-term battery operation due to the poor interfacial adhesion between carbon and inert polyolefin separators, some researchers put forward new configurations of Li–S cells, namely, the insertion of carbon interlayers between the cathodes and separators. The interlayers are usually thicker and more robust than coating layers and have similar functions to the carbon coatings. Depending on whether a binder is used, HPC interlayers can be divided into binder-support interlayers and binder-free ones.

Binder-support interlayers are usually prepared through the following steps: HPC is mixed with binders (usually polytetrafluoroethylene/water dispersion), then rolled into a film, pressed, cut, and finally dried. Compared to the binder-support interlayers, there are several merits for binder-free ones: (1) the synthesis can be more scalable and convenient because most carbon precursor films have good mechanical flexibility and can maintain good integrity during the calcination process; (2) the thickness of the interlayers can be easily controlled by tuning the precursor films; (3) the interlayer could promote better conductivity and higher energy density as no nonconductive binders are used. Thus, herein, we focus on the binder-free interlayers derived from HPCs.

To explore the correlation between the pore structures of HPC interlayers and the electrochemical performances, Wang et al.[164] prepared a series of activated carbon nanofiber (ACNF) interlayers with different pore structures by electrospinning and tuning the activation time under steam/N_2 flow. With the extension of activation, the micropore ratio, SSA, and pore volume were all improved (Figure 15A,B). The cyclic performance of Li–S cells (Figure 15C) is also enhanced to a large extent because the ACNF1 interlayer provides a higher SSA and a larger pore volume for stabilizing more PSs through physical adsorption. In turn, the anchored species can be reutilized in the subsequent conversion. Singhal et al.[153] further investigated the effect of the thickness of interlayers on the cyclic performances of Li–S cells by varying the weight of nonporous carbon nanofibers (NPCNFs) and ACNF interlayers from 1.3 to 4.2 mg cm^{-2} at 0.2 C (Figure 15D). According to the results of the investigation, the cyclic performance became more stable at a low current density when the thicknesses of the interlayers were increased. This is because the chemical reaction rates are controlled by kinetics at a low current density rather than by the mass transfer of Li^+. In addition, more intermediate PSs would be trapped in the cathode region

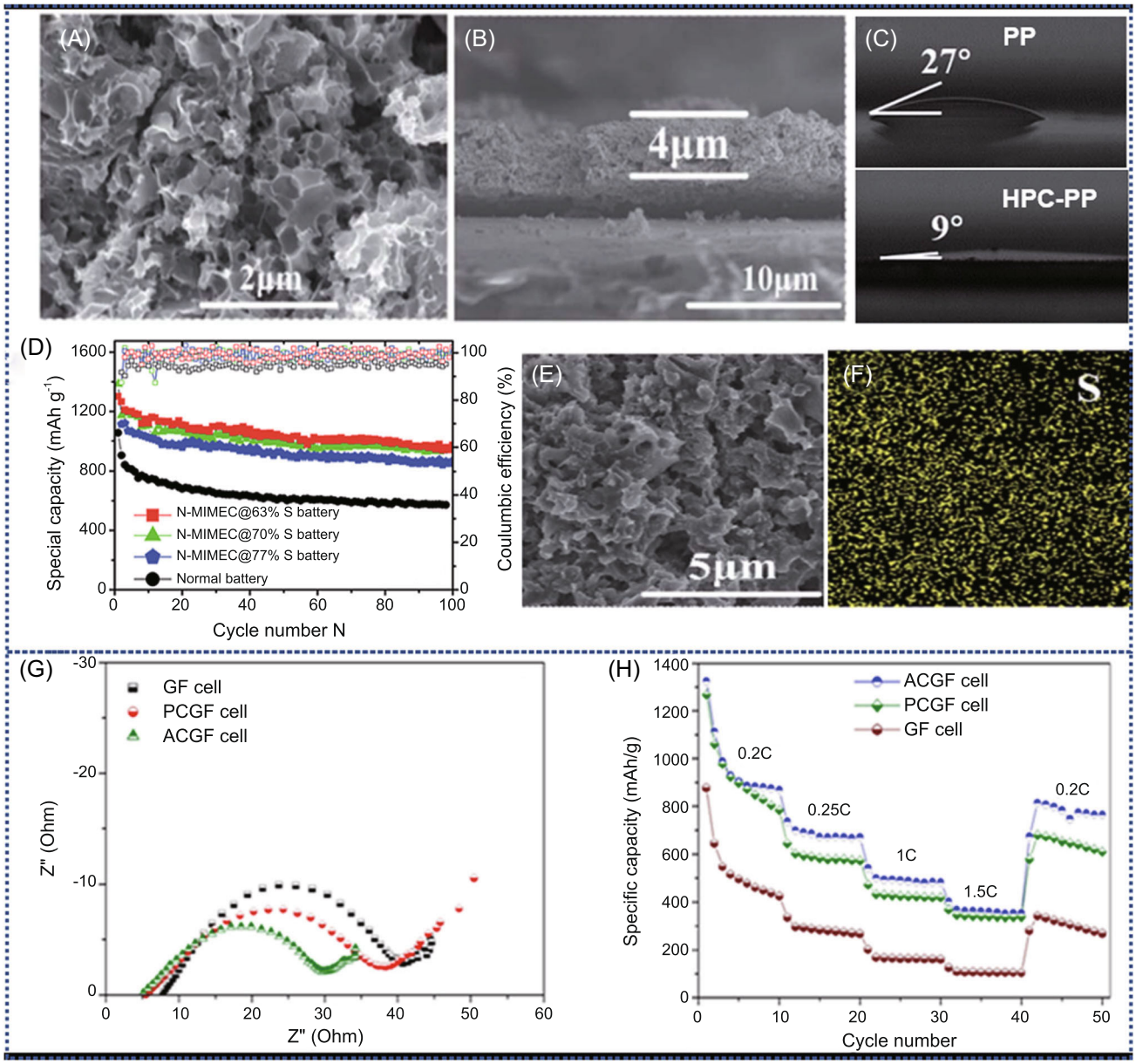

FIGURE 14 Hierarchical porous carbon (HPC)-functionalized polypropylene (PP) separators and their characterizations. Scanning electron microscopy (SEM) images of (A) the top surface and (B) cross-section for HPC-coated PP, respectively. (C) Contact angles toward the electrolyte for PP and HPC-coated PP separators. (D) Cycle performance at 0.1 C for Li–S cells assembled with PP and HPC-coated PP. (E) SEM image and (F) the corresponding energy-dispersive spectroscopy mapping of the S element for HPC-coated PP after five cycles. (G) Electrochemical impedance spectroscopy (EIS) of glass fiber (GF), polycarbonate glass fiber (PCGF), and activated carbon-coated glass fiber (ACGF) cells. (H) Rate performances of GF, PCGF, and ACGF cells. (A–F) Reproduced with permission: Copyright 2017, Royal Society of Chemistry.[132] (H,I) Reproduced with permission: Copyright 2018, Elsevier[189]

by the thicker interlayer. However, no comparison of battery performances with different thicknesses of ACNF interlayers operated at high current densities was provided. Due to the longer migration pathway within the thicker interlayers, it is assumed that the reaction rates can be reduced by the inferior mass transfer of Li^+ at large current densities, thus resulting in poor rate performances. Moreover, the high areal loading of the HPC interlayer (4.2 mg cm^{-2}) undesirably decreases the high energy density of Li–S batteries.

As issues such as low conductivity, volume change, and PS shutting of sulfur cathode would worsen at high sulfur loading, the single functionalization of the sulfur cathode or the separator using HPCs may not meet the requirement for practical applications. The integration of an HPC-modified cathode and an HPC-functionalized

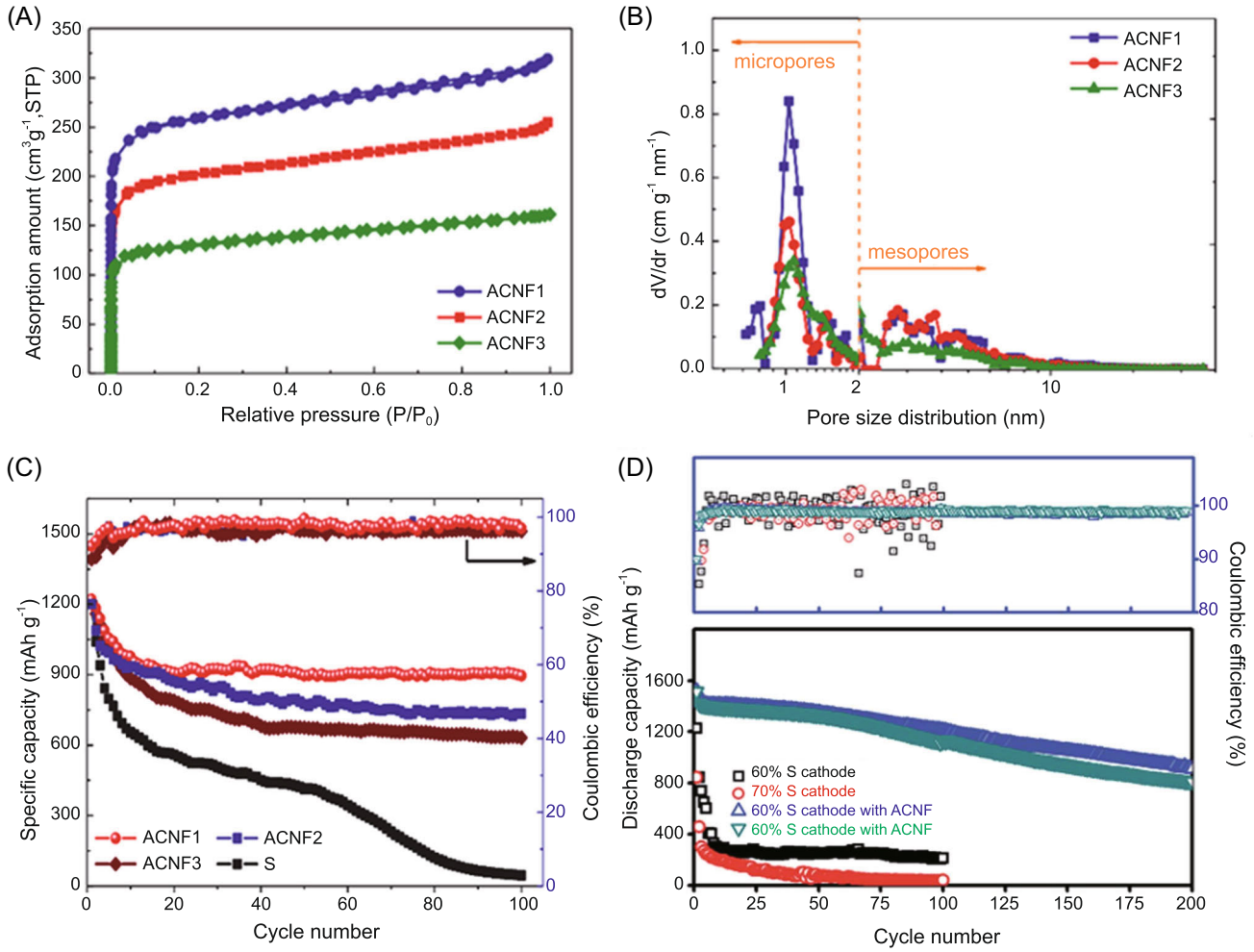

FIGURE 15 (A) N_2 adsorption/desorption isotherms and (B) pore size distribution of activated carbon nanofibers (ACNFs) synthesized by tuning the activation time. (C) Cycling performance and Coulombic efficiency of the Li–S cells with and without using ACNF interlayers. (D) Comparison of cycling performance with varying thicknesses of nonporous carbon nanofibers (NPCNFs) and ACNF interlayers. (A–C) Reproduced with permission; Copyright 2015, Elsevier.[164] (D) Reproduced with permission; Copyright 2015, Royal Society of Chemistry[153]

separator is a good choice, which can further improve the conductivity, confine sulfur species, and promote the commercialization of Li–S batteries. A typical attempt was made by Ye et al.,[35] in which an oval-like carbon microstructure (OLCM) with micro/meso/macropores was adopted as both the sulfur host and coating layers for the separator. When the configurations were integrated into Li–S cells, high stability of 400 cycles was achieved with a high sulfur loading of 8.9 mg cm^{-2} and ultrahigh sulfur content (89%) in the S@OLCM cathode. Remarkably, a 100-cm^2 (10 × 10 cm) pouch cell was assembled using the ultrahigh sulfur-loaded cathode (14 mg cm^{-2}) with an extremely low E/S ratio (electrolyte amount: sulfur mass) of 2.7 μL mg^{-1}, and a high energy density of 460 Wh kg^{-1} was realized at 18.6 Ah, which was more than two times higher than that of traditional LIBs (150–200 Wh kg^{-1}). This study provided a method to design thick electrodes and a possibility to integrate the modified cathode and separator into one Li–S cell, representing a significant step toward the practical application of Li–S batteries.

On the basis of the above discussion, HPC-based interlayers or coating layers have two functions: first, they serve as a second current collector to improve the conductivity of the sulfur cathode and offer additional reaction sites for reutilization of the dissolved and migrated PSs; second, they function as ionic sieves to inhibit the migration of PS ions while allowing the transport of lithium ions. Therefore, abundant micropores and small mesopores are essential for HPC interlayers to perform the two functions. The self-templating method (using biomass or MOFs as carbon precursors) or a method coupled with activation can be an efficient approach for producing the desirable HPCs for interlayers. In addition, more research needs to be conducted to balance the cyclic stability, rate performances, and energy density of

Li–S cells by tuning the thicknesses, microstructures, and mass loadings of HPC interlayers particularly in a lean electrolyte and with the use of thin-Li metal anodes.

5 | HCPS FOR STABILIZING A LI–METAL ANODE

More formidable challenges of Li–S batteries remain with respect to lithium metal anodes, which are subjected to severe deterioration during cyclic discharge and charge that results from the following issues[262–265]: (1) The lithium anode suffers from an infinite volume change during stripping and plating. (2) Due to the low electrode potential and high activity, parasitic reactions occurring between lithium metal and the electrolyte lead to the formation of an SEI film that acts as an ionic conductor but an electrical barrier on the electrode/electrolyte interfaces. In particular, the SEI films are inhomogeneous in chemical composition and thickness, and therefore induce nonuniform flux of lithium ions and dendritic lithium deposition. (3) As the SEI films are fragile and easily broken, a new SEI film is formed in every time of lithium plating, resulting in the continuous consumption of the electrolyte during charging and discharging. (4) During discharge, some of the lithium dendrites lose electrical contact by isolation of SEI debris and form "dead" lithium. The repeated formation of SEI films and inactive lithium causes low energy efficiency, low CE, and poor cyclic stability. (5) Lithium dendrites could penetrate the separator and lead to the short circuit of cells and thus safety risks.

Plating lithium in porous current collectors, which mitigates the volume change of anode, physically suppresses dendrites growth, and provides more electrical contact between lithium and conductor than 2D current collectors, is popularly researched to enhance the performances of lithium anodes.[266–268] Compared to the 2D plane copper current collector, 3D porous carbon materials are lighter and more chemically stable.[269] In addition, the high surface area of porous structures is advantageous in terms of lowering the local current density and thus prolonging Sand's time.[270,271] Generally, the specific surface area of the porous carbon that contains rich micropores/mesopores can be considerably enhanced because of its high density of small pores. Simultaneously, macropores are essential to accommodating a high content of lithium and thus increasing electrode capacity.[272,273] To this end, a bi-/tri-modal hierarchical porous structure can be a promising host material for accommodation of lithium.

For instance, a micro–mesoporous unstacked graphene with a large pore volume ($1.65\ cm^3\ g^{-1}$) was developed using a MgAl-layered double-hydroxide template and used as the lithium anode host. The huge SSA of hierarchical porous graphene enabled demonstration of the proof of concept of regulating the lithium deposition by reducing the local current density. Meanwhile, the large pore volume yielded sufficient space for the formation of protective SEI and buffering the infinite volume change during the lithium stripping/plating (Figure 16A). As expected, the dendrite-free morphology was maintained after a $2.0\ mAh\ cm^{-2}$ ($1.0\ mAh\ cm^{-2} = 1333\ mAh\ g^{-1}$) depositing process with a current of $0.5\ mA\ cm^{-2}$ ($1.0\ mA\ cm^{-2} = 1333\ mA\ g^{-1}$).[274]

Aside from chemically adsorbing PSs, heteroatom dopants can also function as nucleation sites to promote uniform lithium deposition.[51,276] A N-doped carbon framework, with a hierarchically porous structure and a large specific surface area, derived from 3D-printed Zn-MOF, could simultaneously suppress the dendrite growth, accommodate massive Li deposition, stabilize the Li/electrolyte interface, and dissipate high current densities.[277] As a result, the 3D-printed carbon framework delivered an average CE of 97.9% at $1\ mA\ cm^{-2}$ for a capacity of $10\ mAh\ cm^{-2}$ over ~2000 h. Liu et al.[278] demonstrated that the use of a flexible 3D graphitic nitrogen, oxygen-co-doped carbon foam promoted uniform lithium nucleation and growth. The well-distributed doping sites promoted homogeneous lithium nucleus growth with low nucleation overpotential, and then the initial lithium nucleus, serving as the seed layer, regulated the subsequent uniform lithium growth. Combined with other advantages such as high SSA, a 3D porous framework, and lightweight, carbon foam achieved a high CE of 99.6% for 300 cycles and an ultralong lifespan (>1200 h) with low overpotential (<25 mV at $3\ mA\ cm^{-2}$). Similarly, N, O co-doped micro/mesoporous carbon nanosheet arrays were constructed on a Cu foil as the host to inhibit the Li dendrites and to improve the CE. Benefiting from the abundant vertical nanoporous channels with rich lithophilic heteroatom dopants, high CE and long lifespan were achieved in both the carbonate electrolyte and the ether electrolyte.[279] To investigate the exact working mechanism between lithium and dopants, and understand why lithium nucleated homogeneously on HPCs anodes, first-principle calculations were carried out.[36] According to the investigation of electronegativity, local dipole, and charge transfer between nonmetal dopants and lithium atom, oxygen doping, and oxygen, boron co-doping was predicted to show the best lithiophicity among single-doped and co-doped carbons, respectively, which yielded a rational strategy for the design of lithophilic hosts for a stabilized lithium anode.[36]

Instead of nonmetal doping, metal nanoparticles including gold,[34] cobalt,[280,281] nickel,[282] silver,[275,283] zinc,[284] and nickel/cobalt[285] have also been commonly

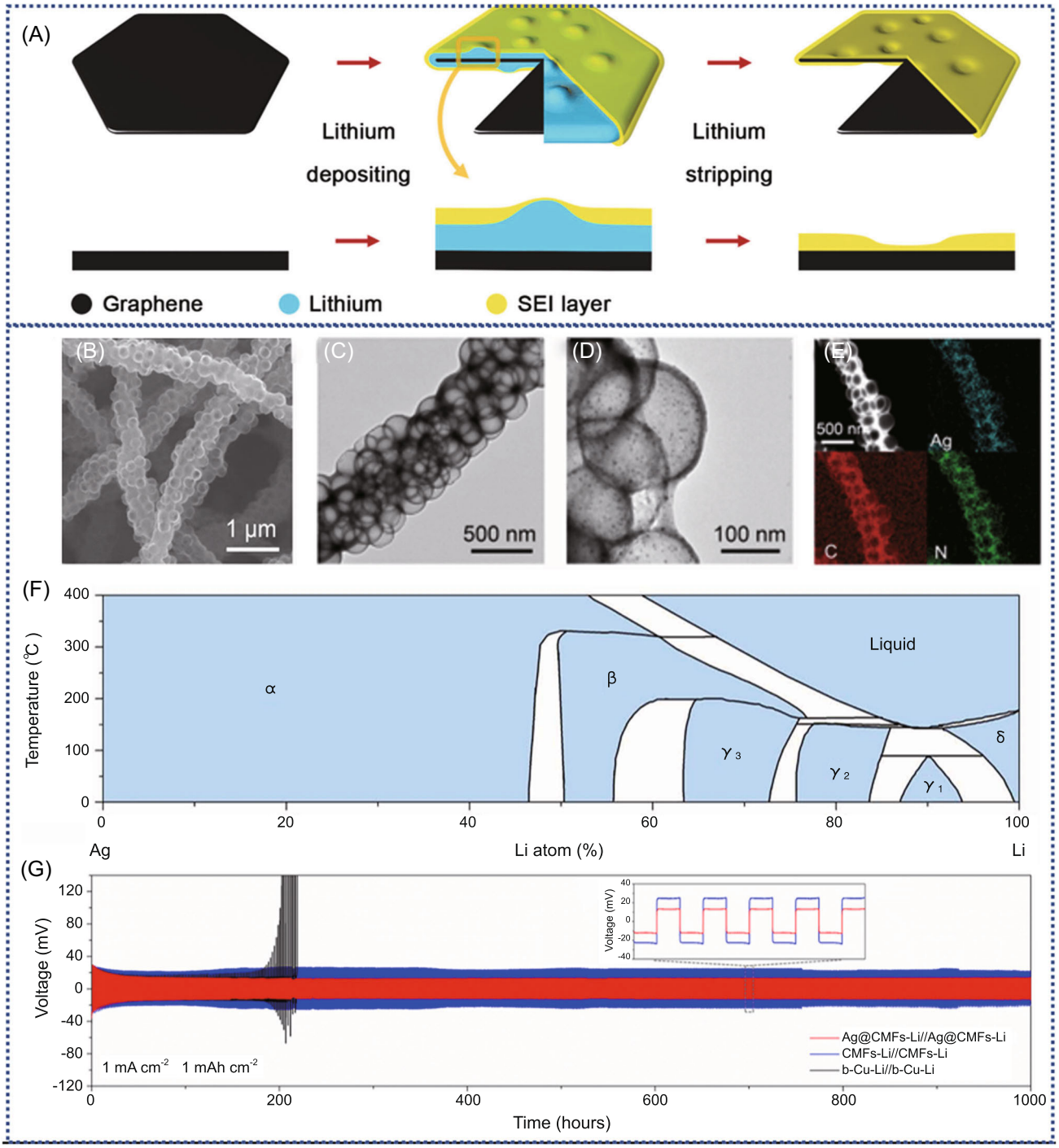

FIGURE 16 Hierarchical porous carbons (HPCs) and their composites utilized for stabilizing the lithium anode. (A) Schematic diagrams of the Li depositing/stripping process on a hierarchical porous graphene flake. (B) Scanning electron microscopy image, (C) transmission electron microscopy (TEM) image, (D) high-resolution TEM image, and (E) corresponding elemental mappings of Ag@CMFs. (F) Ag–Li binary phase diagram. (G) Galvanostatic cycling voltage profiles of bare Cu–Li, CMF–Li, and Ag@CMF–Li anodes in symmetric coin cells at 1 mA cm^{-2} with a capacity of 1 mAh cm^{-2}. (A) Reproduced with permission: Copyright 2016, Wiley.[274] (B–G) Reproduced with permission: Copyright 2021, American Association for the Advancement of Science.[275] CMF, carbon meso–macroporous fiber; SEI, solid electrolyte interphase

introduced into HPCs to improve the affinity toward lithium and to promote even lithium deposition. Taking sliver as an example, Fang et al.[275] embedded Ag nanoparticles into 3D nitrogen-doped carbon meso–macroporous fibers (Ag@N-CMFs) (Figure 16B,C) to accommodate lithium. The 3D hierarchical porous framework could alleviate the infinite volume variation for lithium plating/stripping and lower the local current

density, and the lithiophilic nitrogen dopants could serve as homogeneous sites to reduce the nucleation barrier. Besides, owing to the reversible solid solution-based alloying reaction between silver particles and the lithium film (Figure 15F), the uniformly dispersed silver particles (Figure 16D,E) acted as lithiophilic nucleation seeds to increase the lithium diffusion coefficient, further mitigating the nucleation overpotential and polarization. With these synergetic functions, the Ag@CMFs electrode showed high CE (>98%) for more than 500 cycles, and the Li–Ag@CMFs symmetric cells (Figure 16G) delivered excellent cyclic stability for 1000 h with very small voltage polarization (~10 mV).

Similar to metal nanoparticle seeds, lithiophilic metal oxides and sulfide-functionalized HPCs also showed good potential for stabilizing lithium anodes. Zhang et al.[286] developed a wood-derived 3D carbon scaffold with straight macroporous channels, in-wall mesopores, and a thin lithiophilic ZnO coating to host lithium. Due to the macropores, the 3D carbon scaffold accommodated a high content of lithium, delivering a rather high electrode capacity of 2650 mAh g^{-1}. The channels of the wood-derived carbon could promote the Li stripping/plating processes and effectively restrained the volume change during discharge and charge. Simultaneously, as the thin lithiophilic ZnO layer enabled porous carbon to be easily infused with molten lithium, the Li@ZnO–C electrode-assembled symmetric cell showed a lower overpotential (90 mV at 3 mA cm^{-2}) and better cycling stability (~150 h at 3 mA cm^{-2}) than the symmetric cells with bare Li metal anodes. Later, a bamboo-derived 3D HPC current collector was decorated with ZnO quantum dots and served as a scaffold of a Li metal anode.[287] It was found that the lithiophilic ZnO quantum dots played an important role in regulating uniform lithium deposition. The overpotential for Li stripping/plating was lowered by the lithiophilic ZnO, which worked as nucleation seeds for lithium deposition. However, too many ZnO particles led to shorter cyclic stability compared with the sample with an optimized content (15 wt%), which might be because ZnO took up too much room due to pores and excessive discharge products of Li_2O were formed in the pores. Besides ZnO, other metal oxides and sulfide such as Al_2O_3,[288,289] MgO,[288] MoS_2,[290] and so forth, also showed similar functions of promoting nucleation and plating of lithium when incorporated into HPCs.

To simultaneously inhibit the PS shuttling that arises from the sulfur cathode and the growth of lithium dendrite from the anode, a multifunctional integrated host with lithiophilicity–sulfiphilicity that was composed of bio-derived N-doped micro/meso/macroporous carbon fiber bundles (N-PCFs) with co-imbedded niobium carbide and cobalt nanoparticles (NbC-Co-PCFs) was designed and used as a host for both sulfur and lithium.[37] The 3D carbon skeleton served as a conductive matrix, while the abundant nanopores could physically confine sulfur and lithium and buffer the volume expansion of electrodes. Moreover, the imbedded Co and NbC in the carbon matrix with both lithiophilicity and sulfiphilicity could not only facilitate the adsorption, diffusion, and homogeneous deposition of Li but also promote the adsorption and conversion of LiPSs. Due to the combined benefits of HPC hosts and the embedded lithiophilicity–sulfiphilicity active sites, the Li–S full cells (S@ NbC-Co-PCFs || Li@ NbC-Co-PCFs) showed excellent electrochemical performance (915 mAh g^{-1}, 6.1 mAh cm^{-2}) under high sulfur loading of 6.7 mg cm^{-2}, fulfilling the requirement for the use of Li–S batteries in electric vehicles.[11,37] Remarkably, the N/P capacity ratio (lithium anode/sulfur cathode) for the Li–S full cells was as low as 1.7, demonstrating the potential application of functionalized HPCs in practical Li–S batteries.

As the volume change of lithium during lithium plating/stripping is infinite, large pore volume for HPCs is required when HPCs are used as Li hosts. In contrast to the sulfur host, which needs a high specific surface area, excessive specific surface is unsuitable for the Li host, which can lead to serious side reactions between the lithium anode and the electrolyte.[50] Instead, a moderate specific surface is more suitable for HPCs used as the Li host to reduce the local current density during lithium deposition without serious side effects. Therefore, meso/macroporous carbons with a large pore volume, a moderate specific surface area, highly ordered pores, and adequate lithophilic sites could be ideal Li hosts, which can be synthesized using the hard and soft templating method by the introduction of some lithophilic seeds. Additionally, the integration of an optimized S@HPC cathode and a Li@HPC anode into one Li–S full cell may resolve the issues arising from both the cathode and the anode and further promote the development for Li–S batteries.

6 | SUMMARY AND PERSPECTIVES

In summary, recent research developments in the synthesis of HPCs and the rational design of HPC structures toward sulfur cathodes, separators and interlayers, and lithium anodes are reviewed and discussed. More specifically, a comprehensive understanding gained so far on the correlation between the pore structures of HPCs and the electrochemical performance of the S@HPCs cathodes is discussed. Due to the unique multimodal porous structures, HPCs that have high pore

volume, SSA, and capillary force show great potential for Li–S batteries.

As a highly controllable and reproducible method, the hard-templating synthetic strategy has apparent merits for use in the synthesis of HPCs with anticipative microstructures including morphologies, particle sizes, and porous structures. However, the hard-templating technique might not be feasible for large-scale production on account of the need for a large amount of templates, sophisticated preparation procedures, and time-consuming template-removal processes. The use of some templates such as transition metallic templates can increase the preparation costs. Cheap, abundant, and easily etched templates such as sodium chloride, magnesium oxides, and calcium oxides are preferable for the scalable production of HPCs. The soft templates can lead to the formation of HPCs with ordered mesoporous walls and can be removed easily by calcination, but the electrostatic self-assembly between the carbon precursors and surfactants usually occurs in organic solvents and is also sophisticated and time-consuming. As some soft templates reshape during elevated temperatures, calcination could damage the soft templates and assembled structures and lead to unwanted porous/nonporous structures. Template-free methods for synthesizing HPCs are advantageous in terms of the direct calcination of carbon feedstocks without using templates but are limited to well-tuning the porous structures. The hard and soft-templating method can combine the merits of hard templates and soft templates and is very effective for the construction of 2D and 3D ordered HPCs, but it also simultaneously has the disadvantages of hard templates and soft templates. The activation step can endow HPCs with abundant micropores and ultrahigh specific surface area, but the process is also time-consuming with high-temperature treatment. To achieve optimal HPC structures with high SSA, high pore volume, and ordered pores by a facile, low-cost, and controllable method, a combination of these methods (e.g., hard/soft templates, physical or chemical activation, and template-free carbon precursors) might work. In addition, according to different requirements for different components (e.g., sulfur host, interlayers/coating layers for separators, and lithium host) in Li–S batteries, a suitable synthetic method needs to be adopted for preparing HPCs.

As summarized in Tables 1 and 3, significant progress in the development of Li–S cells with the use of HPCs as conductive sulfur scaffolds, coating layers on separators, and functional interlayers has been achieved from the physical interactions (e.g., physical adsorption and spatial confinement for HPCs without heteroatoms) to interfacial chemical interactions (e.g., chemisorption and conversion for heteroatoms-doped HPCs), aiming at increasing the sulfur utilization and decreasing the dissolution and migration of PS ions. Through the introduction of HPCs, Li–S batteries show considerably enhanced discharge capacity, cyclic stability, and CE. Although many advances have been successfully shown in laboratory, a large gap, mainly arising from the different metrics, still exists between academia and industry. The metrics such as areal sulfur loadings, sulfur contents, active materials utilization, electrolyte amounts (or the ratio of electrolyte to sulfur), anode/cathode (N/P) capacity ratio, contents of nonactive cell components, and voltage hysteresis have often been neglected previously in academia, but they are fairly important to industry as they are linked to the practical energy density, power density, and energy efficiency of Li–S cells. To bridge the gap, in future research, the following metrics need to be carefully taken into account: high-sulfur-loading cathodes (e.g., $>6\ mg\ cm^{-2}$), high sulfur contents (e.g., >70 wt%), high sulfur utilization (e.g., >80%), low E/S ratio (e.g., $<5\ \mu L\ mg^{-1}$), and low N/P capacity ratio (e.g., <2) for pouch cells toward practical applications.[11,273] To this end, we need to revisit many previous results obtained that did not fulfill these metrics as the metrics have an influence on the electrode and battery performances. Thus, achievement of these metrics gives rise to more challenges in developing the HPC components for Li–S cells.

For cathodes, since the structures of HPCs (e.g., SSA, pore volume, and ordering degree, heteroatom doping) are strongly related to the characteristics of composite cathodes (e.g., sulfur content, loading, and utilization) and battery performances (e.g., discharge capacity, cyclic stability, and energy density), the pore structures of HPCs need to be further optimized in terms of the metrics to enhance the practical battery performances. Moreover, under critical conditions, the electrode reactions become more sluggish and drastically decrease the rate performances. In addition, more insights into the mass transfer in electrodes, electrodes/interface reactions, and surface interactions between active materials and host materials by theoretical studies are required.

The HPC-modified separators and HPC interlayers have indeed been proven to be efficient in preventing the PS shuttle and prolonging the battery lifespan (Table 3). However, challenges still remain mainly in the HPC-based interlayers associated with the effectiveness, areal mass loadings, porosities, and stability of the interlayers. The effectiveness is mainly linked to mitigating the "shuttle effect" of PSs. First, there is a lack of insights with respect to the permeation behaviors and mechanisms of PSs, lithium ions, and solvent molecules within the nanosized channels such as micropores. Second, in many cases, the interlayers are composed of micro/

mesoporous HPC particles and also many voids/large pores between particles, reducing the effectiveness. Third, the effectiveness is also associated with the thickness of the interlayers. In general, thicker layers can increase the diffusion resistance of particles. Balancing the thickness and battery performances such as the rate performances can be difficult. The areal mass loadings are related to the density and thickness of the interlayer. Thick interlayers with high mass loadings are not preferable as they increase the component weight too much and accommodate too much electrolyte, both of which are detrimental to the energy density. However, thin layers could reduce the effectiveness as mentioned above. In general, the lower porosity is better as it requires smaller amount of electrolyte thus decreasing E/S ratio. On the other hand, slightly higher porosity can enable reutilization and accommodation of more PSs, improving the battery capacity. Thus, determination of the effect of porosity on the cell performances requires more investigations. As is well known, a stable interlayer is essential for durability. However, in many cases, HPC interlayers are brittle and easily develop microcracks due to the external pressure and internal nonuniform reactions. Some HPC interlayers have low adhesion to the separators and are often delaminated from the separators. All these challenges need to be addressed in future research.

Investigations on thin lithium metal anodes are of significance for practical use as well. In a laboratory, a thick Li foil is usually used as the anode to evaluate the performance of designed cathodes and separators. However, excessive Li can compensate the negative effects of Li dendrites and consumption of lithium in the long-term cycling test, especially in batteries with high sulfur loading and lean-electrolyte conditions. Batteries assembled with thin lithium electrodes often degrade much faster than those using thick lithium electrodes. In addition, when designing and developing practical high-sulfur-loading batteries, the issues of Li dendrites, unstable SEI, and Li corrosion need to be taken into account for both fundamental research and practical applications, as these issues would become more serious along with the increased sulfur content. Although some strategies have been put forward to develop thin Li anodes and suppress the growth of Li dendrites, most of the Li metal anodes reported to date are operated at low current densities and low capacities. It is still a major challenge to construct Li metal anodes with high capacity and rate performance to match the cathodes with high sulfur loading ($>6\ mg\ cm^{-2}$).

To overcome the above obstacles, future development of HPCs for Li–S batteries can benefit from focusing on the following aspects. First, development of scalable and cost-effective strategies for the production of HPCs still requires more efforts. Properties such as pore volume, SSA, electrical conductivity, heteroatom doping, and microstructures should be comprehensively controlled to meet the requirements for S@HPC cathodes with high sulfur contents, high loadings, and high utilization for practical applications. To realize optimized structures, to simplify the synthesis procedures, and to reduce the costs, a combination of various methods might be worthy of further investigations. Second, the design and fabrication of high-performance S@HPCs cathodes play a vital role in promoting the practical applications of Li–S cells. Thus, correlations between electrochemical performances of HCP-based batteries and several key parameters such as high sulfur contents, electrode capacity, areal sulfur loadings, and low electrolyte/sulfur (E/S) ratios require more investigations. More efforts also need to be devoted toward exploring novel S@HPC architectures to facilitate the reaction kinetics and improve the power densities. For example, surface chemistry such as heteroatom-doping to improve the sulfiphilicity of HPCs can further suppress the PS migration through chemisorption. Decoration of HPCs with catalysts can be performed to accelerate the chemical conversion of active materials, reducing the overpotential and improving power densities of batteries. Simulations on mass transfer within electrodes and electrode reactions and DFT calculations of the interaction between PSs and surface functional groups such as N or O heteroatoms and catalysts are highly recommended for guiding experimental studies.

Third, separators functionalized with HPCs could effectively enhance the conductivity and suppress the migration of PSs, playing an important role in the operation of high-sulfur-loading batteries. According to the above-mentioned challenges, the following pathways can be taken into account: first, based on experiments, simulation, and calculations, the picture of permeable behaviors of PSs needs to be well drawn. Under the practical metrics addressed above (e.g., S loading $>6\ mg\ cm^{-2}$, S contents $>70\ wt\%$, high S utilization, low E/S ratio (e.g., $<5\ \mu L\ mg^{-1}$), low N/P ratio, and pouch cell tests), investigations on the reduction of the thickness of coating layers without sacrificing the capacity and effect of suppressing the PS shuttle can be performed. Development of facile and scalable routes such as roll-to-roll printing and other coating techniques adoptable in industry for producing a large-area and uniform coatings/interlayers is meaningful.

In addition, the freestanding S@HPCs cathodes or Li@HPCs anodes can reduce the ratio of inactive materials. HPCs can be tailored as lightweight current collectors with areal density below $1\ mg/cm^2$ for $50\ \mu m$

thickness to replace the traditional current collectors of copper foil (>8.5 mg/cm^2 for 9 μm thick) and aluminum foil (>3.0 mg/cm^2 for 12 μm thick), thus leading to a marked increase in the energy density of Li–S cells. Although considerable progress has been made, relevant research is still important and needs to be conducted more in the future with respect to the electrode's mechanical stability, flexibility, high loadings of active materials, electrode/battery performances, durability, thin electrode production technologies, scalability, and so forth. In terms of the above factors, this review work also provides guidelines on the synthesis strategies, design, and effects of thin HPC current collectors on the battery performances. The use of sulfiphilic or lithiophilic materials (e.g., metal, metal oxides, sulfides, carbides and nitrides, and single-atom seeds) that facilitate the chemical adsorption and conversion of PS ions or promote uniform lithium deposition could be further helpful for achievement of high energy densities.

Last but not the least, configurations integrating the different components (S@HPC cathode, HPC-coated separator, and S@HPCs anode) into one Li–S cell can simultaneously resolve the problems of sulfur cathodes and lithium anodes. Furthermore, more research needs to be focused on theoretical simulations and in situ characterizations, which can provide a more in-depth understanding of the role and working mechanism of HPCs during battery operation and in turn promote optimization of the structures of HPCs. Although there are still several formidable obstacles that hinder the practical applications of Li–S batteries, the recent progress made demonstrates that rationally designed HPCs with high pore volume and SSA, ordered structures, and optimal heteroatom doping can be one of the most desirable materials to promote the development of this promising energy storage system.

ACKNOWLEDGMENT

Yinyu Xiang is very grateful to the China Scholarship Council (CSC; No. 201806950083) for his PhD scholarship.

CONFLICTS OF INTEREST

The authors declare no conflicts of interest.

ORCID

Yutao Pei http://orcid.org/0000-0002-1817-2228

REFERENCES

1. Tarascon JM, Armand M. Issues and challenges facing rechargeable lithium batteries. *Nature*. 2001;414(6861):359-367.
2. Dunn B, Kamath H, Tarascon JM. Electrical energy storage for the grid: a battery of choices. *Science*. 2011;334(6058):928-935.
3. Simon P, Gogotsi Y. Materials for electrochemical capacitors. *Nat Mater*. 2008;7(11):845-854.
4. Armand M, Tarascon JM. Building better batteries. *Nature*. 2008;451(7179):652-657.
5. Goodenough JB, Kim Y. Challenges for rechargeable Li batteries. *Chem Mater*. 2010;22(3):587-603.
6. Yang Z, Zhang J, Kintner-Meyer MC, et al. Electrochemical energy storage for green grid. *Chem Rev*. 2011;111(5):3577-3613.
7. Bruce PG, Freunberger SA, Hardwick LJ, Tarascon JM. Li-O_2 and Li–S batteries with high energy storage. *Nat Mater*. 2012;11(1):19-29.
8. Manthiram A, Fu YZ, Chung SH, Zu CX, Su YS. Rechargeable lithium–sulfur batteries. *Chem Rev*. 2014;114(23):11751-11787.
9. Yin YX, Xin S, Guo YG, Wan LJ. Lithium–sulfur batteries: electrochemistry, materials, and prospects. *Angew Chem Int Ed*. 2013;52(50):13186-13200.
10. Ji XL, Nazar LF. Advances in Li–S batteries. *J Mater Chem*. 2010;20(44):9821-9826.
11. Peng H-J, Huang J-Q, Cheng X-B, Zhang Q. Review on high-loading and high-energy lithium–sulfur batteries. *Adv Energy Mater*. 2017;7(24):1700260.
12. Li BQ, Kong L, Zhao CX, et al. Expediting redox kinetics of sulfur species by atomic-scale electrocatalysts in lithium–sulfur batteries. *InfoMat*. 2019;1(4):533-541.
13. Tang R, Zhu Z, Li C, et al. Carbon-based flexible self-supporting cathode for lithium–sulfur batteries: progress and perspective. *Carbon Energy*. 2021;3(2):271-302.
14. Zhang CF, Cui LF, Abdolhosseinzadeh S, Heier J. Two-dimensional mxenes for lithium-sulfur batteries. *InfoMat*. 2020;2(4):613-638.
15. Queneau Y, Han B. Interface issues of lithium metal anode for high-energy batteries: challenges, strategies, and perspectives. *InfoMat*. 2021;3(2):155-174.
16. Dai Y-Y, Xu C-M, Liu X-H, et al. Manipulating metal–sulfur interactions for achieving high-performance S cathodes for room temperature Li/Na–sulfur batteries. *Carbon Energy*. 2021;3(2):253-270.
17. Li J, Kong Z, Liu X, et al. Strategies to anode protection in lithium metal battery: a review. *InfoMat*. 2021;3(12):1333-1363.
18. Li Z, Huang Y, Yuan L, Hao Z, Huang Y. Status and prospects in sulfur-carbon composites as cathode materials for rechargeable lithium–sulfur batteries. *Carbon*. 2015;92:41-63.
19. Xiang Y, Li J, Lei J, et al. Advanced separators for lithium-ion and lithium–sulfur batteries: a review of recent progress. *ChemSusChem*. 2016;9(21):3023-3039.
20. Jeong YC, Kim JH, Nam S, Park CR, Yang SJ. Rational design of nanostructured functional interlayer/separator for advanced Li–S batteries. *Adv Funct Mater*. 2018;28(38):1707411.
21. Wang H, Yang Y, Liang Y, et al. Graphene-wrapped sulfur particles as a rechargeable lithium–sulfur battery cathode material with high capacity and cycling stability. *Nano Lett*. 2011;11(7):2644-2647.
22. Dai CL, Sun GQ, Hu LY, Xiao YK, Zhang ZP, Qu LT. Recent progress in graphene-based electrodes for flexible batteries. *InfoMat*. 2020;2(3):509-526.
23. Zhou G, Wang DW, Li F, et al. A flexible nanostructured sulphur-carbon nanotube cathode with high rate performance for Li–S batteries. *Energy Environ Sci*. 2012;5(10):8901-8906.

24. Zhou GM, Zhao YB, Manthiram A. Dual-confined flexible sulfur cathodes encapsulated in nitrogen-doped double-shelled hollow carbon spheres and wrapped with graphene for Li–S batteries. *Adv Energy Mater*. 2015;5(9):1402263.
25. Ji LW, Rao MM, Aloni S, Wang L, Cairns EJ, Zhang YG. Porous carbon nanofiber–sulfur composite electrodes for lithium/sulfur cells. *Energy Environ Sci*. 2011;4(12):5053-5059.
26. Liu M, Wu F, Zheng L, et al. Nature-inspired porous multichannel carbon monolith: molecular cooperative enables sustainable production and high-performance capacitive energy storage. *InfoMat*. 2021;3(10):1154-1170.
27. Shi Y, Liu G, Jin R, Xu H, Wang Q, Gao S. Carbon materials from melamine sponges for supercapacitors and lithium battery electrode materials: a review. *Carbon Energy*. 2019;1(2):253-275.
28. Ji X, Lee KT, Nazar LF. A highly ordered nanostructured carbon–sulphur cathode for lithium–sulphur batteries. *Nat Mater*. 2009;8(6):500-506.
29. Liang C, Dudney NJ, Howe JY. Hierarchically structured sulfur/carbon nanocomposite material for high-energy lithium battery. *Chem Mater*. 2009;21(19):4724-4730.
30. Su Y-S, Manthiram A. Lithium–sulphur batteries with a microporous carbon paper as a bifunctional interlayer. *Nat Commun*. 2012;3(1):1166.
31. Huang J-Q, Liu X-F, Zhang Q, et al. Entrapment of sulfur in hierarchical porous graphene for lithium–sulfur batteries with high rate performance from-40 to 60°C. *Nano Energy*. 2013;2(2):314-321.
32. Zhang L, Wang Y, Peng B, et al. Preparation of a macroscopic, robust carbon-fiber monolith from filamentous fungi and its application in Li–S batteries. *Green Chem*. 2014;16(8):3926-3934.
33. Hou T-Z, Chen X, Peng H-J, et al. Design principles for heteroatom-doped nanocarbon to achieve strong anchoring of polysulfides for lithium–sulfur batteries. *Small*. 2016;12(24):3283-3291.
34. Yan K, Lu Z, Lee HW, et al. Selective deposition and stable encapsulation of lithium through heterogeneous seeded growth. *Nat Energy*. 2016;1(3):16010.
35. Ye Y, Wu F, Liu Y, et al. Toward practical high-energy batteries: a modular-assembled oval-like carbon microstructure for thick sulfur electrodes. *Adv Mater*. 2017;29(48):1700598.
36. Chen X, Chen X-R, Hou T-Z, et al. Lithiophilicity chemistry of heteroatom-doped carbon to guide uniform lithium nucleation in lithium metal anodes. *Sci Adv*. 2019;5(2):eaau7728.
37. Wei Y, Wang B, Zhang Y, et al. Rational design of multifunctional integrated host configuration with lithiophilicity-sulfiphilicity toward high-performance Li–S full batteries. *Adv Funct Mater*. 2021;31(3):2006033.
38. Wang JG, Xie KY, Wei BQ. Advanced engineering of nanostructured carbons for lithium–sulfur batteries. *Nano Energy*. 2015;15:413-444.
39. Sing KSW. Reporting physisorption data for gas/solid systems with special reference to the determination of surface area and porosity (recommendations 1984). *Pure Appl Chem*. 1985;57(4):603-619.
40. Zhang L, Wang Y, Niu Z, Chen J. Advanced nanostructured carbon-based materials for rechargeable lithium–sulfur batteries. *Carbon*. 2019;141(46):400-416.
41. Dutta S, Bhaumik A, Wu KCW. Hierarchically porous carbon derived from polymers and biomass: effect of interconnected pores on energy applications. *Energy Environ Sci*. 2014;7(11):3574-3592.
42. Xu TT, Xue CF, Zhang ZL, Hao XG. Hierarchically porous carbon materials templated from skeletonal polyurethane foam. *Prog Chem*. 2014;26(12):1924-1929.
43. Sun M-H, Huang S-Z, Chen L-H, et al. Applications of hierarchically structured porous materials from energy storage and conversion, catalysis, photocatalysis, adsorption, separation, and sensing to biomedicine. *Chem Soc Rev*. 2016;45(12):3479-3563.
44. Sun M, Chen C, Chen L, Su B. Hierarchically porous materials: synthesis strategies and emerging applications. *Front Chem Sci Eng*. 2016;10(3):301-347.
45. Bae W-G, Kim HN, Kim D, Park S-H, Jeong HE, Suh K-Y. 25th anniversary article: scalable multiscale patterned structures inspired by nature: the role of hierarchy. *Adv Mater*. 2014;26(5):675-700.
46. Imtiaz S, Zhang J, Zafar ZA, et al. Biomass-derived nanostructured porous carbons for lithium–sulfur batteries. *Sci China Mater*. 2016;59(5):389-407.
47. Liu T, Zhang F, Song Y, Li Y. Revitalizing carbon supercapacitor electrodes with hierarchical porous structures. *J Mater Chem A*. 2017;5(34):17705-17733.
48. Liu PT, Wang YY, Liu JH. Biomass-derived porous carbon materials for advanced lithium sulfur batteries. *J Energy Chem*. 2019;34:171-185.
49. Hu Z, Wang C, Wang C, et al. Uncovering the critical impact of the solid electrolyte interphase structure on the interfacial stability. *InfoMat*. 2021:1-11. doi:10.1002/inf2.12249
50. Ni S, Tan S, An Q, Mai L. Three dimensional porous frameworks for lithium dendrite suppression. *J Energy Chem*. 2020;44:73-89.
51. Lee J, Lee TH, Jang HW, Park HS. Chemical modification of ordered/disordered carbon nanostructures for metal hosts and electrocatalysts of lithium-air batteries. *InfoMat*. 2022;4(1):e12268.
52. Feng J, Gao Z, Sheng L, Hao Z, Wang FR. Progress and perspective of interface design in garnet electrolyte-based all-solid-state batteries. *Carbon Energy*. 2021;3(3):385-409.
53. Wang J, Kang Q, Yuan J, et al. Dendrite-free lithium and sodium metal anodes with deep plating/stripping properties for lithium and sodium batteries. *Carbon Energy*. 2021;3(1):153-166.
54. Yan X, Lin L, Chen Q, et al. Multifunctional roles of carbon-based hosts for Li–metal anodes: a review. *Carbon Energy*. 2021;3(2):303-329.
55. Qu Y, Zhang Z, Zhang X, et al. Synthesis of hierarchical porous honeycomb carbon for lithium–sulfur battery cathode with high rate capability and long cycling stability. *Electrochim Acta*. 2014;137:439-446.
56. Liu S, Xie K, Li Y, et al. Graphene oxide wrapped hierarchical porous carbon–sulfur composite cathode with enhanced cycling and rate performance for lithium–sulfur batteries. *RSC Adv*. 2015;5(8):5516-5522.
57. Choudhury S, Ebert T, Windberg T, et al. Hierarchical porous carbon cathode for lithium–sulfur batteries using carbon derived from hybrid materials synthesized by twin polymerization. *Part Part Syst Charact*. 2018;35(12):1800364.
58. Liu X, Liu X, Sun B, et al. Carbon materials with hierarchical porosity: effect of template removal strategy and study on their electrochemical properties. *Carbon*. 2018;130:680-691.

59. Zhao X, Kim M, Liu Y, et al. Root-like porous carbon nanofibers with high sulfur loading enabling superior areal capacity of lithium–sulfur batteries. *Carbon*. 2018;128:138-146.
60. Chen M, Su Z, Jiang K, Pan Y, Zhang Y, Long D. Promoting sulfur immobilization by a hierarchical morphology of hollow carbon nanosphere clusters for high-stability Li–S battery. *J Mater Chem A*. 2019;7(11):6250-6258.
61. Wang M, Zhang H, Zhou W, Yang X, Li X, Zhang H. Rational design of a nested pore structure sulfur host for fast Li/S batteries with a long cycle life. *J Mater Chem A*. 2016;4(5):1653-1662.
62. Hu W, Hirota Y, Zhu Y, et al. Separator decoration with cobalt/nitrogen codoped carbon for highly efficient polysulfide confinement in lithium–sulfur batteries. *ChemSusChem*. 2017;10(18):3557-3564.
63. Wu P, Sun M-H, Yu Y, et al. Physical and chemical dual-confinement of polysulfides within hierarchically meso-microporous nitrogen-doped carbon nanocages for advanced Li–S batteries. *RSC Adv*. 2017;7(68):42627-42633.
64. Wu F, Zhao S, Chen L, et al. Electron bridging structure glued yolk-shell hierarchical porous carbon/sulfur composite for high-performance Li–S batteries. *Electrochim Acta*. 2018;292:199-207.
65. Li C, Yu J, Xue S-L, et al. Wood-inspired multi-channel tubular graphene network for high-performance lithium–sulfur batteries. *Carbon*. 2018;139:522-530.
66. Yu L, Brun N, Sakaushi K, Eckert J, Titirici MM. Hydrothermal nanocasting: synthesis of hierarchically porous carbon monoliths and their application in lithium–sulfur batteries. *Carbon*. 2013;61:245-253.
67. Schneider A, Janek J, Brezesinski T. Improving the capacity of lithium–sulfur batteries by tailoring the polysulfide adsorption efficiency of hierarchical oxygen/nitrogen-functionalized carbon host materials. *Phys Chem Chem Phys*. 2017;19(12):8349-8355.
68. Han P, Chung SH, Manthiram A. Pyrrolic-type nitrogen-doped hierarchical macro/mesoporous carbon as a bifunctional host for high-performance thick cathodes for lithium–sulfur batteries. *Small*. 2019;15(16):1900690.
69. Guo D, Chen X, Wei H, et al. Controllable synthesis of highly uniform flower-like hierarchical carbon nanospheres and their application in high performance lithium–sulfur batteries. *J Mater Chem A*. 2017;5(13):6245-6256.
70. Yu Z, Liu M, Guo D, et al. Radially inwardly aligned hierarchical porous carbon for ultra-long-life lithium–sulfur batteries. *Angew Chem Int Ed*. 2020;59(16):6406-6411.
71. Schneider A, Weidmann C, Suchomski C, Sommer H, Janek J, Brezesinski T. Ionic liquid-derived nitrogen-enriched carbon/sulfur composite cathodes with hierarchical microstructure-a step toward durable high-energy and high-performance lithium–sulfur batteries. *Chem Mater*. 2015;27(5):1674-1683.
72. Reitz C, Breitung B, Schneider A, et al. Hierarchical carbon with high nitrogen doping level: a versatile anode and cathode host material for long-life lithium-ion and lithium–sulfur batteries. *ACS Appl Mater Interfaces*. 2016;8(16):10274-10282.
73. Lyu Z, Xu D, Yang L, et al. Hierarchical carbon nanocages confining high-loading sulfur for high-rate lithium–sulfur batteries. *Nano Energy*. 2015;12:657-665.
74. Lu LQ, Schriever N, de Hosson JTM, Pei YT. Low-temperature solid-state growth of three-dimensional bicontinuous nanoporous graphene with tunable porosity for lithium–sulfur batteries. *J Mater Chem A*. 2018;6(24):11405-11415.
75. Diez N, Ferrero GA, Sevilla M, Fuertes AB. A sustainable approach to hierarchically porous carbons from tannic acid and their utilization in supercapacitive energy storage systems. *J Mater Chem A*. 2019;7(23):14280-14290.
76. Xi K, Kidambi PR, Chen R, et al. Binder free three-dimensional sulphur/few-layer graphene foam cathode with enhanced high-rate capability for rechargeable lithium sulphur batteries. *Nanoscale*. 2014;6(11):5746-5753.
77. Wu F, Shi L, Mu D, Xu H, Wu B. A hierarchical carbon fiber/sulfur composite as cathode material for Li–S batteries. *Carbon*. 2015;86:146-155.
78. Luo C, Niu S, Zhou G, et al. Dual-functional hard template directed one-step formation of a hierarchical porous carbon-carbon nanotube hybrid for lithium–sulfur batteries. *Chem Commun*. 2016;52(82):12143-12146.
79. Guo Q, Sun S, Kim K, et al. A novel one-step reaction sodium–sulfur battery with high areal sulfur loading on hierarchical porous carbon fiber. *Carbon Energy*. 2021;3(3):440-448.
80. Tang Y, Sha J, Wang N, et al. Covalently bonded 3D rebar graphene foam for ultrahigh-areal-capacity lithium–metal anodes by in-situ loose powder metallurgy synthesis. *Carbon*. 2020;158:536-544.
81. Du L, Wu Q, Yang L, et al. Efficient synergism of electrocatalysis and physical confinement leading to durable high-power lithium–sulfur batteries. *Nano Energy*. 2019;57:34-40.
82. Niu S-Z, Wu S-D, Lu W, Yang Q-H, Kang F-Y. A one-step hard-templating method for the preparation of a hierarchical microporous-mesoporous carbon for lithium–sulfur batteries. *New Carbon Mater*. 2017;32(4):289-296.
83. Tang C, Li B-Q, Zhang Q, et al. CaO-templated growth of hierarchical porous graphene for high-power lithium–sulfur battery applications. *Adv Funct Mater*. 2016;26(4):577-585.
84. Liao H, Zhang H, Hong H, Li Z, Lin Y. Novel flower-like hierarchical carbon sphere with multi-scale pores coated on PP separator for high-performance lithium–sulfur batteries. *Electrochim Acta*. 2017;257:210-216.
85. Hu G, Sun Z, Shi C, et al. A sulfur-rich copolymer@CNT hybrid cathode with dual-confinement of polysulfides for high-performance lithium–sulfur batteries. *Adv Mater*. 2017;29(11):1603835.
86. Wang J-G, Liu H, Zhang X, Li X, Liu X, Kang F. Green synthesis of hierarchically porous carbon nanotubes as advanced materials for high-efficient energy storage. *Small*. 2018;14(13):13.
87. Zhang Y, Li G, Wang J, et al. Hierarchical defective $Fe_{3-x}C$@C hollow microsphere enables fast and long-lasting lithium–sulfur batteries. *Adv Funct Mater*. 2020;30(22):2001165.
88. Feng S, Song J, Fu S, et al. One-step synthesis of carbon nanosheet-decorated carbon nanofibers as a 3D interconnected porous carbon scaffold for lithium–sulfur batteries. *J Mater Chem A*. 2017;5(45):23737-23743.
89. Jiang P, Deng W, Zhou XF, Feng JW, Liu ZP. Vapor-assisted synthesis of hierarchical porous graphitic carbon materials

towards energy storage devices. *J Power Sources*. 2019;425:10-16.
90. Wang D-W, Li F, Liu M, Lu GQ, Cheng H-M. 3D aperiodic hierarchical porous graphitic carbon material for high-rate electrochemical capacitive energy storage. *Angew Chem Int Ed*. 2008;120(2):379-382.
91. Xu G, Ding B, Nie P, Shen L, Dou H, Zhang X. Hierarchically porous carbon encapsulating sulfur as a superior cathode material for high performance lithium-sulfur batteries. *ACS Appl Mater Interfaces*. 2014;6(1):194-199.
92. Zheng Z, Guo H, Pei F, et al. High sulfur loading in hierarchical porous carbon rods constructed by vertically oriented porous graphene-like nanosheets for Li–S batteries. *Adv Funct Mater*. 2016;26(48):8952-8959.
93. Miao X, Sun D, Zhou X, Lei Z. Designed formation of nitrogen and sulfur dual-doped hierarchically porous carbon for long-life lithium and sodium ion batteries. *Chem Eng J*. 2019;364:208-216.
94. Zhao M-Q, Peng H-J, Tian G-L, et al. Hierarchical vine-tree-like carbon nanotube architectures: in-situ CVD self-assembly and their use as robust scaffolds for lithium–sulfur batteries. *Adv Mater*. 2014;26(41):7051-7058.
95. Shi L, Chen Y, Song H, et al. Preparation and lithium-storage performance of a novel hierarchical porous carbon from sucrose using Mg-Al layered double hydroxides as template. *Electrochim Acta*. 2017;231:153-161.
96. Rümmeli MH, Bachmatiuk A, Scott A, et al. Direct low-temperature nanographene CVD synthesis over a dielectric insulator. *ACS Nano*. 2010;4(7):4206-4210.
97. Tang C, Wang H-S, Wang H-F, et al. Spatially confined hybridization of nanometer-sized NiFe hydroxides into nitrogen-doped graphene frameworks leading to superior oxygen evolution reactivity. *Adv Mater*. 2015;27(30):4516-4522.
98. Xie K, Qin X, Wang X, et al. Carbon nanocages as supercapacitor electrode materials. *Adv Mater*. 2012;24(3):347-352.
99. Ryou J, Hong S. First-principles study of carbon atoms adsorbed on MgO(100) related to graphene growth. *Curr Appl Phys*. 2013;13(2):327-330.
100. Lu L, Pei F, Abeln T, Pei Y. Tailoring three-dimensional interconnected nanoporous graphene micro/nano-foams for lithium–sulfur batteries. *Carbon*. 2020;157:437-447.
101. Lu L, de Hosson JTM, Pei Y. Three-dimensional micron-porous graphene foams for lightweight current collectors of lithium–sulfur batteries. *Carbon*. 2019;144:713-723.
102. Long L, Jiang X, Liu J, et al. In situ template synthesis of hierarchical porous carbon used for high-performance lithium–sulfur batteries. *RSC Adv*. 2018;8(9):4503-4513.
103. Xu J, Tan Z, Zeng W, et al. A hierarchical carbon derived from sponge-templated activation of graphene oxide for high-performance supercapacitor electrodes. *Adv Mater*. 2016;28(26):5222-5228.
104. Perananthan S, Bonso JS, Ferraris JP. Supercapacitors utilizing electrodes derived from polyacrylonitrile fibers incorporating tetramethylammonium oxalate as a porogen. *Carbon*. 2016;106:20-27.
105. Wang H, Zhou H, Wu S, et al. Facile synthesis of N/B co-doped hierarchically porous carbon materials based on threonine protic ionic liquids for supercapacitor. *Electrochim Acta*. 2021;380:138230.
106. Kubo S, White RJ, Tauer K, Titirici MM. Flexible coral-like carbon nanoarchitectures via a dual block copolymer-latex templating approach. *Chem Mater*. 2013;25(23):4781-4790.
107. Yu XL, Wang JG, Huang ZH, Shen WC, Kang FY. Ordered mesoporous carbon nanospheres as electrode materials for high-performance supercapacitors. *Electrochem Commun*. 2013;36:66-70.
108. Sun L, Zhou H, Li L, et al. Double soft-template synthesis of nitrogen/sulfur-codoped hierarchically porous carbon materials derived from protic ionic liquid for supercapacitor. *ACS Appl Mater Interfaces*. 2017;9(31):26088-26095.
109. Bulavova P, Parmentier J, Slovak V. Facile synthesis of soft-templated carbon monoliths with hierarchical porosity for fast adsorption from liquid media. *Micropor Mesopor Mat*. 2018;272:155-165.
110. Kundu S, Chowdhury IH, Naskar MK. Hierarchical porous carbon nanospheres for efficient removal of toxic organic water contaminants of phenol and methylene blue. *J Chem Eng Data*. 2018;63(3):559-573.
111. Fan XM, Yu C, Ling Z, Yang J, Qiu JS. Hydrothermal synthesis of phosphate-functionalized carbon nanotube-containing carbon composites for supercapacitors with highly stable performance. *ACS Appl Mater Interfaces*. 2013;5(6):2104-2110.
112. To JW, He J, Mei J, et al. Hierarchical N-doped carbon as CO_2 adsorbent with high CO_2 selectivity from rationally designed polypyrrole precursor. *J Am Chem Soc*. 2016;138(3):1001-1009.
113. Katchala N, Mohan EH, Bulusu SV, Varadaraju UV, Tata NR, Srinivasan A. One step synthesized hierarchical spherical porous carbon as an efficient electrode material for lithium-ion battery. *Mater Lett*. 2019;237:156-160.
114. Sun L, Zhou Y, Li L, et al. Facile and green synthesis of 3D honeycomb-like N/S-codoped hierarchically porous carbon materials from bio-protic salt for flexible, temperature-resistant supercapacitors. *Appl Surf Sci*. 2019;467:382-390.
115. Liu D, Cheng G, Zhao H, et al. Self-assembly of polyhedral oligosilsesquioxane (POSS) into hierarchically ordered mesoporous carbons with uniform microporosity and nitrogen-doping for high performance supercapacitors. *Nano Energy*. 2016;22:255-268.
116. Zhang S, Weng Q, Zhao F, et al. High electrocapacitive performance of bowl-like monodispersed porous carbon nanoparticles prepared with an interfacial self-assembly process. *J Colloid Interface Sci*. 2017;496:35-43.
117. Zhang X, Li Y, Cao C. Facile one-pot synthesis of mesoporous hierarchically structured silica/carbon nanomaterials. *J Mater Chem*. 2012;22(28):13918-13921.
118. Ren Y, Li M. Facile synthesis of SiO_x@C composite nanorods as anodes for lithium ion batteries with excellent electrochemical performance. *J Power Sources*. 2016;306:459-466.
119. Liu J, Yuan H, Tao X, et al. Recent progress on biomass-derived ecomaterials toward advanced rechargeable lithium batteries. *EcoMat*. 2020;2(1):e12019.
120. Xu J, Zhou K, Chen F, et al. Natural integrated carbon architecture for rechargeable lithium-sulfur batteries. *ACS Sustainable Chem Eng*. 2016;4(3):666-670.
121. Chung SH, Manthiram A. A natural carbonized leaf as polysulfide diffusion inhibitor for high-performance lithium–sulfur battery cells. *ChemSusChem*. 2014;7(6):1655-1661.

122. Li Y, Wang L, Gao B, et al. Hierarchical porous carbon materials derived from self-template bamboo leaves for lithium–sulfur batteries. *Electrochim Acta*. 2017;229:352-360.
123. Li M, Yu N, Qin JG, Li E, Du Z, Chen L. High-performance lithium–sulfur batteries with a cassava-derived carbon sheet as a polysulfides inhibitor. *New J Chem*. 2014;38(9):4549-4554.
124. Zhao Y, Wang L, Huang L, et al. Biomass-derived oxygen and nitrogen co-doped porous carbon with hierarchical architecture as sulfur hosts for high-performance lithium/sulfur batteries. *Nanomaterials*. 2017;7(11):402.
125. Zhao Y, Zhang X, He Y, Liu N, Tan T, Liang C. Biomass-derived nitrogen-doped highly porous carbon material with a hierarchical porous structure for high-performance lithium/sulfur batteries. *Materials*. 2017;10(10):1158.
126. Liang C, Zhang X, Zhao Y, Tan T, Zhang Y, Chen Z. Preparation of hierarchical porous carbon from waterweed and its application in lithium/sulfur batteries. *Energies*. 2018;11(6):1535.
127. Xia L, Zhou Y, Ren J, et al. An eco-friendly microorganism method to activate biomass for cathode materials for high-performance lithium–sulfur batteries. *Energy Fuel*. 2018;32(9):9997-10007.
128. Zheng B, Li N, Yang J, Xi J. Waste cotton cloth derived carbon microtube textile: a robust and scalable interlayer for lithium–sulfur batteries. *Chem Commun*. 2019;55(16):2289-2292.
129. Zhong M, Guan J, Sun J, et al. Carbon nanodot-decorated alveolate N, O, S tridoped hierarchical porous carbon as efficient electrocatalysis of polysulfide conversion for lithium–sulfur batteries. *Electrochim Acta*. 2019;299:600-609.
130. Chung SH, Manthiram A. Carbonized eggshell membrane as a natural polysulfide reservoir for highly reversible Li–S batteries. *Adv Mater*. 2014;26(9):1360-1365.
131. Wei S, Zhang H, Huang Y, Wang W, Xia Y, Yu Z. Pig bone derived hierarchical porous carbon and its enhanced cycling performance of lithium–sulfur batteries. *Energy Environ Sci*. 2011;4(3):736-740.
132. Shao H, Ai F, Wang W, et al. Crab shell-derived nitrogen-doped micro-/mesoporous carbon as an effective separator coating for high energy lithium–sulfur batteries. *J Mater Chem A*. 2017;5(37):19892-19900.
133. Zhang B, Xiao M, Wang S, et al. Novel hierarchically porous carbon materials obtained from natural biopolymer as host matrixes for lithium–sulfur battery applications. *ACS Appl Mater Interfaces*. 2014;6(15):13174-13182.
134. Zhong Y, Xia X, Deng S, et al. Spore carbon from aspergillus oryzae for advanced electrochemical energy storage. *Adv Mater*. 2018;30(46):1805165.
135. Sahore R, Estevez LP, Ramanujapuram A, DiSalvo FJ, Giannelis EP. High-rate lithium–sulfur batteries enabled by hierarchical porous carbons synthesized via ice templation. *J Power Sources*. 2015;297:188-194.
136. Klose M, Pinkert K, Zier M, et al. Hollow carbon nano-onions with hierarchical porosity derived from commercial metal–organic framework. *Carbon*. 2014;79:302-309.
137. Xi K, Cao S, Peng X, Ducati C, Kumar RV, Cheetham AK. Carbon with hierarchical pores from carbonized metal–organic frameworks for lithium–sulphur batteries. *Chem Commun*. 2013;49(22):2192-2194.
138. Xu GY, Ding B, Shen LF, Nie P, Han JP, Zhang XG. Sulfur embedded in metal organic framework-derived hierarchically porous carbon nanoplates for high performance lithium–sulfur battery. *J Mater Chem A*. 2013;1(14):4490-4496.
139. Yang XF, Yan N, Zhou W, Zhang HZ, Li XF, Zhang HM. Sulfur embedded in one-dimensional french fries-like hierarchical porous carbon derived from a metal-organic framework for high performance lithium–sulfur batteries. *J Mater Chem A*. 2015;3(29):15314-15323.
140. Yang X, Yu Y, Yan N, Zhang H, Li X, Zhang H. 1-D oriented cross-linking hierarchical porous carbon fibers as a sulfur immobilizer for high performance lithium–sulfur batteries. *J Mater Chem A*. 2016;4(16):5965-5972.
141. Chen T, Cheng B, Zhu G, et al. Highly efficient retention of polysulfides in "sea urchin"-like carbon nanotube/nanopolyhedra superstructures as cathode material for ultralong-life lithium–sulfur batteries. *Nano Lett*. 2017;17(1):437-444.
142. Zhang H, Zhao Z, Liu Y, et al. Nitrogen-doped hierarchical porous carbon derived from metal-organic aerogel for high performance lithium–sulfur batteries. *J Energy Chem*. 2017;26(6):1282-1290.
143. Chang Z, Ding B, Dou H, Wang J, Xu G, Zhang X. Hierarchically porous multilayered carbon barriers for high-performance Li–S batteries. *Chem Eur J*. 2018;24(15):3768-3775.
144. Li G, Lei W, Luo D, et al. Stringed "tube on cube" nanohybrids as compact cathode matrix for high-loading and lean-electrolyte lithium–sulfur batteries. *Energy Environ Sci*. 2018;11(9):2372-2381.
145. Shan J, Liu Y, Su Y, et al. Graphene-directed two-dimensional porous carbon frameworks for high-performance lithium–sulfur battery cathodes. *J Mater Chem A*. 2016;4(1):314-320.
146. Wu H, Huang Y, Xu S, Zhang W, Wang K, Zong M. Fabricating three-dimensional hierarchical porous N-doped graphene by a tunable assembly method for interlayer assisted lithium–sulfur batteries. *Chem Eng J*. 2017;327:855-867.
147. Zhang H, Gao Q, Qian W, et al. Binary hierarchical porous graphene/pyrolytic carbon nanocomposite matrix loaded with sulfur as a high-performance Li–S battery cathode. *ACS Appl Mater Interfaces*. 2018;10(22):18726-18733.
148. Yang W, Yang W, Song A, Sun G, Shao G. 3D interconnected porous carbon nanosheets/carbon nanotubes as a polysulfide reservoir for high-performance lithium–sulfur batteries. *Nanoscale*. 2018;10(2):816-824.
149. Zhang XY, Xue DP, Jiang S, et al. Rational confinement engineering of MOF-derived carbon-based electrocatalysts toward CO_2 reduction and O_2 reduction reactions. *InfoMat*. 2022;4:e12257
150. Ren J, Huang Y, Zhu H, et al. Recent progress on MOF-derived carbon materials for energy storage. *Carbon Energy*. 2020;2(2):176-202.
151. Williams PT, Reed AR. Development of activated carbon pore structure via physical and chemical activation of biomass fibre waste. *Biomass Bioenerg*. 2006;30(2):144-152.
152. Wang M, Zhang H, Zhang Y, Li J, Zhang F, Hu W. A modified hierarchical porous carbon for lithium/sulfur batteries with improved capacity and cycling stability. *J Solid State Electr*. 2013;17(8):2243-2250.
153. Singhal R, Chung S-H, Manthiram A, Kalra V. A free-standing carbon nanofiber interlayer for high-performance lithium–sulfur batteries. *J Mater Chem A*. 2015;3(8):4530-4538.

154. Kim J-J, Kim HS, Ahn J, Lee KJ, Yoo WC, Sung Y-E. Activation of micropore-confined sulfur within hierarchical porous carbon for lithium–sulfur batteries. *J Power Sources*. 2016;306:617-622.
155. Moreno N, Caballero A, Morales J, Agostini M, Hassoun J. Lithium battery using sulfur infiltrated in three-dimensional flower-like hierarchical porous carbon electrode. *Mater Chem Phys*. 2016;180:82-88.
156. Zeng S-Z, Zeng X, Tu W, et al. Facile and tailored synthesis of ultrahigh-surface-area clews of carbon nanobelts for high-rate lithium–sulfur batteries. *J Mater Chem A*. 2017;5(44):23209-23220.
157. Sahore R, Levin BDA, Pan M, Muller DA, DiSalvo FJ, Giannelis EP. Design principles for optimum performance of porous carbons in lithium–sulfur batteries. *Adv Energy Mater*. 2016;6(14):1600134.
158. Thieme S, Brückner J, Meier A, et al. A lithium–sulfur full cell with ultralong cycle life: influence of cathode structure and polysulfide additive. *J Mater Chem A*. 2015;3(7):3808-3820.
159. Liu D, Li Y, Zheng D, et al. Ammonia-treated ordered mesoporous carbons with hierarchical porosity and nitrogen-doping for lithium–sulfur batteries. *ChemistrySelect*. 2017;2(24):7160-7168.
160. Hoffmann C, Thieme S, Brückner J, et al. Nanocasting hierarchical carbide-derived carbons in nanostructured opal assemblies for high-performance cathodes in lithium–sulfur batteries. *ACS Nano*. 2014;8(12):12130-12140.
161. Oschatz M, Borchardt L, Pinkert K, et al. Hierarchical carbide-derived carbon foams with advanced mesostructure as a versatile electrochemical energy-storage material. *Adv Energy Mater*. 2014;4(2):1300645.
162. Wei Y, Tao Y, Zhang C, et al. Layered carbide-derived carbon with hierarchically porous structure for high rate lithium–sulfur batteries. *Electrochim Acta*. 2016;188:385-392.
163. Wang J, Tang J, Ding B, et al. Hierarchical porous carbons with layer-by-layer motif architectures from confined soft-template self-assembly in layered materials. *Nat Commun*. 2017;8:15717.
164. Wang J, Yang Y, Kang F. Porous carbon nanofiber paper as an effective interlayer for high-performance lithium–sulfur batteries. *Electrochim Acta*. 2015;168:271-276.
165. Park M-S, Yu J-S, Kim KJ, et al. Porous carbon spheres as a functional conducting framework for use in lithium–sulfur batteries. *RSC Adv*. 2013;3(29):11774-11781.
166. Zhao S, Li C, Wang W, et al. A novel porous nanocomposite of sulfur/carbon obtained from fish scales for lithium–sulfur batteries. *J Mater Chem A*. 2013;1(10):3334-3339.
167. Gao M, Li C, Liu N, et al. Inhibition on polysulfides dissolve during the discharge-charge by using fish-scale-based porous carbon for lithium–sulfur battery. *Electrochim Acta*. 2014;149:258-263.
168. Moreno N, Caballero A, Hernán L, Morales J. Lithium–sulfur batteries with activated carbons derived from olive stones. *Carbon*. 2014;70:241-248.
169. Peng H-J, Huang J-Q, Zhao M-Q, et al. Nanoarchitectured graphene/CNT@porous carbon with extraordinary electrical conductivity and interconnected micro/mesopores for lithium–sulfur batteries. *Adv Funct Mater*. 2014;24(19):2772-2781.
170. Qu Y, Zhang Z, Jiang S, et al. Confining selenium in nitrogen-containing hierarchical porous carbon for high-rate rechargeable lithium–selenium batteries. *J Mater Chem A*. 2014;2(31):12255-12261.
171. Wang H, Chen Z, Liu HK, Guo Z. A facile synthesis approach to micro–macroporous carbon from cotton and its application in the lithium–sulfur battery. *RSC Adv*. 2014;4(110):65074-65080.
172. Cao Z, Zhang J, Ding Y, et al. Lotus root-like structured carbon fibers as encapsulated sulfur host for lithium–sulfur batteries. *J Electrochem Soc*. 2015;162(10):A2157-A2162.
173. Gu X, Lai C, Liu F, Yang W, Hou Y, Zhang S. A conductive interwoven bamboo carbon fiber membrane for Li–S batteries. *J Mater Chem A*. 2015;3(18):9502-9509.
174. Liu M, Chen Y, Chen K, et al. Biomass-derived activated carbon for rechargeable lithium–sulfur batteries. *BioResources*. 2015;10(1):155-168.
175. Deng W, Hu A, Chen X, et al. Sulfur-impregnated 3D hierarchical porous nitrogen-doped aligned carbon nanotubes as high-performance cathode for lithium–sulfur batteries. *J Power Sources*. 2016;322:138-146.
176. Ren G, Li S, Fan Z-X, Warzywoda J, Fan Z. Soybean-derived hierarchical porous carbon with large sulfur loading and sulfur content for high-performance lithium–sulfur batteries. *J Mater Chem A*. 2016;4(42):16507-16515.
177. Cai J, Wu C, Zhu Y, Zhang K, Shen PK. Sulfur impregnated N, P co-doped hierarchical porous carbon as cathode for high-performance Li–S batteries. *J Power Sources*. 2017;341:165-174.
178. Chen M, Jiang S, Cai S, et al. Hierarchical porous carbon modified with ionic surfactants as efficient sulfur hosts for the high-performance lithium–sulfur batteries. *Chem Eng J*. 2017;313:404-414.
179. Chen M, Jiang S, Huang C, et al. Honeycomb-like nitrogen and sulfur dual-doped hierarchical porous biomass-derived carbon for lithium–sulfur batteries. *ChemSusChem*. 2017;10(8):1803-1812.
180. Guo Z, Zhang B, Li D, et al. A mixed microporous/low-range mesoporous composite with high sulfur loading from hierarchically-structured carbon for lithium–sulfur batteries. *Electrochim Acta*. 2017;230:181-188.
181. Ji S, Imtiaz S, Sun D, et al. Coralline-like N-doped hierarchically porous carbon derived from enteromorpha as a host matrix for lithium–sulfur battery. *Chem Eur J*. 2017;23(72):18208-18215.
182. Wu X, Fan L, Wang M, et al. Long-life lithium–sulfur battery derived from nori-based nitrogen and oxygen dual-doped 3D hierarchical biochar. *ACS Appl Mater Interfaces*. 2017;9(22):18889-18896.
183. Xu Z. Corncob-derived porous carbon as an interlayer coating to improve the performance of lithium sulphur battery. *Int J Electrochem Sci*. 2017;12(5):4515-4527.
184. Xue M, Chen C, Ren Z, Tan Y, Li B, Zhang C. A novel mangosteen peels derived hierarchical porous carbon for lithium–sulfur battery. *Mater Lett*. 2017;209:594-597.
185. Liang Y, Chen L, Zhuang D, et al. Fabrication and nanostructure control of super-hierarchical carbon materials from heterogeneous bottlebrushes. *Chem Sci*. 2017;8(3):2101-2106.
186. Cao Z, Zhang R, Shi M, et al. Rational design oxygen and sulfur dual-doped 3D hierarchical porous carbons for high-performance lithium–sulfur batteries. *J Electrochem Soc*. 2018;165(2):A31-A39.

187. Huang J-Q, Chong WG, Zheng Q, et al. Understanding the roles of activated porous carbon nanotubes as sulfur support and separator coating for lithium–sulfur batteries. *Electrochim Acta*. 2018;268:1-9.
188. Kang D, Tang K, Lemmon JP. Tunable pore structure for confining polysulfides in high performance Li–S battery with coal precursor. *Appl Surf Sci*. 2018;458:714-721.
189. Selvan RK, Zhu P, Yan C, et al. Biomass-derived porous carbon modified glass fiber separator as polysulfide reservoir for Li–S batteries. *J Colloid Interface Sci*. 2018;513:231-239.
190. Wu H, Xia L, Ren J, et al. A multidimensional and nitrogen-doped graphene/hierarchical porous carbon as a sulfur scaffold for high-performance lithium–sulfur batteries. *Electrochim Acta*. 2018;278:83-92.
191. Wu P, Chen L-H, Xiao S-S, et al. Insight into the positive effect of porous hierarchy in S/C cathodes on the electrochemical performance of Li–S batteries. *Nanoscale*. 2018;10(25):11861-11868.
192. Yan Y, Shi M, Wei Y, et al. Process optimization for producing hierarchical porous bamboo-derived carbon materials with ultrahigh specific surface area for lithium–sulfur batteries. *J Alloys Compd*. 2018;738:16-24.
193. Yan Y, Shi M, Wei Y, et al. The hierarchical porous structure of carbon aerogels as matrix in cathode materials for Li–S batteries. *J Nanopart Res*. 2018;20(10):260.
194. Yan Y, Wei Y, Li Q, et al. Activated porous carbon materials with ultrahigh specific surface area derived from banana peels for high-performance lithium–sulfur batteries. *J Mater Sci*. 2018;29(13):11325-11335.
195. Yu J, Li X, Shu Y, Ma L, Zhang X, Ding Y. Anchoring polysulfides in hierarchical porous carbon aerogel via electric-field-responsive switch for lithium–sulfur battery. *Electrochim Acta*. 2019;293:458-465.
196. Chabu JM, Li YJ, Liu YN. Biomass-derived N, O, and S-tridoped hierarchically porous carbon as a cathode for lithium–sulfur batteries. *ChemNanoMat*. 2019;5(5):612-618.
197. Jiang S, Chen M, Wang X, et al. Honeycomb-like nitrogen and sulfur dual-doped hierarchical porous biomass carbon bifunctional interlayer for advanced lithium–sulfur batteries. *Chem Eng J*. 2019;355:478-486.
198. Li M, H Y, Wang X, et al. Hierarchical porous carbon derived from peanut hull for polysulfide confinement in lithium–sulfur batteries. *Energy Technol*. 2019;7(3):6125-6138.
199. Zeng SB, Li X, Zhong H, Chen SW, Mai YH. Layered electrodes based on 3D hierarchical porous carbon and conducting polymers for high-performance lithium–sulfur batteries. *Small Methods*. 2019;3(5):1900028.
200. Liu X, Huang W, Wang D, Tian J, Shan Z. A nitrogen-doped 3D hierarchical carbon/sulfur composite for advanced lithium–sulfur batteries. *J Power Sources*. 2017;355:211-218.
201. Polrolniczak P, Nowicki P, Wasinski K, Pietrzak R, Walkowiak M. Biomass-derived hierarchical carbon as sulfur cathode stabilizing agent for lithium–sulfur batteries. *Solid State Ionics*. 2016;297:59-63.
202. Schneidermann C, Kensy C, Otto P, et al. Nitrogen-doped biomass-derived carbon formed by mechanochemical synthesis for lithium–sulfur batteries. *ChemSusChem*. 2019;12(1):310-319.
203. Wu HL, Mou JR, Zhou L, Zheng QJ, Jiang N, Lin DM. Cloud cap-like, hierarchically porous carbon derived from mushroom as an excellent host cathode for high-performance lithium–sulfur batteries. *Electrochim Acta*. 2016;212:1021-1030.
204. Ren J, Zhou Y, Wu H, Xie F, Xu C, Lin D. Sulfur-encapsulated in heteroatom-doped hierarchical porous carbon derived from goat hair for high performance lithium–sulfur batteries. *J Energy Chem*. 2019;30:121-131.
205. Song Z, Lu X, Hu Q, et al. Synergistic confining polysulfides by rational design a N/P co-doped carbon as sulfur host and functional interlayer for high-performance lithium–sulfur batteries. *J Power Sources*. 2019;421:23-31.
206. Lozano-Castelló D, Calo JM, Cazorla-Amorós D, Linares-Solano A. Carbon activation with KOH as explored by temperature programmed techniques, and the effects of hydrogen. *Carbon*. 2007;45(13):2529-2536.
207. Wang J, Kaskel S. KOH activation of carbon-based materials for energy storage. *J Mater Chem*. 2012;22(45):23710-23725.
208. Raymundo-Piñero E, Azaïs P, Cacciaguerra T, Cazorla-Amorós D, Linares-Solano A, Béguin F. KOH and NaOH activation mechanisms of multiwalled carbon nanotubes with different structural organisation. *Carbon*. 2005;43(4):786-795.
209. Qiao W, Yoon S-H, Mochida I. KOH activation of needle coke to develop activated carbons for high-performance EDLC. *Energy Fuel*. 2006;20(4):1680-1684.
210. Wang H, Gao Q, Hu J. High hydrogen storage capacity of porous carbons prepared by using activated carbon. *J Am Chem Soc*. 2009;131(20):7016-7022.
211. Oschatz M, Thieme S, Borchardt L, et al. A new route for the preparation of mesoporous carbon materials with high performance in lithium–sulphur battery cathodes. *Chem Commun*. 2013;49(52):5832-5834.
212. Zhao C, Liu L, Zhao H, et al. Sulfur-infiltrated porous carbon microspheres with controllable multi-modal pore size distribution for high energy lithium–sulfur batteries. *Nanoscale*. 2014;6(2):882-888.
213. Zhang F, Ji S, Wang H, Liang H, Wang X, Wang R. Implanting cobalt atom clusters within nitrogen-doped carbon network as highly stable cathode for lithium–sulfur batteries. *Small Methods*. 2021;5(6):e2100066.
214. Zhu L, Zhu W, Cheng X-B, et al. Cathode materials based on carbon nanotubes for high-energy-density lithium–sulfur batteries. *Carbon*. 2014;75:161-168.
215. To JW, Chen Z, Yao H, et al. Ultrahigh surface area three-dimensional porous graphitic carbon from conjugated polymeric molecular framework. *ACS Central Sci*. 2015;1(2):68-76.
216. Yu X, Zhao J, Lv R, et al. Facile synthesis of nitrogen-doped carbon nanosheets with hierarchical porosity for high performance supercapacitors and lithium–sulfur batteries. *J Mater Chem A*. 2015;3(36):18400-18405.
217. Gong Z, Wu Q, Wang F, et al. A hierarchical micro/mesoporous carbon fiber/sulfur composite for high-performance lithium-sulfur batteries. *RSC Adv*. 2016;6(44):37443-37451.
218. Rybarczyk MK, Peng H-J, Tang C, Lieder M, Zhang Q, Titirici M-M. Porous carbon derived from rice husks as sustainable bioresources: insights into the role of micro-/mesoporous hierarchy in hosting active species for lithium–sulphur batteries. *Green Chem*. 2016;18(19):5169-5179.

219. Strubel P, Althues H, Kaskel S. Zinc-salt templating of hierarchical porous carbons for low electrolyte high energy lithium–sulfur batteries (LE-LiS). *Carbon*. 2016;107:705-710.
220. Vu D-L, Seo J-S, Lee H-Y, Lee J-W. Activated carbon with hierarchical micro-mesoporous structure obtained from rice husk and its application for lithium–sulfur batteries. *RSC Adv*. 2017;7(7):4144-4151.
221. Zhang B, Zhao Y, Liu J, Wang X, Li D, Li X. Impact of micro-/mesoporous carbonaceous structure on electrochemical performance of sulfur. *Electrochim Acta*. 2017;248:416-424.
222. Zhao F, Li D, Cao B, Liu M, Chen K, Chen Y. Hierarchical carbon microstructures prepared from oil-palm-shell tracheids for Li–S batteries. *New J Chem*. 2017;41(10):4110-4115.
223. Zhang L, Zhao W, Yuan S, et al. Engineering the morphology/porosity of oxygen-doped carbon for sulfur host as lithium–sulfur batteries. *J Energy Chem*. 2021;60:531-545.
224. Ren J, Zhou Y, Guo M, Zheng Q, Lin D. Novel sustainable nitrogen, iodine-dual-doped hierarchical porous activated carbon as a superior host material for high-performance lithium–sulfur batteries. *Int J Hydrogen Energy*. 2018;43(43):20022-20032.
225. Wu R, Chen S, Deng J, et al. Hierarchically porous nitrogen-doped carbon as cathode for lithium–sulfur batteries. *J Energy Chem*. 2018;27(6):1661-1667.
226. Wu S, Cao Q, Wang M, Yu T, Wang H, Lu S. Engineering multi-chambered carbon nanospheres@carbon as efficient sulfur hosts for lithium–sulfur batteries dagger. *J Mater Chem A*. 2018;6(23):10891-10897.
227. Xue M, Chen C, Tan Y, Ren Z, Li B, Zhang C. Mangosteen peel-derived porous carbon: synthesis and its application in the sulfur cathode for lithium–sulfur battery. *J Mater Sci*. 2018;53(15):11062-11077.
228. Yang H, Zhang X, Guo J, et al. A N,S-codoped hierarchical carbon foam@porous carbon composite as freestanding cathode for high-performance lithium–sulfur batteries. *J Alloys Compd*. 2018;768:495-502.
229. You X-L, Liu L-J, Zhang M-Y, Walle MD, Li Y, Liu Y-N. Novel biomass-derived hierarchical porous carbon for lithium–sulfur batteries. *Mater Lett*. 2018;217:167-170.
230. Cheng D, Wu P, Wang J, et al. Synergetic pore structure optimization and nitrogen doping of 3D porous graphene for high-performance lithium–sulfur battery. *Carbon*. 2019;143:869-877.
231. Fan X, Tan F, Meng F, Liu J. Hierarchical porous N-doped carbon nanosheets obtained by organic-inorganic bipolymeric engineering for improved lithium–sulfur batteries. *Chem Eur J*. 2019;25(16):4040-4046.
232. Xia L, Song Z, Zhou L, Lin D, Zheng Q. Nitrogen and oxygen dual-doped hierarchical porous carbon derived from rapeseed meal for high-performance lithium–sulfur batteries. *J Solid State Chem*. 2019;270:500-508.
233. Yang DH, Zhou HY, Liu H, Han BH. Hollow N-doped carbon polyhedrons with hierarchically porous shell for confinement of polysulfides in lithium–sulfur batteries. *iScience*. 2019;13:243-253.
234. Park J, Yoon S, Oh S, et al. A systematic correlation between morphology of porous carbon cathode and electrolyte in lithium–sulfur battery. *J Energy Chem*. 2021;61:561-573.
235. Zhang J, Xiang J, Dong Z, et al. Biomass-derived activated carbon with 3D connected architecture for rechargeable lithium–sulfur batteries. *Electrochim Acta*. 2014;116:146-151.
236. Song Y, Li X, He C. Porous carbon framework nested nickel foam as freestanding host for high energy lithium–sulfur batteries. *Chin Chem Lett*. 2021;32(3):1106-1110.
237. Jung DS, Hwang TH, Lee JH, et al. Hierarchical porous carbon by ultrasonic spray pyrolysis yields stable cycling in lithium–sulfur battery. *Nano Lett*. 2014;14(8):4418-4425.
238. Liu Y, Li G, Fu J, Chen Z, Peng X. Strings of porous carbon polyhedrons as self-standing cathode host for high-energy-density lithium–sulfur batteries. *Angew Chem Int Ed*. 2017;56(22):6176-6180.
239. Luo C, Lv W, Deng Y, et al. A dual-function Na_2SO_4 template directed formation of cathode materials with a high content of sulfur nanodots for lithium–sulfur batteries. *Small*. 2017;13(27):1700358.
240. Tang Q, Li H, Zuo M, et al. Optimized assembly of micro-/meso-/macroporous carbon for Li–S batteries. *Nano*. 2017;12(2):1750021.
241. Yang T, Zhong Y, Liang J, et al. Hierarchical porous yolk-shell carbon nanosphere for high-performance lithium–sulfur batteries. *Part Part Syst Charact*. 2017;34(4):1600281.
242. Dai F, Shen J, Dailly A, et al. Hierarchical electrode architectures for high energy lithium-chalcogen rechargeable batteries. *Nano Energy*. 2018;51:668-679.
243. Ge Y, Chen Z, Ye S, Zhu Z, Tu Y, Yang X. A spheres-in-tube carbonaceous nanostructure for high-capacity and high-rate lithium–sulfur batteries. *J Mater Chem A*. 2018;6(30):14885-14893.
244. Qin X, Wu J, Xu Z-L, et al. Electrosprayed multiscale porous carbon microspheres as sulfur hosts for long-life lithium–sulfur batteries. *Carbon*. 2019;141:16-24.
245. Yang M, Hu X, Fang Z, et al. Bifunctional MOF-derived carbon photonic crystal architectures for advanced Zn-air and Li–S batteries: highly exposed graphitic nitrogen matters. *Adv Funct Mater*. 2017;27(36):1701971.
246. Yan Y, Shi M, Zou Y, et al. Tunable hierarchical porous carbon aerogel/graphene composites cathode matrix for Li–S batteries. *J Alloys Compd*. 2019;791:952-961.
247. Yan Y, Wei Y, Zhao C, et al. A modified template-removal process to improve the specific surface area and hierarchical porosity of carbon materials. *J Solid State Chem*. 2019;269:24-29.
248. Tang Z, Xu F, Liang Y, Wu D, Fu R. Preparation and electrochemical performance of a hierarchically porous activated carbon aerogel/sulfur cathode for lithium–sulfur batteries. *New Carbon Mater*. 2015;30(4):319-326.
249. Lu R, Cheng M, Mao L, et al. Nitrogen-doped nanoarray-modified 3D hierarchical graphene as a cofunction host for high-performance flexible Li–S battery. *EcoMat*. 2020;2(1):e12010.
250. Yuan Z, Peng H-J, Huang J-Q, et al. Hierarchical free-standing carbon-nanotube paper electrodes with ultrahigh sulfur-loading for lithium–sulfur batteries. *Adv Funct Mater*. 2014;24(39):6105-6112.
251. Ding B, Yuan C, Shen L, Xu G, Nie P, Zhang X. Encapsulating sulfur into hierarchically ordered porous carbon as a high-performance cathode for lithium–sulfur batteries. *Chem Eur J*. 2013;19(3):1013-1019.
252. Cai J, Wu C, Yang S, Zhu Y, Shen PK, Zhang K. Templated and catalytic fabrication of N-doped hierarchical porous carbon-carbon nanotube hybrids as host for lithium–sulfur batteries. *ACS Appl Mater Interfaces*. 2017;9(39):33876-33886.

253. Zhang C, Zhang Z, Wang D, Yin F, Zhang Y. Three-dimensionally ordered macro-/mesoporous carbon loading sulfur as high-performance cathodes for lithium/sulfur batteries. *J Alloys Compd*. 2017;714:126-132.
254. Zhang J, You C, Wang J, et al. Confinement of sulfur species into heteroatom-doped, porous carbon container for high areal capacity cathode. *Chem Eng J*. 2019;368:340-349.
255. Liu Z, Wang L, Yang W. Hierarchically porous nitrogen-doped carbon foams decorated with zinc nanodots as high-performance sulfur hosts for lithium–sulfur battery. *Chin Chem Lett*. 2021;32(9):2919-2922.
256. Wang P, Qi X, Zhao W, Qian M, Bi H, Huang F. Nitrogen-doped hierarchical few-layered porous carbon for efficient electrochemical energy storage. *Carbon Energy*. 2021;3(2):349-359.
257. Tang W, Chen Z, Tian B, et al. In situ observation and electrochemical study of encapsulated sulfur nanoparticles by MoS_2 flakes. *J Am Chem Soc*. 2017;139(29):10133-10141.
258. Wei ZH, Ren YQ, Sokolowski J, Zhu XD, Wu G. Mechanistic understanding of the role separators playing in advanced lithium–sulfur batteries. *InfoMat*. 2020;2(3):483-508.
259. Arora P, Zhang Z. Battery separators. *Chem Rev*. 2004;104(10):4419-4462.
260. Zhen M, Wang J, Wang X, Wang C. Hierarchical N-rich carbon sponge with excellent cycling performance for lithium–sulfur battery at high rates. *Chem Eur J*. 2018;24(22):5860-5867.
261. Sui Z-Y, Yang Q-S, Zhou H-Y, et al. Nitrogen-doped graphene aerogel as both a sulfur host and an effective interlayer for high-performance lithium–sulfur batteries. *Nanotechnology*. 2017;28(49):495701.
262. Albertus P, Babinec S, Litzelman S, Newman A. Status and challenges in enabling the lithium metal electrode for high-energy and low-cost rechargeable batteries. *Nat Energy*. 2018;3(1):16-21.
263. Zhang Y, Zuo T-T, Popovic J, et al. Towards better Li metal anodes: challenges and strategies. *Mater Today*. 2020;33:56-74.
264. Zhang X, Wang A, Liu X, Luo J. Dendrites in lithium metal anodes: suppression, regulation, and elimination. *Acc Chem Res*. 2019;52(11):3223-3232.
265. Xiao J, Li Q, Bi Y, et al. Understanding and applying coulombic efficiency in lithium metal batteries. *Nat Energy*. 2020;5(8):561-568.
266. Ye H, Xin S, Yin YX, Guo YG. Advanced porous carbon materials for high-efficient lithium metal anodes. *Adv Energy Mater*. 2017;7(23):9.
267. Lu Y, Lu Y, Jin C, et al. Natural wood structure inspires practical lithium–metal batteries. *ACS Energy Lett*. 2021;6(6):2103-2110.
268. Chen Y, Zou K, Dai X, et al. Polysulfide filter and dendrite inhibitor: highly graphitized wood framework inhibits polysulfide shuttle and lithium dendrites in Li–S batteries. *Adv Funct Mater*. 2021;31(31):2102458.
269. Zheng G, Lee SW, Liang Z, et al. Interconnected hollow carbon nanospheres for stable lithium metal anodes. *Nat Nanotechnol*. 2014;9(8):618-623.
270. Liu L, Yin YX, Li JY, et al. Free-standing hollow carbon fibers as high-capacity containers for stable lithium metal anodes. *Joule*. 2017;1(3):563-575.
271. Lu Q, Jie Y, Meng X, et al. Carbon materials for stable Li metal anodes: challenges, solutions, and outlook. *Carbon Energy*. 2021;3(6):957-975.
272. Liu Y, Li X, Fan L, Li S, Maleki Kheimeh Sari H, Qin J. A review of carbon-based materials for safe lithium metal anodes. *Front Chem*. 2019;7:721-721.
273. Fu A, Wang C, Pei F, Cui J, Fang X, Zheng N. Recent advances in hollow porous carbon materials for lithium–sulfur batteries. *Small*. 2019;15:1804786.
274. Zhang R, Cheng XB, Zhao CZ, et al. Conductive nanostructured scaffolds render low local current density to inhibit lithium dendrite growth. *Adv Mater*. 2016;28(11):2155-2162.
275. Fang Y, Zhang SL, Wu Z-P, Luan D, Lou XW. A highly stable lithium metal anode enabled by Ag nanoparticle–embedded nitrogen-doped carbon macroporous fibers. *Sci Adv*. 2021;7(21):eabg3626.
276. Li Z, Li X, Zhou L, et al. A synergistic strategy for stable lithium metal anodes using 3D fluorine-doped graphene shuttle-implanted porous carbon networks. *Nano Energy*. 2018;49:179-185.
277. Lyu Z, Lim GJH, Guo R, et al. 3D-printed electrodes for lithium metal batteries with high areal capacity and high-rate capability. *Energy Stor Mater*. 2020;24:336-342.
278. Liu L, Yin Y-X, Li J-Y, Wang S-H, Guo Y-G, Wan L-J. Uniform lithium nucleation/growth induced by lightweight nitrogen-doped graphitic carbon foams for high-performance lithium metal anodes. *Adv Mater*. 2018;30(10):1706216.
279. Xu Z, Xu L, Xu Z, Deng Z, Wang XN. O-codoped carbon nanosheet array enabling stable lithium metal anode. *Adv Funct Mater*. 2021;31(40):2102354.
280. Liu S, Li J, Yan X, et al. Superhierarchical cobalt-embedded nitrogen-doped porous carbon nanosheets as two-in-one hosts for high-performance lithium–sulfur batteries. *Adv Mater*. 2018;30(12):1706895.
281. Liu X, Qian X, Tang W, et al. Designer uniform Li plating/stripping through lithium–cobalt alloying hierarchical scaffolds for scalable high-performance lithium–metal anodes. *J Energy Chem*. 2021;52:385-392.
282. Zhang Z, Wang J, Yan X, et al. In-situ growth of hierarchical N-doped CNTs/Ni foam scaffold for dendrite-free lithium metal anode. *Energy Stor Mater*. 2020;29:332-340.
283. Sun Q, Zhai W, Hou G, et al. In situ synthesis of a lithiophilic Ag-nanoparticles-decorated 3D porous carbon framework toward dendrite-free lithium metal anodes. *ACS Sustainable Chem Eng*. 2018;6(11):15219-15227.
284. Fang Y, Zeng Y, Jin Q, et al. Nitrogen-doped amorphous Zn–carbon multichannel fibers for stable lithium metal anodes. *Angew Chem Int Ed*. 2021;60(15):8515-8520.
285. Chen C, Guan J, Li NW, et al. Lotus-root-like carbon fibers embedded with Ni-Co nanoparticles for dendrite-free lithium metal anodes. *Adv Mater*. 2021;33(24):e2100608.
286. Zhang Y, Luo W, Wang C, et al. High-capacity, low-tortuosity, and channel-guided lithium metal anode. *Proc Natl Acad Sci U S A*. 2017;114(14):3584-3589.

287. Jin C, Sheng O, Luo J, et al. 3D lithium metal embedded within lithiophilic porous matrix for stable lithium metal batteries. *Nano Energy*. 2017;37:177-186.
288. Dong Q, Shen R, Li C, et al. Construction of soft base tongs on separator to grasp polysulfides from shuttling in lithium–sulfur batteries. *Small*. 2018;14(52):1804277.
289. Xie J, Wang J, Lee HR, et al. Engineering stable interfaces for three-dimensional lithium metal anodes. *Sci Adv*. 2018;4(7):eaat5168.
290. Lou X-W. Sulfur-preloaded double-shelled C@MoS_2 structures as an additive reservoir for stable lithium metal anodes. *Angew Chem Int Ed*. 2020;59(37):15839-15843.

AUTHOR BIOGRAPHIES

Yinyu Xiang obtained his Bachelor's degree from Wuhan University of Science and Technology in 2015 and his Master's degree in Chemical Engineering from Wuhan University of Technology in 2018. Currently, he is a PhD student under the supervision of Prof. Yutao Pei, Department of Advanced Production Engineering, Faculty of Science and Engineering, University of Groningen, the Netherlands. His research is focused on porous carbon materials for energy storage, including lithium-ion batteries, and lithium–sulfur batteries.

Dr. Liqiang Lu is a postdoctoral research fellow at the University of Groningen. He obtained his master degree from Shanghai University in 2012 and then worked as a research assistant in the Shanghai Institute of Ceramics, CAS, China, during 2012–2014. He received his PhD degree under the supervision of Prof. Yutao Pei and Prof. Jeff Th. M. de Hosson from the University of Groningen in 2018. His research interests mainly focus on developing high-energy-density batteries such as lithium–sulfur batteries, lithium metal batteries, sodium–metal batteries, and all-solid-state batteries by designing advanced electrodes, separators, and electrolytes.

Dr. Ajay Giri Prakash Kottapalli is an assistant professor in the Department of Advanced Production Engineering at University of Groningen. In 2013, he received his Ph.D. degree from Nanyang Technological University. During 2014-2015, he was a Postdoctoral Associate at Singapore-MIT Alliance for Research and Technology (SMART), and in 2016, he became a Principal Research Scientist at SMART. He is also currently a Research Affiliate with the MIT Sea Grant at MIT. In 2018, he was awarded the top-10 innovators under 35 in Asia-Pacific by MIT Technology Review. His research interests mainly include biomimetic/bio-inspired MEMS/NEMS, flexible electronics and biomedical sensors.

Prof. Yutao Pei is a professor in the Department of Advanced Production Engineering at the University of Groningen, the Netherlands. He received his PhD degree in Exploration Engineering from China University of Geosciences, Wuhan, in 1992. During 1993–1994, he was a postdoctoral fellow at the Harbin Institute of Technology, China. In 1995, he became an associate professor at Beijing University of Technology. Since 1998, he joined the Netherlands Institute for Metals Research that was transformed in 2008 into the Materials Innovation Institute M2i. His current research interests mainly include nanostructured materials for energy storage and devices, additive manufacturing of metals, laser materials processing and technology, surface, and interface science.

How to cite this article: Xiang Y, Lu L, Kottapalli AGP, Pei Y. Status and perspectives of hierarchical porous carbon materials in terms of high-performance lithium–sulfur batteries. *Carbon Energy*. 2022;1-53. doi:10.1002/cey2.185